Dynamic spatially resolved unilateral NMR measurements of liquid ingress and vapour adsorption and desorption in heterogeneous layered fabrics

Hans Adriaensen

A thesis submitted in partial fulfilment of the requirements of

Nottingham Trent University for the degree of Doctor of Philosophy

October 2010

"Hopes are always accompanied by fears, and, in scientific research, the fears are liable to become dominant."

Paul Adrien Maurice Dirac

ACKNOWLEDGMENTS

To Clive Dixon at the chemistry glassware unit in the University of Nottingham who helped to produce a vapour generator by building and incorporating a "L" shaped glass tube to the main body of the flask.

In the beginning, after a few weeks of work, my supervisor told me the following: "You just missed the MRPM conference in Bologna, (in Italy, 2006)!" This gave me an enormous motivation. Therefore at the end of the first year I aimed to present my work at the ICMRM conference in Aachen (2007), where I met Johannes Leisen who brought a good insight about textile fabrics.

Afterwards, the originality and divergence of the work brought me to another conference on the characterisation of porous solids (COPS, in Edinburgh, 2008) where my work was different compared to the other presentations but relevant and interestingly exciting in that NMR or even MRI is also a potential technique to reveal some characteristics about activated carbons. All those people on that conference were swearing only through isotherms. I was glad I could discover isotherms and more importantly understand their meaning.

At the last conference in Biarritz (Carbon 2009), we met Jacques Conard who monitored linewidth changes and chemical shifts during adsorption in the early 70's with a different instrument. His publications (written in French!) are of a great interest for this thesis. I have related his linewidth variations to changes of R_2 in this work.

Thank you to my parents Magdalena and Joene Adriaensen for their motivations and freedom they have given me so that I could develop interest to everything occurring in life.

To my Mother-in-law Anna and my Mum for alternating with baby sitting during the last tense moments of the write up.

To my sun Bogdan who was born exactly at the end of the three experimental years and who has given me some nice leisure times.

Thank you to many people with whom I have had relaxing times at the university and to Sam Lawman, Boco Peric, Kafing Keita, Andrew Lerwill, David Willmer, Gary

Wells, Rob Morris, Christophe Trabi, Elizabeth Bemand and Haida Liang with whom I have shared the lab and which has made my work pleasant.

Finally thank you to my wife Marcjanna who has supported me throughout the whole project and who has raised many questions about my work from a point of view of a non-scientific person which is even more exciting because I needed to be creative in supplying answers. Also for her "special" encouragements during the writing up.

Sorry to those I have forgotten.

TABLE OF CONTENTS

CHAPTER III:

CHAPTER IV:

CHAPTER V:

CHAPTER VI:

ABSTRACT

This thesis presents investigations of liquid ingress and vapour uptake in different porous media including textile fabrics and activated carbons, monitored by means of a unilateral NMR instrument. The aim of this work is to assess protective materials which prevent toxic liquid ingress and toxic vapour uptake from contaminating materials and personnel. A high performance fabric made of a combination of coated and not coated fibres can provide extremely high protection against toxic liquids. By incorporating an adsorbent layer between two highly repellent layers, an "intelligent" fabric that can prevent complete penetration through the composite system by toxic vapours can be constructed. This project was undertaken with a low-field unilateral *profile* NMR Mouse® (MObile Universal Surface Explorer) which can collect signal from a thin and flat sensitive volume (*ca.* 1.5 cm x 1.5 cm x 0.6 mm) up to 10 mm above it, and in a non-invasive manner. The instrument uses a strong inherent magnetic field gradient (11.38 $T.m^{-1}$) in conjunction with pulsed radio frequency waves. The method makes use of Fourier Transformed NMR in order to spatially resolve 1D vertical profiles for each measurement over a field of view exceeding 500 μm and with a spatial resolution of 15 μm.

One system investigated was a laminate heterogeneous layered fabric, made of a horizontal stack of three individual layers, each 70 μm thick, constructed from entangled fibres of 10 μm in diameter. The top and bottom layers are strongly repellent to the oil used as a model that represents a simulant for a toxic liquid, whilst the middle layer is non-repellent and allows oil to absorb inside. The ability of the liquid challenge (source of hydrogen-containing molecules in the form of a droplet) to penetrate the textile structure depends on the external pressure applied to the droplet; the effect of this pressure is extensively investigated in this work. In further experiments, the middle layer of the fabric was replaced by an activated carbon cloth textile layer (200 μm thick) made of woven fibres. Activated carbon is an extremely powerful adsorbent into which one or more challenge(s) can be adsorbed at a time and has therefore a great aptitude to contribute to the effectiveness of protective textiles.

In this work it is demonstrated that the ingress of liquids as a function of pressure vertically applied to the top of the sample can be dynamically monitored via a vertical stack of 1D NMR profiles. It was possible to non-invasively and non-destructively quantify the amount of liquid penetrating into the middle non-repellent layer (or activated carbon cloth layer) as a function of pressure. The ability of unilateral NMR to monitor the adsorption process of vapours onto activated carbons cloths was also explored. The monitoring technique was extended to other types of activated carbons including monoliths and composites. Spatially resolved one dimensional profiles of both the transverse NMR relaxation rate (R_2) and the absolute quantity of adsorbate present at a given position across the selected slice were obtained for three different activated carbons (monolith, composite and cloth) which are challenging samples from the point of view of their electrical conductivity. The NMR amplitude is shown to strongly correlate with T_2 and, when calibrated, the NMR amplitude is shown to reveal the saturation level. The NMR relaxation rate reveals subtle information about pore filling, which allows quantitative assessment of the system's saturation level, without the need for calibration, provided that the molecule under investigation is known. Differing dynamic variations in R_2 are seen for one adsorbate to another. For the case of ingress into textile cloth layer, the data suggests that the bigger pores are filled before the smaller pores.

ACRONYMS

Here is an extensive list of acronyms used throughout the thesis.

NMR: **N**uclear **M**agnetic **R**esonance

MRI: **M**agnetic **R**esonance **I**maging

MOUSE: **MO**bile **U**niversal **S**urface **E**xplorer

CPMG: **C**arr-**P**urcell-**M**eiboom-**G**ill

SNR: **S**ignal to **N**oise **R**atio

MAS: **M**agic-**A**ngle **S**pinning

DSTL: **D**efence **S**cience and **T**echnology **L**aboratory

AC: **A**ctivated **C**arbon

ACNC: **A**ctivated **C**arbon **C**oco**N**ut

SC2: nutshell carbon

CF2 and JP2: sample codes for two different AC cloths

BPL: AC derived from coal

VOC: **V**olatile **O**rganic **C**ompound

RF: **R**adio **F**requency

FID: **F**ree **I**nduction **D**ecay

FOV: **F**ield **O**f **V**iew

FTIR: **F**ourier **T**ransform **I**nfra**R**ed

PW$_{360}$: 360° **P**ulse **W**idths

B_1: RF magnetic field

B_0: polarising field

τ : time duration of the CPMG sequence

T_R: repetition time

T_E: echo time

T_1: longitudinal relaxation time or spin-lattice relaxation time

T_2: transverse relaxation time or spin-spin relaxation time

T_2^{eff} : effective transverse relaxation time

R_2^{eff} : effective transverse relaxation rate

T_2^* : T_2 star

R_1: longitudinal relaxation rate

R_2: transverse relaxation rate

M_0: magnitude of the fully polarised nuclear magnetisation

M_y: longitudinal nuclear magnetisation

M_{xz}: transverse nuclear magnetisation

FWHM: **F**ull **W**idth at **H**alf **M**aximum

FA: **F**itted **A**mplitude

$\underline{i}^{'}$, $\underline{j}^{'}$ and $\underline{k}^{'}$: unit vectors of the rotating frame

θ: surface area covering

α: flip angle

θ_m: magic angle

φ: Young's contact angle

θ_{ap}: apparent contact angle

θ_a: advancing angle

θ_r: receding angle

θ_W: Wenzel contact angle

ψ: sliding angle

γ: gyromagnetic ratio

ω_0: Larmor frequency

ν_0: precession frequency of the nuclear spins in the magnetic field

ω_1: angular frequency of the precession of the nuclear magnetisation about B_1

ν_1: precession frequency of the nuclear magnetisation

δ: skin depth

μ: permeability

σ: conductivity

ω: angular frequency

σ_{SV}: surface tension between the solid and vapour phases

σ_{LV}: surface tension between the liquid and vapour phases

σ_{SL}: interfacial tension between the solid and liquid phases

ΔP: external applied pressure

P_{Lap}: Laplace pressure

P_i: pressure inside a droplet

P_{at}: atmospheric pressure

R: minimum radius of meniscus in a capillary tube

r: pore radius

η: viscosity of fluid

l: distance over which a pressure gradient acts

n: amount of volume of fluid

BET: **B**runauer-**E**mmett-**T**eller

BJH: **B**arrett-**J**oyner-**H**alenda

DR: **D**ubinin **R**adushkevic

V_m: monolayer coverage volume

V: amount of gas adsorbed

p/p^0: relative pressure

p^0: saturation pressure

n^a : equilibrium amounts of adsorbed gas or vapour

S/V : surface to volume ratio of a pore

ρ_1 and ρ_2: surface relaxation strengths

w: distance between the centre of the RF coil and the sensitive volume

PTFE: **p**oly**t**etra**f**luoro**e**thylene

ESE: **E**lectromagnetic **S**hielding **E**ffect

SE: **S**hielding **E**ffectiveness

GMS: **g**lyco**m**ono**s**accharide

TMP: **t**ri**m**ethyl **p**hosphate

DMMP: **di**methyl **m**ethyl**p**hosphonate

TEP: **T**ri**e**thyl **P**hosphate

CHAPTER I: INTRODUCTION: REVIEW OF PREVIOUS WORK FORMING THE BASIS FOR THE NEW RESEARCH

INTRODUCTION

The field of research in Nuclear Magnetic Resonance (NMR) and of Magnetic Resonance Imaging (MRI) is presently benefiting from a variety of work producing improvements of the hardware itself [1-4] and in the methods allowing to diagnose cancer and several other diseases [5-8].

The development of high performance textiles is the research aim of a number of organisations. Fabrics can be made of several layers, each possessing different protection properties so as to generate a multi functional product for various applications. One application is a multi-layered textile that provides a barrier to liquid and vapour challenges (defined in section II.1.2.4.). In this thesis, unilateral NMR is exploited to image both liquid and vapour uptake of the textile.

Key to the performance of fabrics that act as protection materials is the incorporation of a layer that can adsorb toxic vapours.

The carbon community benefits from a broad range of research applications that are currently being explored. For instance, the National Aeronautics and Space Administration (NASA) has invested funds in order to explore how carbon arrived and evolved on earth. Their next goal is to further explore the planet Mars [9-10] by excavating a two meters deep hole in order to extract information from the ground. Another outcome of recent research is that there resides a natural equilibrium between the earth (leaves and trees), the ocean and the atmosphere resulting from the exchange of 150 billions of tons of carbon per year. The industrial activities release more and more carbon dioxide (CO_2) which disrupts this equilibrium. Hervé le Treut tries to numerically simulate the earth climate [11]; "the increasing production of CO_2 plays a key role for the earth prediction climate". Less worryingly, carbon is extensively used in healthcare because of its high biocompatibility for implants [12]. Carbon is also at the core of nanotube technologies [13] in which a broad range of nanodevices are developed

such as nanoprocessors, solar cells, ultracapacitors, nano-Random Access Memory (nano-RAM), nanoscale electric motors (nanomotors).

Research on Activated Carbon (AC) was developed in combination with the growth of interest on carbon. The adsorption of gases and vapours onto porous media has been the subject of extensive investigations. AC is a widely used material for this application. The nature of the porosity of AC materials is usually determined by gravimetric or volumetric techniques that probe the pore structure of these substances. Other methods such as calorimetry [14] can provide details concerning chemical or physical adsorption, but little information is available on the dynamic effects occurring at the molecular level during the adsorption process. In this thesis the ability of unilateral NMR to monitor the processes of adsorption, desorption and the saturation of a vapour onto a porous carbon which is a challenging sample due to its electrical conductivity is explored.

I.1. Purpose of this specific research and relevant previous work

I.1.1. Aims and goals

The basis of this thesis work originated from a preliminary investigation carried out by the author during a two months summer research project conducted in 2006. The goal of this study was to determine whether it was possible to monitor a liquid ingressing into an optically opaque fabric by means of NMR. In this early work it was demonstrated that with a unilateral NMR instrument, a liquid invading a fabric can be monitored, with spatially resolved information across the thickness of the fabric, as in MRI. Following this, the main issue that this research further endeavoured to answer was whether the fate of a liquid ingressing into an AC cloth, and a vapour being adsorbed in an AC cloth/monolith could be spatially and temporally resolved using a specific unilateral NMR instrument.

In the first year, the research was focused on both repellent and non-repellent fabrics which were supplied by the Defence Science and Technology Laboratory (DSTL).

After one year of research, four different samples all made of four different forms of AC were provided by the DSTL and the study shifted focus from liquid ingress to the monitoring of vapour being adsorbed in AC using the same NMR instrument.

I.1.2. State-of-the-art concerning advanced fabrics

The design of liquid repellent fabrics is extremely important to industrial and domestic applications that seek to minimise, or prevent liquid ingress from contaminating materials and personnel [15-19].

The contact angle, φ, is a quantitative measure of the wetting of a solid by a liquid. It is defined geometrically as the angle formed by a liquid at the three phase boundary where a liquid (L), gas/vapour (V) and solid (S) intersect on an *ideal surface* (perfectly flat and homogeneous), see Fig.I.1. The contact angle of the droplet is determined by Young's relation [20], see Eq [I.1].

$$\sigma_{SV} = \sigma_{SL} + \sigma_{LV} \cos \varphi, \qquad\qquad \text{Eq [I.1]}$$

with: σ_{SV}: the surface tension between the solid and vapour phases,

σ_{LV}: the surface tension between the liquid and vapour phases,

σ_{SL}: interfacial tension between the solid and liquid phases and

φ: Young's contact angle.
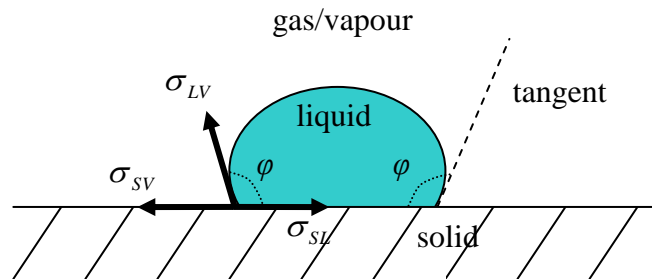
Fig.I.1: Sketch representing Young's contact angle φ of a liquid resting on a solid which is an ideal surface (flat and homogeneous). The theoretical description of the contact angle arises from the consideration of a thermodynamic equilibrium between the three phases.

18

In designing protective clothing, knowledge of how liquids will interact with a textile material under various conditions of wear is crucial. Léger and Joanny [21] reviewed the wetting and spreading properties of simple liquids on solid surfaces. They describe how with partial wetting the liquid does not spread completely and shows a finite contact angle on a solid surface, whereas in a complete wetting situation, the liquid forms a film on a solid surface with a thickness in the mesoscopic range.

If one considers a pool of liquid on a repellent heterogeneous fabric, to enter the pores a pressure must be applied to exceed the Laplace pressure of the curved meniscus for the smallest curvature it requires to enter this pore. As atmospheric pressure acts on all the points the pressure difference across the curved meniscus is the applied pressure (ΔP) and this must equal the Laplace pressure [22], P_{Lap}. Therefore, the pressure inside a droplet (P_i) is related to the external pressure applied to the droplet and to the atmospheric pressure (P_{at}) through the following equation [22]:

$$\Delta P = P_i - P_{at} = P_{Lap},$$
Eq [I.2]

also called the Laplace pressure, which can be written as:

$$P_{Lap} = \frac{2\sigma_{LV}}{R},$$
Eq [I.3]

where R is the is the minimum radius of the meniscus formed by the liquid in a capillary tube. R can be related to the pore radius (r) and contact angle (φ) by:

$$R = \frac{r}{\cos\varphi}.$$
Eq [I.4]

By combining Eq [I.3] and Eq [I.4], it is found that the external applied pressure is:

$$P_{Lap} = \frac{2\sigma_{LV}\cos\varphi}{r}.$$
Eq [I.5]

Critical information on how a liquid penetrates a fabric includes the pressure at which the liquid is forced into the substrate and, at that breakthrough pressure, the location of the ingressing liquid within the textile. If one assumes that the liquid is only penetrating into one (cylindrical) pore, the ingress of the fluid is subjected to the external pressure (ΔP) applied to the droplet, the entrance pore size radius (r) of the pore, the viscosity (η) of the fluid and the distance (l) over which the pressure gradient acts into a pore, *i.e.* how far into the pore the liquid has penetrated so far. The rate of change in the amount of volume of fluid (or the volume flow rate) can be found through the following equation [23]:

$$\frac{dn}{dt} = \frac{\Delta P \pi r^4}{8 \eta l}, \qquad\qquad \text{Eq [I.6]}$$

with n being the amount of volume of fluid. Eq [I.6] tells that as time goes on, l increases so dn/dt decreases and the flux slows down.

If there are a lot of parallel pores, all the same diameter, then the progress of the fluid into the material will also depend on how closely packed on the surface these pores are; obviously the closer together they are, the more fluid will enter. However, the determination of the location of the liquid inside the fabric is complicated. If the textile can be de-laminated then the separate layers can be analysed gravimetrically or the liquid residing in the individual layer could be extracted with a solvent and the corresponding amount of test liquid quantified by an appropriate spectroscopic technique (*e.g.* Fourier Transform InfraRed (FTIR), mass spectroscopy or gas chromatography). All of these methods are, however, either time-consuming, invasive/destructive or do not provide quantification of the amount of liquid that is able to penetrate into or through the fabric, and only supply a "snapshot" of the ingress process as opposed to a "dynamic" measurement.

In an ideal experiment, the textile would be imaged so that the fate of the liquid droplet could be determined whilst an external pressure was applied. X-ray tomography [24] and neutron radiology [25] have been used as non-contact techniques to analyse water (H_2O) distribution in fabrics, but the use of these as bench-top instruments is difficult. In this work, it is suggested and demonstrated that an alternative possibility for the non-

invasive quantitative monitoring of liquid ingress within an opaque and complex fabric is to use MRI.

This work hypothesises that the ingress of a liquid into a fluoropolymer coated fabric can be followed using the *profile* NMR Mouse®. In the literature MRI has been used for the determination of 1D profiles of moisture content and drying across the thickness of carpets [26-28]. A two-dimensional MRI investigation of water distribution in carpets has also been reported [28] but the substantial evaporation of water during the time duration (77 minutes) of the experiment prevented the workers from being able to produce quantitative data.

NMR microscopy has been used, for example, to follow the ingress of a dissolution medium, in this case a sodium phosphate buffer with pH 6.8, into small (sub-mm) lipophilic matrix theophylline beads [29]. In that work, Harding demonstrated that the total concentration of absorbed liquid increased and its T_2 relaxation time decreased with increasing glycomonosaccharide (GMS) content of the bead matrix, see Fig.I.2. In order to monitor this distribution of liquid within fully liquid penetrated beads, a 3D NMR imaging technique was used with a Bruker DRX 400 spectrometer equipped with a micro imaging probehead. This decrease in the liquid T_2 relaxation with increasing GMS content indicates stronger interactions of the liquid with the matrix material.
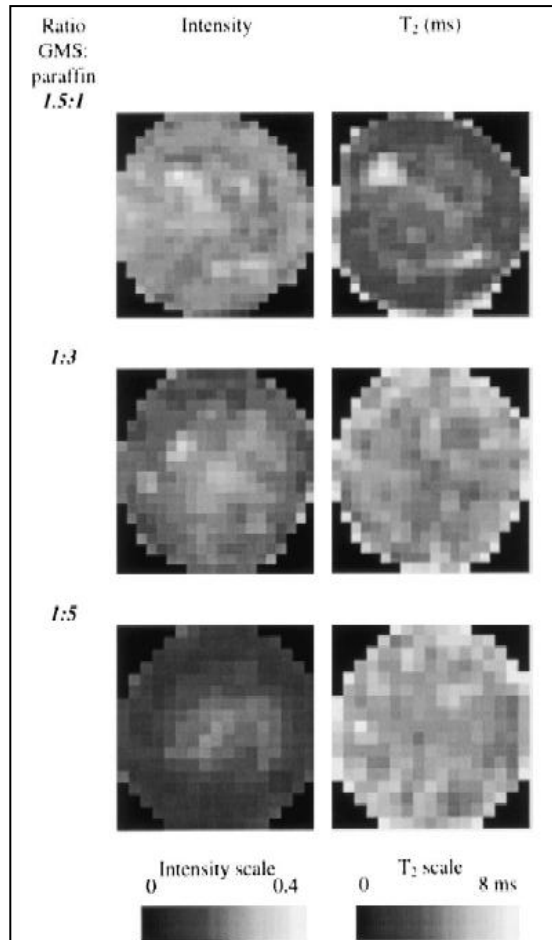
Fig.I.2: Selected 2D slices from 3D images of fully liquid saturated beads, (reproduced from Ref [29]). The images show signal intensity, after corrections for relaxation contrast, liquid T_2 relaxation times for beads with GMS:paraffin ratios of 1.5:1, 1:3 and 1:5. The mean liquid T_2 value decreases with increasing proportion of GMS in the matrix formulation. The signal intensity gives a measure of the fractional uptake of liquid by the bead.

I.1.3. Definition of activated carbon

Activated carbon is an extremely powerful adsorbent and can be produced from a variety of carbonaceous source materials including *e.g.* agricultural wastes. Commercial precursors of AC may be brown coal, peat, wood and in general materials containing lignin and cellulose [30]. Other commonly used precursors are bituminous coal, coconut shells, almond shells, hazelnut shells, walnut shells, pistachio-nut shells, peach and plum stones, grape seeds, eucalyptus kraft lignin, softwood bark residues, oil-palm shells, petroleum, pitch and polymers.

Generally, activated carbons can be prepared via a physical or a chemical method. The physical method, widely used in the industry, involves two stages, pyrolysis and then physical activation [31]. In the first stage, the starting materials are carbonised in an inert atmosphere at a moderate temperature (400-800 °C) to produce chars with rudimentary pore structures. Subsequently, in the second stage, the resulting chars are subjected to a partial and controlled gasification at a higher temperature (900 °C) with steam, carbon dioxide or air to produce the final activated carbons with well developed and accessible internal structures. Chemical activation is done by carbonisation of carbonaceous materials impregnated with chemical reagents [32].

Chemical activation is sometimes preferred over physical activation for its lower activation temperature and increased yield. Among the numerous chemical activants such as potassium hydroxide (KOH), zinc chloride ($ZnCl_2$), hydrochloric acid (HCl), etc., phosphoric acid (H_3PO_4) is widely used for this process as it can be removed easily after activation of the carbon by washing it with hot and cold water [32].

It is the achievement of small porosity network that makes carbon *activated*. This activation allows materials to bind physically by van der Waals forces to the surface of activated carbon, which is a process called physisorption [30]. However, if the adsorbate forms a bond with the adsorbent then chemisorption [30] occurs and is driven by a chemical reaction occurring at the exposed surface.

I.1.4. State-of-the-art of NMR measurements on activated carbon

In the following section a review of some of the work done on AC using NMR is given.

In the early 70's, general NMR work on activated carbons became of a sudden interest. Gradsztajn, Conard *et al.* [33] started to publish results taken using high resolution proton (^{1}H) NMR studies of adsorbates (defined in section I.1.5.) on carbon black (Carbolac in this case) and Activated Carbon CocoNut (AC NC). Carbon black [30] is an industrially manufactured colloidal carbon material produced by the incomplete combustion of carbon hydrogen compounds and has a well-defined morphology with a minimum content of tars which is a modified pitch. The surface area to volume ratio of carbon black can be three to four times lower compared to that of activated carbon. Conard *et al.* studied extensively the monomolecular layer covering on carbons [33, 34]. The main findings of their work were based on results of NMR chemical shifts and line widths of proton NMR. The surface area covering was recorded with both water and benzene vapours (C_6H_6) during adsorption on both Carbolac and AC NC. Conard explains that the chemical shifts of protons are related to the nature of the carbon and are almost independent to the nature of the adsorbed liquid and from its resonating nucleus. In addition, the chemical shift decreases when the surface area covering θ increases, see Fig.I.3, with θ being the number of monomolecular layers which was evaluated with the BET surface method [35, 36], also called the BET method (details of which are given section in I.1.5.). BET stands for Brunauer, Emmett, and Teller, the three scientists who optimized the theory for measuring specific surface area (definition given in section I.1.5.). Conard explored the causes of the chemical shifts. He showed that one of them is the physical interaction between non-paired electrons and nuclear spins. Another cause is the deformation of the electronic cloud of adsorbed molecules. Such interactions can cause chemical shifts which are dependent on the type of the adsorbed molecules. Diamagnetic anisotropy of crystallized parts of carbon is also responsible for some of the observed chemical shift.
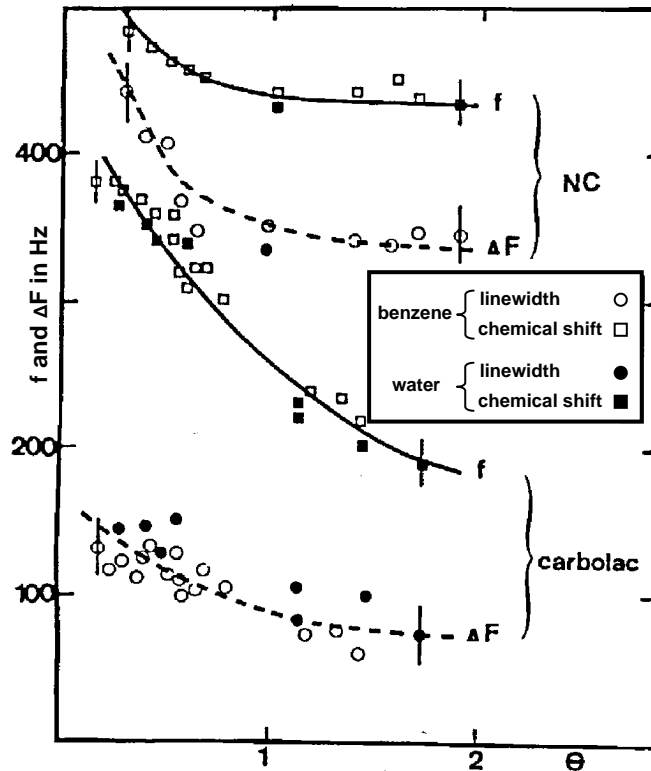
Fig.I.3: Relationship between the surface layer covering and both the protons NMR chemical shift and line width, (reproduced from Ref [33]). During adsorption of water and/or benzene on AC NC and/or on carbolac, the line width decreases by up to 100 Hz, and chemical shifts up to 200 Hz may be seen. The chemical shift observed for carbolac is greater than that seen for AC NC mostly due to the differences in the shape of their pores which is related to the diamagnetic susceptibility of the adsorbent.

In Conard's work the NMR spectral peak's frequency is not only displaced, but the line width is also shown to vary with the polarising field, with the temperature and with the surface area coverage. Two types of NMR line widths are measured resulting from the two different ACs (carbolac and AC NC). On one hand, the line width from adsorbed liquids may be called "homogeneous" which means that it stays constant when B_0 (defined later in section II.1.1.) varies (15.1, 56.4, 60 MHz). This is the case for carbolac and is due to a spherical shape of the pores. One the other hand, the line width from adsorbed liquids may be called "inhomogeneous" which means that it varies with B_0. This is the case for AC NC and is explained by the fact that the pores are not spherical, see Fig.I.4.
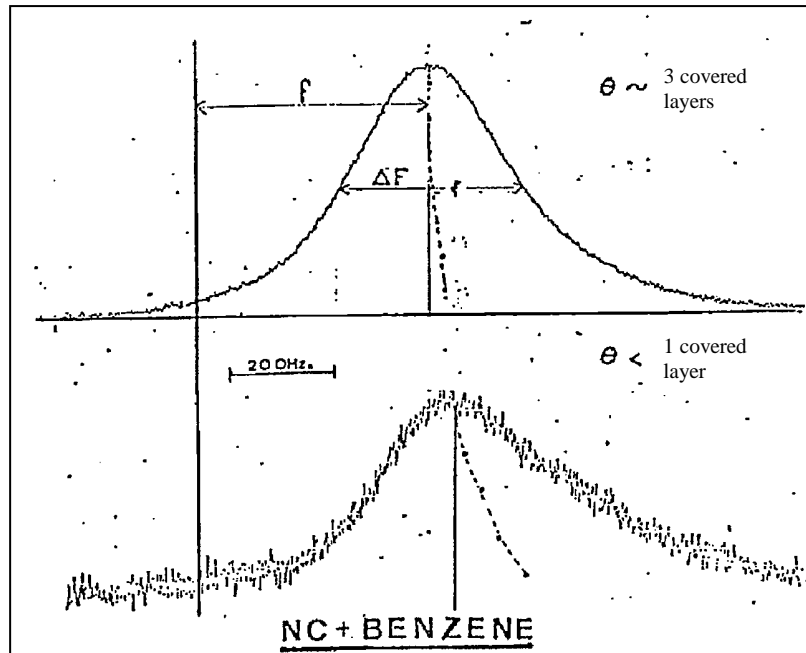
Fig.I.4: Benzene adsorbed on AC NC measured for a B_0 of 60 MHz, (reproduced from Ref [33]). When less than one layer is covered, the asymmetry of the line width is more pronounced than for a surface covered with three layers. Note that the vertical axis represents ^{1}H NMR signal strength.

In another work undertaken by the same research group [34], it was demonstrated that the adsorption of molecules with OH and CH groups (from formic acid HCOOH) on carbolac, also causes associated chemical shift and line width decrease, see Fig.I.5.
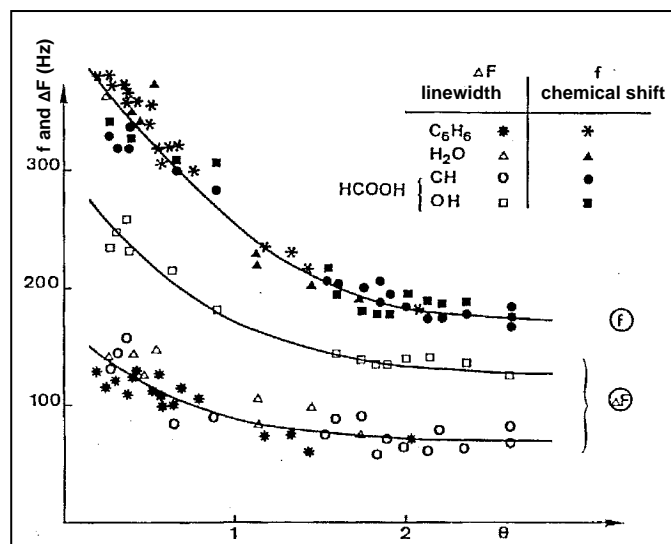
Fig.I.5: Relationship between the surface layer covering and both the proton NMR chemical shift and the line width, (reproduced from Ref [34]). In addition to data similar to that seen in Fig.I.3, Fig.I.5 also comprises information about molecules containing the CH and OH groups during adsorption on carbolac. The line width of CH and OH decreases during adsorption.

Le Cloirec *et al.* [37] obtained, with proton NMR, qualitative and quantitative information on proton-containing molecules (H_2O, and phenol (C_6H_5OH)) adsorbed in either fresh AC or phenol-saturated AC. A Bruker SXP 4-100 spectrometer was used to perform high resolution ^1H NMR at 20 and 90 MHz on AC (Picatif NC60). The spin-spin relaxation time, T_2, was determined from the Carr-Purcell-Meiboom-Gill (CPMG) pulse sequence or from the 90-τ-180 pulse sequence (for the lowest values, smaller than 1 ms). The measurements of 400 mg of each (pre-adsorbed) different sample give an insight about dynamic behaviours of the adsorbed molecules. A typical shape of the Free Induction Decay (FID) is plotted in Fig.I.6.
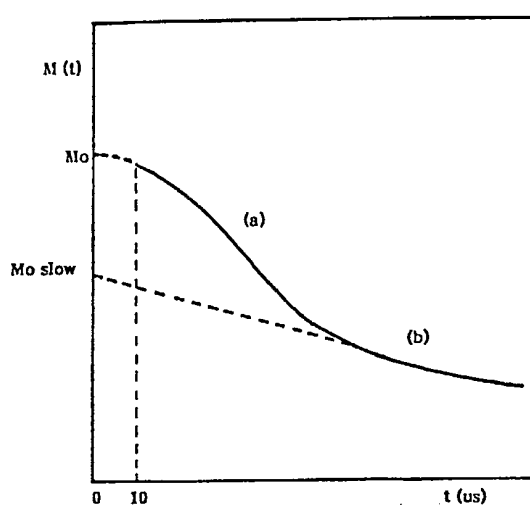
Fig.I.6: Characteristic signal of the FID observed for the AC samples, (reproduced from Ref [37]). Two parts are observed in the curve: **(a)** a fast decay during the first 50 μs and **(b)** a slow exponential decay. It is reported that although the shape of the FID is very similar for each sample, the absolute and relative amplitudes differ a lot.

The slow decay is attributed to the protons of water molecules that diffuse quickly in the inner structure of the AC. These mobile water protons are less numerous (1/2.5) in the sample saturated with phenol. Indeed, the adsorbed water covers the entire porous surface in a fresh AC; whereas when the AC saturated with phenol is exposed to the adsorption of water, this results in the displacement of 40% of phenol (which is replaced by water).

The fast decaying FID is assigned to adsorbed phenol molecules bonded ($\equiv C-H$) to the AC structure with no translational or rotational motion around their axis; which means that these motions are too slow to reduce the proton line width.

Adsorption onto activated carbon has also already been studied extensively with Magic-Angle Spinning (MAS) NMR. This technique consists of spinning the sample (usually at a frequency of 1 to 70 kHz) at the magic angle θ_m (*ca.* 54.74°) with respect to the direction of the magnetic field. By doing this, the normally broad lines become narrower, increasing the resolution for better identification and analysis of the spectrum. The main drawback of this technique is that the sample is located inside the bore of the superconducting magnet which restricts the user to batch sampling where the adsorbent has been pre-adsorbed, or to conducting the experiment inside the bore of the magnet. The latter can be practically challenging, particularly when performing MAS experiments.

As a result of the highly toxic nature of organophosphorus compounds, there is considerable interest in the use of AC in air purification filters. As a consequence experimental techniques such as MAS NMR have been used to probe adsorption behaviour. For example, on a study done using MAS Phosphorous-31 (^{31}P) NMR [38], adsorption of an organophosphate (trimethyl phosphate, TMP, $C_3H_9PO_4$) and of an organophosphonate (dimethyl methylphosphonate, DMMP, $C_3H_9PO_3$) was recorded on the porous system of a nutshell carbon (SC2) at 81.014 MHz using a Chemagnetics CMX 200 spectrometer with a 7.5 mm o.d. pencil rotor situated in an MAS probe. The MAS speed employed was 1.2 kHz. ^{31}P NMR was carried out rather than ^{1}H NMR or ^{13}C NMR, in part because phosphorus-containing substrates are of substantial interest but also partly because of the highly-favourable characteristics of the phosphorus nucleus as compared with ^{13}C for example: 100% natural abundance (1.1% for ^{13}C) and high magnetic moment ($\gamma(^{31}P)/\gamma(^{13}C)=1.6$). Thus, spectra can be obtained in short times even at quite low loadings (*e.g.* 10% w/w). In that work, it was found from the spectra that the amount of adsorbed material within the pore system can be accurately obtained by measurement of the areas under each peak in the ^{31}P spectrum as a function of time and that a quick initial adsorption is followed by a slower process as the adsorbate material enters less accessible smaller pores, see Fig.I.7. Two experiments were studied by the addition of 50% w/w TMP to SC2 carbon with 50% w/w DMMP pre-adsorbed, and the inverse experiment, adding 50% w/w DMMP to SC2 with 50% w/w TMP pre-adsorbed. The samples were left for 2 hours between the addition of the first and second adsorbate, which were both added as liquid by using a microsyringe.
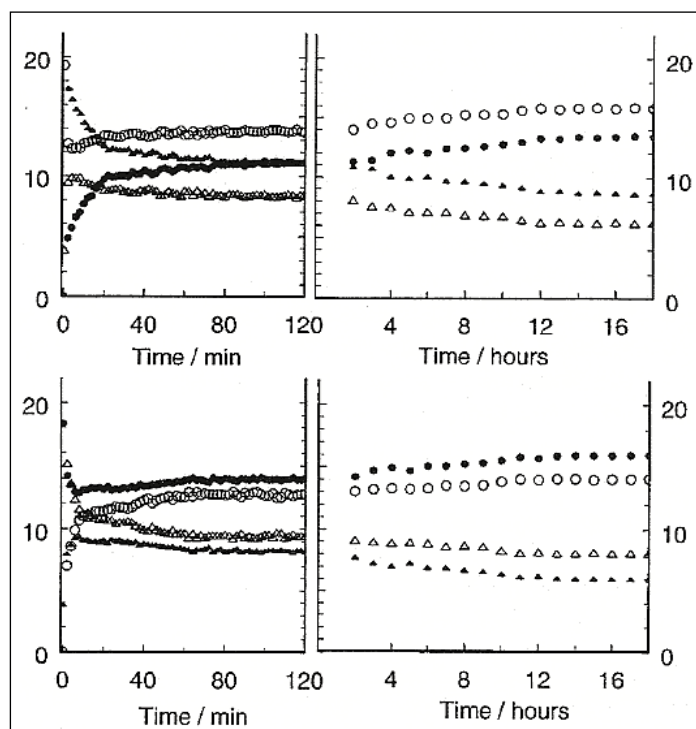
Fig.I.7: Variation in peak areas, in arbitrary units, of each adsorbate with time elapsed after the addition of the second adsorbate, (reproduced from Ref [38]). The top plots illustrate the addition of 50% w/w DMMP (filled symbols) upon SC2 with 50% w/w TMP (hollow symbols) pre-adsorbed. The lower plots illustrate the converse experiment. The low frequency peak (with a broad peak area) is represented by circles and the high frequency peak (with a narrow peak area) is represented by triangles. Each phosphorus-containing compound gives two resonances (a sharp peak appearing at a chemical shift indistinguishable from that of the liquid material and a broad peak shifted by *ca.* 8 ppm to lower frequency) when added to the carbon adsorbent, therefore the plots may be characterized by a double exponential function, each described by a substantially different half-life. The initial quick adsorption process, which corresponds to adsorption within the more accessible porous volume, occurs within the first 2 minutes of adsorption onto the clean carbon surface. It can be accounted for by an exponential function with a half-life on the order of tens of seconds. The second exponential function describes the adsorption of a much smaller proportion of the adsorbate and has a half-life typically on the order of several hours corresponding to the entrance of molecules into progressively smaller pores.

In both cases they observed that the final chemical shift for each material is at slightly higher frequency than that observed for the adsorbate in the experiments performed on the adsorption of 50% w/w of each material. This shows that the average pore size explored by the adsorbate molecules has increased in size relative to the pore size explored prior to the addition of the second adsorbate.

A limitation with MAS NMR arises though because of:

- the time required to obtain NMR spectra; in this case for ^{31}P it takes 2 minutes to achieve the first one and thereafter every 48 seconds (with a recycle time of 3 seconds and accumulating 16 acquisitions) whereas it takes about two hours for ^{13}C;

- the time delay (typically 10 minutes) introduced after the adsorbate addition - in the cell under investigation hosting the AC sample - due to the need to insert the sample holder into the spectrometer and initiate MAS so that the sample is spun at the requisite speed.

In addition, another ^{31}P-containing molecule (Triethyl phosphate, TEP, $C_6H_{15}PO_4$) has been explored using ^{31}P MAS NMR by this same research group [39]. In this work, the NMR data was obtained (with the same MAS spectrometer) on the adsorption of DMMP, TMP and TEP on AC derived from coal (BPL). The spectra reveal that at low loadings a broad resonance band is seen at *ca.* 8 ppm to low frequency of the signal for the neat liquid adsorbate, see Fig.I.8 (upper curves). This broad signal may be assigned to strongly adsorbed molecules (probably in rapid exchange with nearby relatively free molecules, at least in the larger channels) in micropores and mesopores. At higher loadings a sharper peak appears, arising from less-strongly adsorbed molecules at surfaces and domain interfaces, see Fig.I.8 (lower curves).
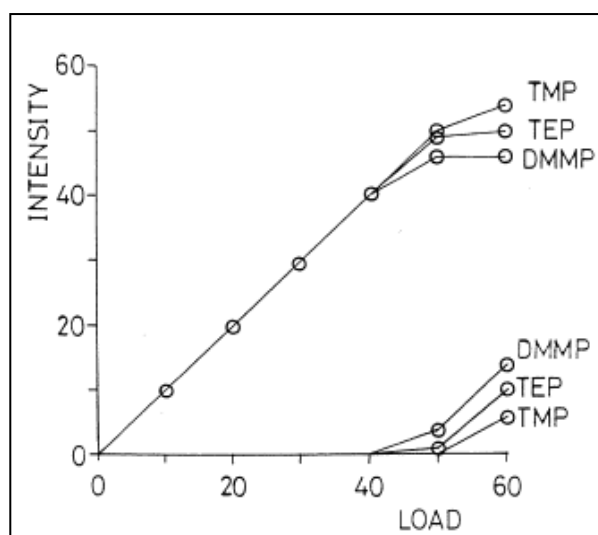
Fig.I.8: Plots of intensity (integrated peak area, arbitrary units) versus w/w% adsorbate load for (upper curves) the broad peak, and (lower curves) the sharp peak for the adsorption of TMP, TEP and DMMP on BPL, (reproduced from Ref [39]).

I.1.4.1. The electrical conductivity of activated carbon in the context of NMR measurements

Because of its good conductivity, AC is a difficult candidate for NMR/MRI. One main difficulty is to control the currents induced in AC during an NMR experiment. Graphite fraction, in particular, in carbon distorts the NMR spectra. This phenomenon has been associated with the magnetic susceptibility [40] and the conductivity [41] of carbonaceous materials. These two factors - the magnetic susceptibility and the conductivity (which causes the electromagnetic shielding effect (ESE) of electromagnetic radiation) of carbon materials - complicate the design of NMR experiments where ideally non-conductive and non-metallic samples should be used.

In recent work, Melguizo-Guijarro *et al.* demonstrate [42] that the ESE of carbons influences the NMR spectra thus resulting in a very low sensitivity. In that study the shielding effect was measured as the Shielding Effectiveness (SE). The NMR spectra were acquired in a Bruker Avance 500 instrument equipped with a standard-bore 11.74 T superconducting magnet operating at 500.13 MHz for ^{1}H and 125.76 MHz for ^{13}C. A Bruker, two channels MAS, broadband probe (Bruker X/H CP-MAS) for 4 mm diameter sample rotors was used. The samples for NMR measurements were conditioned in standard 4 mm zirconia MAS rotors of 80 µL capacity. All the NMR experiments were performed at MAS rotation frequencies between 4 and 12 kHz. The SE is expressed in units of decibels (dB) and can be calculated from the values of the 360° pulse widths (PW_{360}) measured in NMR experiments. PW_{360} is the B_1 (defined later in section II.2.2.) Radio Frequency (RF) transmit power that produces flip angles of 360° for the adamantine ($C_{10}H_{16}$) sample when shielded by a mixture containing carbon. SE is given by the following equation:

$$SE = 20 \log_{10}\left(\frac{PW_{360}}{PW_{360}^0} \right), \qquad \text{Eq [I.7]}$$

with PW_{360}^0 the pulse width measured for the irradiation power received by the adamantine sample without carbon shielding effect (rotor filled with pure silica gel).

The PW$_{360}$ for ^{1}H and ^{13}C were measured for a sample of adamantine contained in a glass capillary inside the zirconia rotor that is surrounded by a shield of AC-silica mixture going from pure AC to pure silica; those measurements gave rise to the their corresponding ^{1}H and ^{13}C spectra (at different shielded arrangement). These spectra of adamantine were acquired by means of 90° pulses calibrated according with the PW$_{360}$ measured. The ESE of the AC-silica mixture on the radiofrequency entering the sample and that on the NMR signal coming out from the sample were measured separately as the radiofrequencies generated by the probe coil have to go across the sample to produce the nuclei excitation (inward way) and later, the emitted radiation has to come out across the sample to reach the receiver coil (outward way), see Fig.I.9.
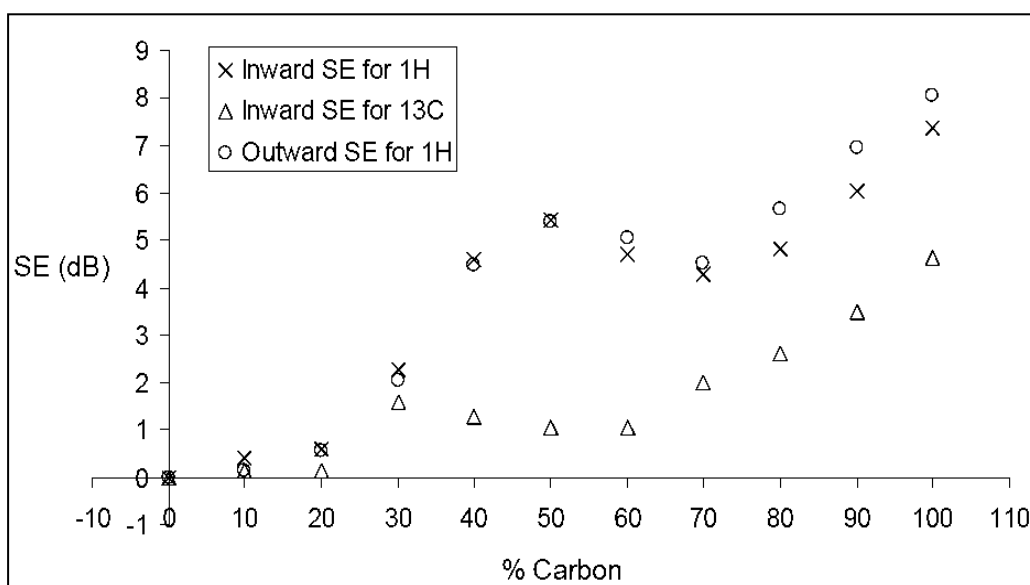
Fig.I.9: Experimental data obtained for the SE (in dB) of AC-silica mixtures for the electromagnetic radiation of frequencies corresponding to NMR of ^{1}H and ^{13}C, (reproduced from Ref [42]).

After comparing the SE at the two different frequencies it can be said that (i) the trend in the evolution of the SE values along the whole dilution range (100 - 0% carbon) has the same profile for both frequencies, and (ii) the SE values are significantly higher for the higher (^{1}H) frequency in most of the dilution range (100 - 40% carbon). The shielding effect is the highest with the presence of 100% of carbon, and it also exhibits an interesting secondary maximum, for 30% or 50% carbon depending on the nucleus under investigation, that the authors seem to relate to the attainment of the threshold of percolation conductivity [43].

I.1.5. Introduction to the characterisation of activated carbons

The size of the pores found within an AC can be differentiated into three categories:
1. micropore for diameter smaller than 2 nm;
2. mesopore for diameter between 2 and 50 nm;
3. macropore for diameter greater than 50 nm.

In experimental adsorption systems, the gas or vapour is called "the adsorptive" when not in adsorbed state, and "the adsorbate" when existing as an adsorbed phase within a solid, which is referred to as the adsorbent. Note that, at room temperature, a vapour is a substance which has experienced a phase change, whereas a gas is a substance which has not, and will not experience a phase change. The plot of the equilibrium amounts of adsorbed gas or vapour n^a (in mmol.g^{-1} or in cm^3.g^{-1}) against the relative pressure (p/p^0) of the adsorbate at constant temperature makes up the adsorption isotherm. With p^0 being the saturation pressure (in Pascal) which corresponds to the room pressure. The adsorption of gases and vapours is a physical process (physisorption), not involving formation of chemical bonds [30]. The progressive occupancy of adsorption sites is not a random process but one of selecting the next best available site, from an energetic point of view. In adsorption studies, the experimental isotherms of nitrogen (at 77.35 K), see Fig.I.10, carbon dioxide (at 273 K) and water vapour provide considerable information by visual inspection (for an experienced researcher) and quantitative analysis. Isotherms can supply the characterisation of a range of porous solids but are most commonly used for activated carbons.
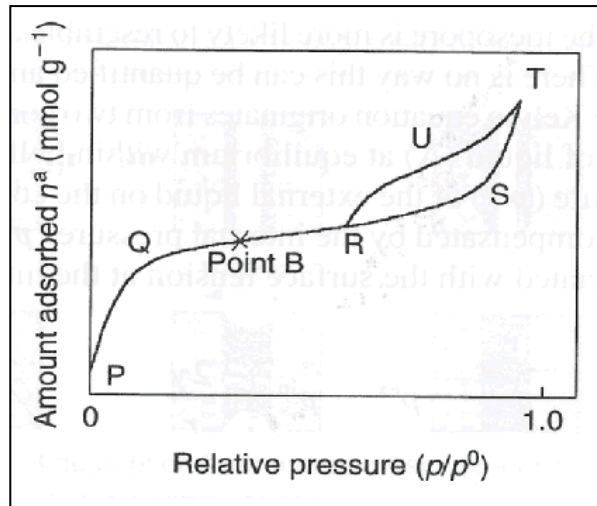
Fig.I.10: Adsorption isotherm of nitrogen, at 77.35 K, on a carbon containing both micro- and mesoporosity, and exhibiting a closed hysteresis loop on desorption, (reproduced from Ref [30]). n^a is a typical notation to represent the weight of adsorbate at relative pressure p/p^0).

From the visual inspection of the isotherm shape several characteristics of the AC can be extracted concerning the porous network into which the adsorption process has occurred such as:

- The presence of a hysteresis indicates the existence of mesoporosity because in these pores the mechanism of filling differs from that of emptying.

- The absence of the point of inflection (called **point B**, defined later on) indicates a stronger adsorbate-adsorbate than adsorbate-adsorbent interactions.

- If the point of inflection (**point B**) is present, the monolayer covering (completed at point B) can be separated from the multi-layer covering processes.

- The shape of hysteresis is an indicator of the geometry of the pores (cylindrical (*or slit-shape)*, spherical *(or bottle neck)*, cone shape, irregular…).

- For certain types of isotherm, the gradients of the initial part of the isotherm, from p/p^0 values from zero to about 0.05, are indicative of the dimensions of the microporosity, the steeper the gradient, the smaller are the micropores.

A qualitative interpretation of Fig.I.10 can be done by breaking the isotherm into different parts [30]. The **PQ** section describes adsorption in the microporosity. The **QR** section describes the continuation of the adsorption process, reversibly, into the smallest of the mesopores. For a totally microporous carbon the isotherm will have

34

levelled horizontally from position **Q**. The **RS** section describes the progressive filling (capillary condensation) of all other mesopores in the carbon concluding with the largest of the mesopores at position **S**. If macropores are present in the carbon, the section **ST** needs to be taken into consideration, conversely the position **S** merges with the position **T**. However, on lowering the pressure of the nitrogen in the equipment, the desorption isotherm does not follow the **SR** curve but the **SUR** (or **TUR**) one thereby creating a hysteresis loop closing at point **R**. The adsorption line describes equilibria of gaseous adsorbate over a curved meniscus on the internal surface of a cylinder whereas the desorption line describes equilibria of gaseous adsorbate over a curved meniscus (semi-spherical) at the end of a cylinder filled with liquid nitrogen, see Fig.I.11.
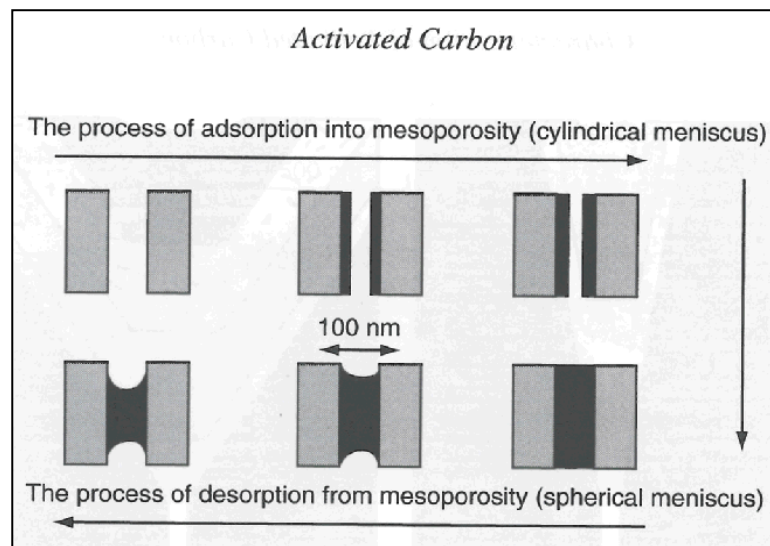
Fig.I.11: Adsorption in mesoporosity: a possible cause of hysteresis (irreversible adsorption-desorption processes), (reproduced from Ref [30]).

Coming back to the description of Fig.I.10, both the adsorption and desorption parts of the isotherm can be used to calculate the pore size distribution and results are essentially in agreement with each another. If the **RS** section is vertical then this indicates that all of the mesoporosity is of one size. As examples, a p/p^0 value of 0.90 corresponds to a pore size of 10 nm, a p/p^0 value of 0.95 to a pore size of 20 nm increasing to 200 nm at value of p/p^0 of 0.995. Note that experimentally, for such high relative pressures, it may be difficult to maintain the sample at the boiling point of nitrogen (77.35 K). An actual temperature of 77.40 K results in an error of 40% in assignments of pore size. Characteristically, the hysteresis loops in all isotherms close before reaching a relative pressure of 0.3 in the desorption process except when microporosity is present.

From the quantitative analysis the following results can be obtained [30]:

- The adsorption capacity.

- The pore size distribution of the carbon matrix.

- The presence of porosity with entrance dimensions smaller than *ca.* 0.7 nm diameter.

- The presence of sites of high adsorption potential, effective at low relative pressures of the adsorptive.

- The polarity of the surface of the carbon adsorbent (*e.g.* presence of surface oxygen complexes).

Some of this quantitative information can be extracted by the use of two separate methods: the BJH (Barrett-Joyner-Halenda) method [44] *(used as a measure of multi-layer coverage)* and the BET method [35, 36] *(used as a measure of monolayer coverage)*. The Kelvin, the Langmuir, BET and DR (Dubinin Radushkevic) equations are used to interpret isotherms and are central to the characterization of porosity in solids [30]; they are given in appendix A.

This BJH method uses the Kelvin equation in a modified fashion and allows to calculate the averaged pore size distribution. The Kelvin equation predicts the pressure at which the adsorptive will spontaneously condense (and evaporate) in a cylindrical pore of a given size. Condensation occurs in pores that already have some multilayers on the walls, therefore the Kelvin equation is exploiting the isotherm (Fig.I.10) for high relative pressures.

The Langmuir equation is a limiting case of the BET equation for the adsorption of a single molecular layer coverage of adsorbate and is used in the absence of meso- and/or macro- pores. The BET equation leads to the BET method which is most widely used and allows the determination of the specific surface area of the totality of the pores. The Langmuir and BET equations could be described as curve-fitting equations. The BET equation linearizes that part of the isotherm that contains the "knee", for relative pressures below 0.3-0.5 (see Fig.I.10). The equation can be solved by graphical means, by plotting $1/\left(V\left(p^0/p\right)-1\right)$ versus p/p^0, with V the amount of gas adsorbed at a relative pressure p/p^0. The monolayer coverage volume (V_m) is obtained from the slope

(s) and the y-intercept (i) and is equal to $1/(s+i)$. On the other hand, the DR equation can be solved by plotting $\log(V)$ versus $\log^2(p^0/p)$ which linearizes the isotherm based on micropore filling principles. The best fit is extrapolated to $\log^2(p^0/p)$; (*i.e.* where $p/p^0 = 1$) to find the specific micropore volume.

Moreover, in order to give a meaning to those last three equations, they can be linked [30] to Fig.I.10. They use different parts of the isotherm in their predictions of monolayer coverage. The DR equation exploits the initial segment **P** to **Q**, of the isotherm obtained at low pressures. The distribution of adsorption energies predicted from the higher relative pressure regions of the isotherm may or may not exist within a given carbon. The Langmuir equation is based on segment **PQB** where it is assumed that monolayer coverage takes place, whereas segment **QRS**, dealing with pore filling and capillary condensation process, forms the basis for the BET equation as applied to porous solid. **Point B** is the point of inflection of the isotherm where it is assumed that monolayer formation is complete. For most activated carbons, the limit of application of the Langmuir and DR equations is for relative pressures smaller than 0.15.

A last point to be clarified is the term "specific surface area", within the context of adsorption science. This term has been in use since the early days of the development of the Langmuir and BET equations of adsorption and is used for comparison purposes between AC materials. Specific surface area (in $m^2.g^{-1}$) is defined as the ratio between the absolute surface area of a solid and its mass. "Specific surface area" of porosity is widely used in the literature and is a convenient way to indicate adsorption capacity but it must not be confused with the geometrical meaning of a surface area (in m^2). Specific surface area is a "folded surface" creating pores [30], per unit mass of porous material. For the same reason, the specific volume of a pore is a volume per unit mass of a solid and is given in $cm^3.g^{-1}$.

I.2. Novelty of the work covered in this research

In addition to the well known applications in the medical imaging area, NMR can allow the user to non-invasively monitor on-line the quality control on a variety of products such as the detection of moisture [45] in soil [46-50], concrete bridge decks [46, 51], building materials [51, 52] and food [53-59].

In my work the *profile* NMR Mouse[®] [60] is used, which is a simple bench-top instrument, to quantitatively monitor the ingress of oil into a model fabric consisting of three layers of meltblown polypropylene, $(C_3H_6)_n$, fibres with the outer layers possessing a fluoropolymer coating. Experiments are presented whereby the applied pressure is varied, the droplet volume is constant and NMR observation is used to assess whether liquid ingress has occurred. The results show that it is possible to obtain spatially resolved one dimensional profiles of the absolute volume of liquid present at a given position across a selected slice of the fabric as liquid ingresses. With the same instrument, the adsorption, desorption and saturation of several vapours into different types of AC are monitored. Those are challenging samples due to their conductivity. It is found that in those samples, adsorption, desorption and saturation of a gas can be monitored by observations of the evolution of the signal intensity as well as the transverse relaxation rate and in some cases by observations of the longitudinal relaxation rate.

CHAPTER II: THEORY AND INSTRUMENTATION

INTRODUCTION

The phenomenon of NMR was discovered just after the Second World War by Purcell [61] and Bloch [62]. Later, from NMR, MRI was born in Nottingham in 1973 with Mansfield [63] (and with Lauterbur [64]) who pioneered magnetic field gradient coils that were added to the polarising field in order to be able to spatially encode the NMR signal frequency, although the first patent in MRI was awarded to Damadian [65] in 1974. In this chapter, basic NMR will be explained including a classical description of T_1 (longitudinal relaxation time) and T_2 (transverse relaxation time), after which, the *profile* NMR Mouse® instrument will be presented.

II.1. Description of NMR

II.1.1. Principles of NMR

When magnetic moments coming from a multitude of nuclei are added, the quantity obtained is referred to as the magnetic polarisation of the nuclei or the nuclear magnetisation. When subjected to a strong enough permanent magnetic field the nuclear spins (of hydrogen atoms) tend to align with it resulting in non-zero macroscopic nuclear magnetisation. The polarising field - also called the B_0 field - can be created either by a permanent magnet or by an electromagnet or a superconducting magnet. At room temperature and at a given B_0 field, only a small fraction of nuclei reaches a higher energy state and contributes to the macroscopic nuclear magnetisation [66]. The physical mechanism that opposes the nuclear polarisation is thermal energy. When B_0 polarises the system, the number of spins, N_{high}, found in their high energy level ("corresponding to non-polarised spins") is related to the number of spins, N_{low}, found in their lowest energy level ("corresponding to polarised spins") by the Boltzmann distribution:

$$\frac{N_{high}}{N_{low}} = \exp\left(-\frac{\gamma \hbar B_0}{kT}\right), \qquad\qquad \text{Eq [II.1]}$$

where γ is a constant characteristic of the nucleus under investigation, called the gyromagnetic ratio, h is the Planck constant ($h = 2\pi\hbar = 6.626068 \times 10^{-34}$) m^2.kg.s^{-1}, B_0 is the strength of $\underline{B}_0$, k the is Boltzmann constant ($k = 1.3806503 \times 10^{-23}$) m^2.kg.s^{-2}.K^{-1} and T the temperature in Kelvin.

For the case of the NMR instrument, with proton nuclei having $\gamma = 2.68 \times 10^8$ rad.s^{-1}.T^{-1}, at room temperature, and a polarising field of 0.25 Tesla, the percentage of polarised spins,

$\left(\dfrac{N_{low} - N_{high}}{N_{low} + N_{high}}\right) \times 100$, is only 0.000 086%.

Some nuclei such as ^{1}H, ^{2}H, ^{13}C, ^{14}Na, ^{19}F, ^{31}P or ^{129}Xe possess a non-zero spin which means that they have a magnetic moment combined with angular momentum, $\underline{L}$. If the number of neutrons and the number of protons are both even for a given atom, the nucleus has no spin. The nuclear magnetisation is due to an assembly of non-zero nuclear spins. In the quantum mechanical description of NMR the nuclear spins are described as an operator. However, classical physics consider a simpler description of NMR with the nuclear magnetisation as a macroscopic vectorial quantity. When a spin (for spin 1/2) is placed in a magnetic field, there is a component of the magnetic moment of the spin that points either parallel or anti-parallel to the magnetic field. These two spin orientations form a two-level system: *i.e.*, a system that has two states and a definite energy difference, or splitting, between them. Here the anti-parallel orientation has the higher energy. These spins precess about the direction of the B_0 field with an angular frequency, ω_0, proportional to the nuclear gyromagnetic ratio, γ, and to B_0 at the Larmor frequency ω_0 given by:

$$\omega_0 = \gamma B_0 = 2\pi\nu_0, \qquad\qquad \text{Eq [II.2]}$$

with:

ω_0: the "Larmor frequency" or angular frequency of the precession of the spin magnetisation about B_0,

γ: gyromagnetic ratio of the nuclei, equal to 2.68 x 10^8 rad.s^{-1}.T^{-1} for protons.

B_0: strength of polarising field,

ν_0: precession frequency of the nuclear spins in the magnetic field.

When subjected to an external $\underline{B}_0$ field the nuclear magnetisation $\underline{M}$ experiences a torque, $\underline{\tau}$, given by the product:

$$\underline{\tau} = \gamma \underline{M} \times \underline{B}_0 .$$ Eq [II.3]

Furthermore, from the classical equation of dynamics (or from Newton's second law of dynamics), if an external torque, $\underline{\tau}_{ext}$, is applied to a solid body possessing an intrinsic angular momentum, $\underline{L}$, the following equation is obtained:

$$\frac{d\underline{L}}{dt} = \underline{\tau}_{ext} .$$ Eq [II.4]

It is the same equations of motion that dictate the behaviour of nuclear spins experiencing an externally applied magnetic field, $\underline{B}_0$. In this case, the torque experienced by the magnetisation vector, $\underline{M}$, is given by the vector product $\gamma \underline{M} \times \underline{B}_0$, therefore by substituting Eq [II.3] in Eq [II.4], the following equation is obtained:

$$\frac{d\underline{M}}{dt} = \gamma \underline{M} \times \underline{B}_0$$ Eq [II.5]

which is also called the Bloch equations. The Larmor frequency, ω_0, from Eq [II.2] is derived from the Bloch equations. Furthermore, the Bloch equations can be used to calculate the nuclear magnetisation $\underline{M} = (M_x, M_y, M_z)$ as a function of time and can include the effects of transverse and longitudinal relaxations, by assigning $\underline{B} = B_0 \underline{j}'$, in which case they read as follows in a vector notation [67]:

$$\frac{\partial \underline{M}(\underline{r},t)}{\partial t} = \gamma \underline{M}(t) \times \underline{B}_0(\underline{r}) - \frac{M_x(t)\underline{i}' + M_z(t)\underline{k}'}{T_2} - \frac{M_y(t) - M_0}{T_1}\underline{j}', \quad \text{Eq [II.6]}$$

with:

T_1: longitudinal relaxation time or spin-lattice relaxation time,

T_2: transverse relaxation time or spin-spin relaxation time.

$\underline{i}'$, $\underline{j}'$ and $\underline{k}'$ are unit vectors corresponding to the rotating frame, which is a non-inertial reference frame (frame of reference that is under acceleration or deceleration) that is rotating relative to an inertial reference frame (frame of reference which describes time homogeneously and space homogeneously in a time independent manner).

An extra term, representing the contribution of molecular diffusion to the rate of change of magnetisation considered as macroscopic fluid [67], can be added and will be:

$$D\nabla^2 \underline{M}, \quad\quad\quad\quad\quad \text{Eq [II.7]}$$

with D being the self diffusion coefficient in $m^2.s^{-1}$. This expression results from Fick's equation, see appendix B.

The longitudinal nuclear magnetisation, M_y, is the magnetisation that evolves along the axis ($\underline{j}'$ in this case) of the polarising field, B_0.

- The differential (phenomenological) equation describing the time course of the longitudinal nuclear magnetisation, $M_y(t)$, is:

$$\frac{dM_y(t)}{dt} = -\frac{M_y(t) - M_0}{T_1}, \quad\quad\quad \text{Eq [II.8]}$$

with M_0 the magnitude of the polarised magnetisation before being altered by the excitation pulse B_1, which is a RF pulse that flips the nuclear magnetisation - initially parallel to the main magnetic B_0 field - by a certain flip angle, α (=

90° in this case), away from the y axis, producing a component of the magnetisation in the x-z plane.

This linear differential equation has the following general solution:

$$M_y(t) = M_0\left(1 - e^{-t/T_1}\right) + M_y(t_0)e^{-t/T_1}.$$
<div align="right">Eq [II.9]</div>

When T_1 relaxation occurs, the excited spins return to their initial position, along the B_0 field, by transferring energy into the surroundings (the lattice, and for this reason it is also called spin-lattice relaxation time).

Furthermore, the transverse relaxation is associated to spin transverse phase scrambling (see explanation in section II.1.3.1) and is measured by signal loss. In fact, the transverse relaxation is the loss of transverse nuclear magnetisation due to a loss of phase of the spins. It is a process different to longitudinal relaxation in that there is a mutual energy exchange between the spins (for this reason it is also called spin-spin relaxation time). The transverse nuclear magnetisation, M_{xz}, is the component of the nuclear magnetisation that evolves along any axis (x or z in this case) perpendicular to the polarising field.

- The differential (phenomenological) equation describing the time course of the transverse nuclear magnetisation, $M_{xz}(t)$, is:

$$\frac{dM_{xz}(t)}{dt} = -\frac{M_{xz}(t)}{T_2}.$$
<div align="right">Eq [II.10]</div>

This linear differential equation has the following general solution:

$$M_{xz}(t) = M_{xz}(0)e^{-t/T_2}.$$
<div align="right">Eq [II.11]</div>

II.1.2. Longitudinal T_1 relaxation

II.1.2.1. Basic description

The NMR longitudinal relaxation time, T_1, characterises the time it takes for the nuclear magnetisation to come back to its initial polarised state after being out of its equilibrium state. When relaxing, the energy from the spin is dissipated in the surrounding lattice until the spin system has come back to its equilibrium state. The parameter T_1 is an intrinsic characteristic time of materials or tissues.

II.1.2.2. Methods of measurements

Before running an experiment, the T_1 value of the sample under investigation needs to be known so that a suitable Repetition Time (T_R) value can be set, consequently allowing the best Signal to Noise Ratio (SNR) to be collected. It is possible to measure the T_1 constant in at least two different ways with the *profile* NMR Mouse®.

The first method consists of measuring the value of T_R that produces the highest SNR. T_R is the time duration during which the instrument is left "idle", so that the magnetisation can relax.

To find T_1, the SNR of the NMR signal is measured for various values of T_R, and the data is fitted to the following expression, see appendix C:

$$SNR \propto \sqrt{\frac{T}{T_R}} M_0 \left(1 - \exp\left(-\frac{T_R}{T_1} \right) \right), \qquad \text{Eq [II.12]}$$

where T is the experimental time for one particular measurement of SNR, and M_0 is the magnitude of the fully polarised nuclear magnetisation, as already defined before. Note that SNR is proportional to $\sqrt{T}$, therefore if twice more SNR is required, the experiment should be averaged for 4 times longer. Consequently, by choosing a T_R

value smaller than the one where the SNR is the maximum, one can achieve better overall SNR as the number of averages can increase.

Eq [II.12] is shown in Fig.II.1 and from this graph the location where its first derivative relative to T_R equals zero can be found graphically.
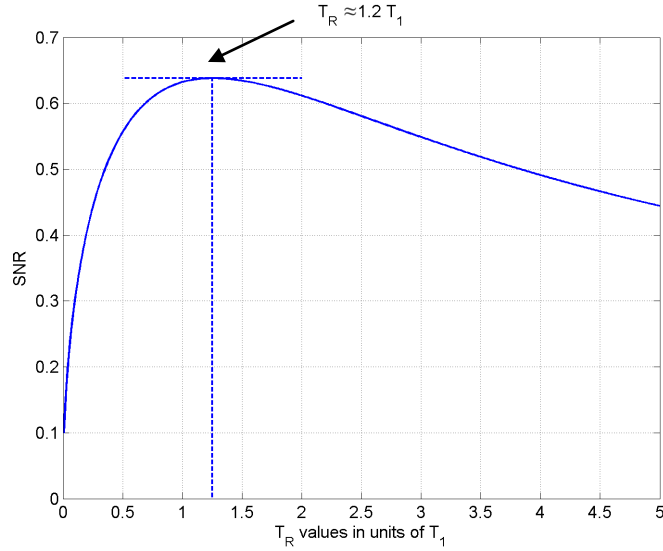
Fig.II.1: Plot of the SNR in Eq [II.12] as a function of T_R, clearly exhibiting a maximum when $T_R \approx 1.2 \ T_1$.

The SNR is rapidly lost if T_R is set to a value slightly lower than $1.2 \ T_1$, whilst the loss in SNR is much less severe if T_R is made slightly longer than $1.2 \ T_1$.

The second method, which is faster and more accurate for T_1 values smaller than 100 ms, is done using the saturation recovery sequence [68], as discussed in the next paragraph.

II.1.2.3. Saturation recovery sequence

Basically, the longitudinal magnetisation with increasing T_R values is measured and fitted to an exponential recovery given by the expression:

$$M_y(T_R) = M_0\left(1 - \exp\left(-\frac{T_R}{T_1}\right)\right).$$
                                                                    Eq [II.13]

45

This equation is derived from Eq [II.8] and details can be found in appendix D.

This magnetisation is measured by summing the amplitude of a fixed number of spin echoes for a given T_R value. When the asymptotic plateau of the curve is reached for the highest T_R values, the value of T_1 can be extracted. In order to obtain a good fit, the maximum T_R value should be set to be at least five times the T_1 constant, which corresponds to the time at which M_y has reached 99.3% of M_0.

II.1.2.4. T_1 measurement on several liquids

The longitudinal relaxation time, T_1, of the oil (DUCKHAMS 15W/40 Mineral formula) that was used for this work, was found to be (31.3 ± 0.3) ms. The DSTL also provided seven different liquid samples of which their T_1 value was measured, see Table II.1.

Sample number	Sample description	T_1 in ms
1	50% poly(ethylene glycol) Mw = 35,000, 49% H_2O, 1% Forafac 1033D (fluorinated surfactant, made by DuPont)	194 ± 2
2	50% poly(ethylene glycol) Mw = 35,000, 30% H_2O, 20% MeOH	317 ± 3
3	20% poly(ethylene glycol) Mw = 35,000, 80% H_2O	636 ± 5
4	20% poly(ethylene glycol) Mw = 35,000, 40% H_2O, 40 MeOH	661 ± 5
5	20% poly(ethylene glycol) Mw = 35,000, 79% H_2O, 1% Forafac 1033D (fluorinated surfactant, made by DuPont)	512 ± 4
6	98.5% H2O, 1.5% A380 (Aquasorb A380, powdered superabsorbent based on sodium carboxymethylcellulose)	1665 ± 12
7	10% poly(ethylene glycol) Mw = 200, 90% H_2O	1810 ± 13

Table II.1: T_1 values for the seven different samples provided by the DSTL, measured at room temperature and at 0.25 T.

In this work Duckams oil (= a hydrocarbon oil) was used as the penetrating liquid because it allows the fastest collection of large SNR by using the shortest repetition

time. However (in future work) from these seven samples, 1 and 2 could be used as their T_R values are short, respectively 233 and 380 ms.

The source of hydrogen-containing molecules is commonly referred to as "the challenge". In this thesis, one of the liquid challenges used is Duckhams oil that represents a simulant for a toxic liquid. Its ability to penetrate the textile structure depends on the external pressure applied to the drop.

II.1.3. Transverse T_2 relaxation

II.1.3.1. Basic description

The NMR transverse relaxation time, T_2, also called spin-spin relaxation time, is the time constant with which the transverse nuclear magnetisation decays exponentially, and results from the interaction of a spin with the spin of an identical neighbour nucleus. These interactions cause the spins to dephase randomly resulting in phase scrambling causing a reduction in the overall transverse magnetisation which is an irreversible process.

II.1.3.2. Methods of measurements

A train of spin echoes [69] can be collected from the CPMG sequence [70, 71] (explained later in section II.2.4.). This sequence was invented by four scientists: Carr, Purcell, Meiboom, and Gill. The spins are refocused between each echo and the signal is damped exponentially according to:

$$M_{xz}(t) = M_{xz}(0)e^{-t/T_2^{eff}} , \qquad \text{Eq [II.14]}$$

with $M_{xz}(t)$ the time course of the transverse nuclear magnetisation and $M_{xz}(0)$ its magnitude after the 90º excitation pulse. T_2^{eff} is the T_2 "effective" explained in section II.1.4.

On Fig.II.2 below, the exponential decay during application of the CPMG sequence is presented. After each refocusing pulse (also called 180° pulse or π pulse), the signal collected is lower. An exponential fit is done to the experimental data from which two parameters are extracted:

- The NMR amplitude.
- The T_2^{eff} value, its reciprocal being the effective transverse relaxation rate (R_2^{eff}).
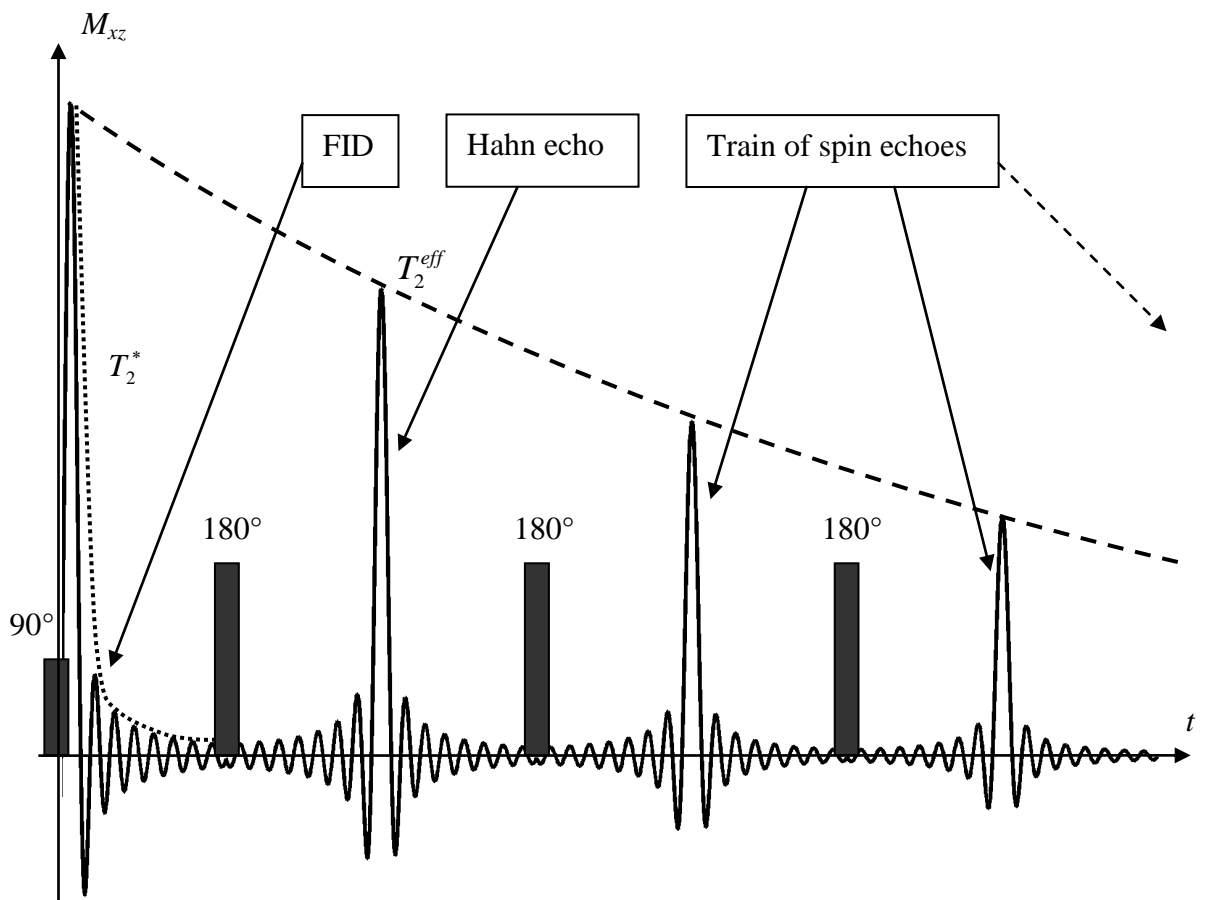
Fig.II.2: Standard CPMG sequence in grossly inhomogeneous field producing a train of spin echoes. The initial 90º pulse generates the transverse nuclear magnetisation. This magnetisation is then periodically refocused by a long string of closely spaced 180º pulses. By applying a refocusing pulse a spin echo is eligible to be formed due to a partial amount of spins being rephased. The exponential decrease of the signal is due to the spin-spin interaction and to self diffusion process for fluids if a field gradient is present in the system. The meaning of T_2 "star" (T_2^*) will be given in the next sub-paragraph.

II.1.4. T_2 change with pore filling

T_2 is the relaxation time due to spin-spin interaction measured in the presence of a homogeneous B_0 field (in the absence of a field gradient). What is more, in the case of the instrument used in this work, T_2^{eff} is measured (see Fig.II.2) because the spins diffuse in a field gradient (which is intrinsic to the inhomogeneous polarising field) and they are therefore imperfectly rephased with 180º RF pulses, which makes the relaxation time shorter than T_2. Also, in the presence of a field gradient, the relaxation decay is enhanced and T_2^* is measured by the FID decay rate following a 90° pulse (see Fig.II.2).

In the 1970's (when the *profile* NMR Mouse® did not exist), a high resolution 60 MHz Varian spectrometer was used to run a study [33, 34] similar to this one on activated carbon. With this NMR spectrometer, the NMR frequency shift of an atom due to its specific location within a molecular species (commonly referred to as the "chemical shift") was measured. With the NMR Mouse®, the different frequencies that are sensed are dominated by the strong vertical field gradient which provides the spatial encoding of the signal. On-resonance, the signal is the highest (see Fig.II.3 at centre of the Gaussian); off-resonance, the signal decreases due to imperfect refocusing pulses.
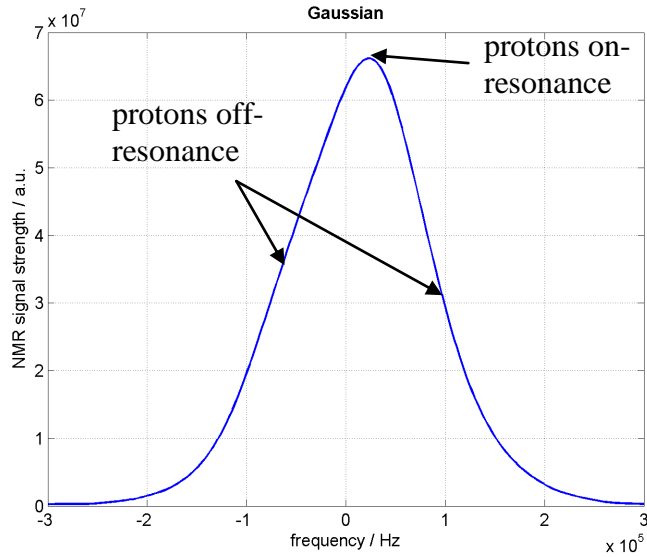
Fig.II.3: Typical frequency response showing the protons off and on-resonance on the profile NMR Mouse® used in this study. The curve is obtained by Fourier transforming a spin echo, and strongly resembles a gaussian function, see Fig.II.7. The shape of this curve is related to that of the RF pulse used. Its width is related to the time duration of the RF pulses and the strength of the field gradient.

A porous material is composed of pores onto whose surface a chemical can be adsorbed. In 1970, the work from the French group presented in chapter I (Conard *et al.*) showed that there is a change in both the NMR chemical shift and the line width during adsorption [33, 34], see Fig.I.3 and Fig.I.5. This has to be put in light of the fact that the transverse relaxation rate, R_2, is directly related to the Full Width at Half Maximum (FWHM) of the corresponding spectral peak, and therefore to the line width through the following relationship:

$$FWHM = \frac{2\sqrt{3}}{T_2} = 2\sqrt{3}R_2.$$
Eq [II.15]

This equation is derived in appendix E.

Conard *et al.*, explain that during adsorption, the line width becomes smaller because of the increased rotational and translational motions of the adsorbed molecules.

On one hand, in the scenario when the pore is free of any molecules, there is no NMR signal. On the other hand, the mobility of protons in pores needs to be considered

50

through two cases. When the pore is saturated, mostly bulk liquid is then sampled resulting in a long T_2 which means a low R_2. The second case is when only a few hydrogen-carrying molecules are adsorbed onto the pore which results in a high R_2 or short T_2 being monitored. This corresponds to Conard's statement (seen above) about molecular motion, in which molecules that are adsorbed (for low value of θ) are those that are most strongly "attached" to the pore and therefore have the lowest mobility resulting in the highest R_2 value. A range of different pore filling states, from the case where only a few adsorbed hydrogens are present to the case where full saturation is achieved, can therefore be probed with T_2.

The gradual change of R_2 observed during adsorption followed by desorption can be justified as follows. Note that before any adsorption has occurred, the pores are filled with air and only thermal noise is measured by the NMR hardware. As soon as a few hydrogen-containing molecules have adsorbed onto the pores, the measured R_2 is relatively high due to strong interactions between the carbon walls and the molecules. As the adsorption process takes place, the R_2 decreases continuously as a result of a pore filling effect in which the molecules stack on layers increasingly remote from the carbon walls resulting in weaker interactions with the carbon walls. At the maximum saturation level of the AC, the R_2 is at its lowest value, and this is attributable to the largest presence of liquid state in the pores. When the challenge has vanished or is taken away, the opposite process comes about. Desorption is likely to occur because the molecules in the centre of the pores are most weakly bound with the walls.

Note that vapour uptake occurs for a pore size distribution ranging between values from less than 2 nm (for micropores) to more than 50 nm (for macropores), most probably until a value of 100 nm above which voids do not fill effectively any more by adsorption processes. In addition, liquid ingress occurs in pores for values spanned between 1 and 10 μm.

II.1.5. Distinguishing smaller and bigger pores

In this discussion fluid ingress into pores is considered without any adsorption. This means that the liquid is not strongly interacting with the walls as is the case for example

of a fluid saturating a porous stone such as a sandstone. The pore size can alter the resulting NMR signal of a fluid saturating them through two regimes [72].

On one hand, a fluid molecule can diffuse through random motions and might hit the solid surface where it then can possibly relax, a process also known as "wall-enhanced relaxation" [72]. On the other hand, a liquid residing in a porous medium experiences NMR relaxation due to interactions occurring at the liquid/solid interface. Kleinberg [72] has described those two scenarios as fast diffusion and slow diffusion respectively, as explained below:

- the molecules may be diffusing inside the pore thereby causing the nuclear magnetisation to be uniform. The decay in the pore, in this regime, is monoexponential and only depends on the surface-to-volume ratio of the pore and is independent of pore shape. This is called: "*surface-limited* regime" [73] *(fast diffusion)*.

- the pores may be relatively large and/or surface relaxation may be strong. In this regime magnetic relaxation occurs at the pore surface, but the decay of the macroscopic magnetisation is controlled by the transport of molecules to the surface. Therefore the magnetisation decay in each pore is not uniform and has a multiexponential decay which depends on the shape of the pore. This is called: "*diffusion-limited* regime" [74] *(slow diffusion)*.

The pore size can be estimated in the fast diffusion regime by measuring the longitudinal relaxation rate (R_1) or the transverse relaxation rate (R_2) through the following equations [73]:

$$R_1 = \frac{1}{T_1} = \rho_1\left(\frac{S}{V}\right), \qquad \text{Eq [II.16]}$$

$$R_2 = \frac{1}{T_2} = \rho_2\left(\frac{S}{V}\right), \qquad \text{Eq [II.17]}$$

where S/V is the surface to volume ratio of the pore, ρ_1 and ρ_2 are the surface relaxation strengths (expressed in $m.s^{-1}$).

II.2. Characteristics of the *profile* NMR Mouse®

The *profile* NMR Mouse® is a unilateral spectrometer that has the ability to measure the NMR signal coming from a sample positioned next to one side of, or most often above, the instrument. This device is "mobile" in that it can easily be moved by hand, as it only weights 5.2 kg. The acronym Mouse stands for MObile Universal Surface Explorer. By placing a sample across the sensitive slice, this unilateral NMR scanner produces one-dimensional profiles of the sample structure with a spatial resolution reaching 15 µm.

The NMR Mouse®, extensively used throughout this work, is composed of the polarising magnets assembly and the RF coil, and has the shape of a parallelepiped rectangle (L × W × H = 13 × 10.8 × 9.7) cm^3, see Fig.II.4.

Fig.II.4: Photograph of the *profile* NMR Mouse® connected to the RF transceiver (not shown), easily transportable due to its light weight (5.2 kg) and moderate size. A PC mouse on the left is also shown to give an idea of the actual size of the NMR Mouse®.

II.2.1. B_0 field: static polarising field

The polarising field is made from an assembly of four permanent magnets. These magnets are arranged in space [75] so that they generate a remarkably flat sensitive volume with adjustable height (up to 10 mm away from the instrument) approximately 0.2 mm thick (which is adjustable, see explanation later on in section II.2.2.) and 1.5 cm in diameter in the transverse surface area. This built-in B_0 field has a strength of 0.25 Tesla (T) at the sensitive volume, resulting in a resonant frequency for protons of 10.64 MHz.
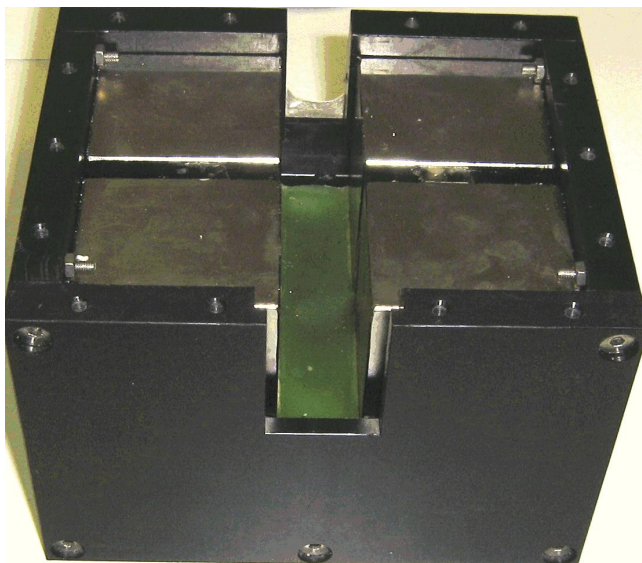
Fig.II.5: Photograph showing the inside of the NMR Mouse®. Four block magnets potted in epoxy resin are clearly seen.

II.2.1.1. Intrinsic field gradient generated by the permanent magnets

In order to describe the various magnetic fields involved when using the NMR Mouse®, the three cartesian axes are defined as shown in Fig.II.6.
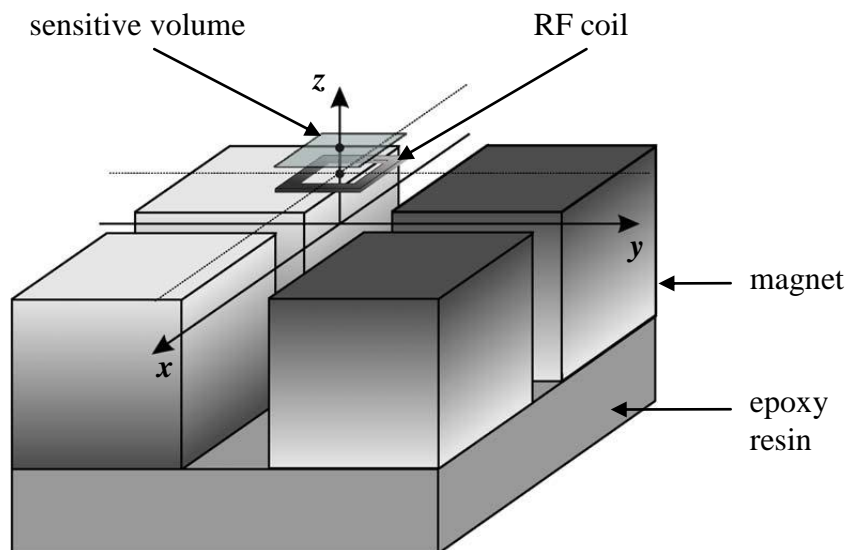
Fig.II.6: Schematic representation of the inside of the NMR Mouse®, (reproduced from Ref [75]). The gradient in the grey shading suggests the polarity of a specific magnet. The sensitive volume is parallel to the *x-y* plane and lays above the NMR instrument.

Those axes give the three orientations in the laboratory frame. The B_0 field is along the *y* axis in the *x-y* plane where it exhibits homogeneous properties at a single *z* location. However, the B_0 varies along the *z* direction. This heterogeneity results in a strong intrinsic vertical field gradient.

By convention, the *z* axis is shown upwards. Note that for the choice of axes in this case, B_0 is along the *y* axis unlike most textbooks where it is usually described as being along the *z* axis.

II.2.1.2. Field gradient measurement

It is possible to measure the linearity and the strength of the field gradient by using a thin enough sample. In this work a film of oil of 12 μm was used. The layer of oil was sandwiched between two microscope slides spaced apart with a 12 μm thick strip of mylar running all around the slide. The *z* coordinate of this thin sample was incrementally changed by interleaving a gradually increasing stack of 80 μm thick tracing paper sheets, the total thickness of which was measured for each trial. The NMR data was collected using a CPMG sequence with 40 spin echoes (echo time, $T_E = 510$ μs, repetition time, $T_R = 170$ ms, number of accumulated experiments = 1500).

These spin echoes (see section II.2.4.) were individually Fourier transformed (see appendix F and Fig.II.7 below) and then averaged.
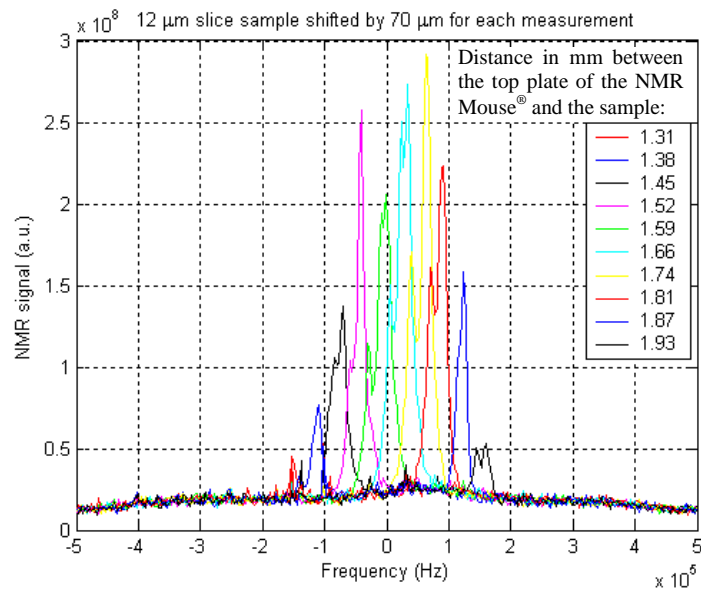
Fig.II.7: The thin oil slice yielded NMR signal at different frequencies across the sensitive volume as the height of the slice was incremented. The overall response shape is an approximately a Gaussian profile.

The peak frequency was plotted against the total thickness of the paper stack, as shown in Fig.II.8.
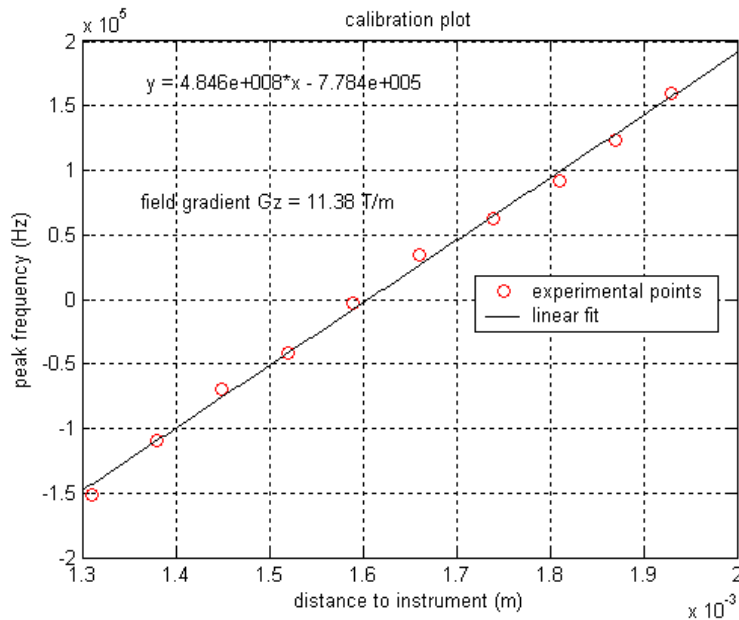
Fig.II.8: plot of the frequency of peak versus the total thickness of the paper stack. From the fitted curve, the slope gradient $d\nu/dz$ was calculated and was found to be $4.846 \cdot 10^8$ Hz.m^{-1}. Accurate calibration of the field gradient strength and linearity is obtained using a 12 μm thin oil slice.

From the Larmor frequency equation, the field gradient can be calculated:

$$G_z = \frac{d\nu}{dz} \cdot \frac{2\pi}{\gamma},$$

Eq [II.18]

thus giving $G_z = 11.38$ T.m^{-1}.

The overall response shape results in an approximately Gaussian profile, with a FWHM of 172 kHz (obtained from Fig.II.7) which corresponds to 355 μm with a field gradient of 11.38 T.m^{-1}. Excellent linearity between the peak frequency and the distance to instrument is found.

This strong z field gradient resulting from grossly inhomogeneous magnetic fields comes with good x- and y- homogeneity (of the y component of the B_0 field) within the sensitive volume and allows high (*ca.* 5 μm) spatial resolution. Not only can a profile, showing the spin density distribution, be produced but different NMR parameters like relaxation times (T_1 and/or T_2) and the local diffusion coefficient can also be spatially resolved in a non-destructive and non-invasive manner. In this work 1D profiles with a high spatial resolution of about 15 μm are obtained after only 4 minutes of averaging.

For comparison purposes, the typical field gradient strength, G_Z, of a whole body scanner may be calculated for a Field of View (FOV) of 20 cm, as would be the case for example when imaging the human brain. This particular FOV can be achieved within a pulsed field gradient of say 1 ms. If the image has 512 points, the sampling rate of the NMR signal will be ($512/1 \times 10^{-3}$) Hz. This, in turn, corresponds to the FOV of 20 cm, or, in other words, the frequency range of the spectrum, which is ($\gamma \times FOV \times G_Z / 2 \times \pi$). By rearranging, it is found that:

$G_Z = 2 \times \pi \times 512 / (\gamma \times FOV \times 10^{-3})$, which is 60 mT.m^{-1}, *i.e.* a field gradient strength approximately 200 times weaker than that residing within the *profile* NMR instrument's selected slice.

II.2.2. B_1 field: RF field

In addition to B_0, a Radio Frequency (RF) field needs to be applied to the sample under investigation, in particular in order to tilt the nuclear magnetisation away from the B_0 field. In NMR, this field is commonly referred to as the B_1 field and it is a homogeneous electromagnetic RF wave generated by a RF coil. The B_1 field has to be normal to the B_0 field; it excites the nuclear magnetisation which subsequently precesses at the Larmor frequency in the sensitive volume. If it is "on resonance" the nuclear magnetisation precesses about B_1 at precession frequency of v_1 following:

$$\omega_1 = \gamma B_1 = 2\pi v_1, \qquad\qquad \text{Eq [II.19]}$$

with ω_1 being the angular frequency of the precession of the nuclear magnetisation about B_1.

In order to tilt the nuclear magnetisation away from the polarising field, the B_1 magnetic field is made to rotate about the B_0 axis with the same frequency as the precessional motion of M about B_0. This results in $M(t)$ being maintained at right angles with the direction of B_1, resulting in a continuous tilting of the magnetisation $M(t)$ with respect to the axis of B_0, whilst it is still precessing about it.

By changing the height (referred to as the z coordinate) of the RF coil horizontal plate relative to the magnet assembly, the height of the selected slice relative to the instrument can be changed from 10 mm to any smaller value. A remote slice allows the non-invasive exploration of thick objects, but the further the selected slice is from the instrument, the thinner it is, because the RF pulses need to be made longer, resulting in a narrower bandwidth. Rapid drop of B_1 field strength also causes a rapid drop of the SNR with increasing distance. Consider w being the distance between the centre of the RF coil and the sensitive volume, B_1 [76] drops with w^{-3}. The B_1 pulses need to be no longer than 10 µs in order to reach 90° flip angle.

II.2.3. Additional gradient coils improving the imaging potential of the NMR Mouse[®]

The *profile* NMR Mouse[®] can be upgraded by adding gradient coils so that it becomes a "close cousin" of an MRI scanner [77]. The technique consisting of acquiring a profile into the z direction, described later on in section II.2.5., remains the same. Two additional switched field gradients are added into the x-y plane breaking the horizontal homogeneity of the y component of the polarising field. In order to obtain a two dimensional MRI image in the x-y plane, a series of CPMG sequences (Table II.2) is applied with M numbers of CPMGs with increasing dephasing applied along the x axis and N numbers of CPMGs with increasing dephasing applied along the y axis. One experiment will last $N \times M \times (\tau + T_R)$, where τ is the time duration of the CPMG sequence and T_R the repetition time.
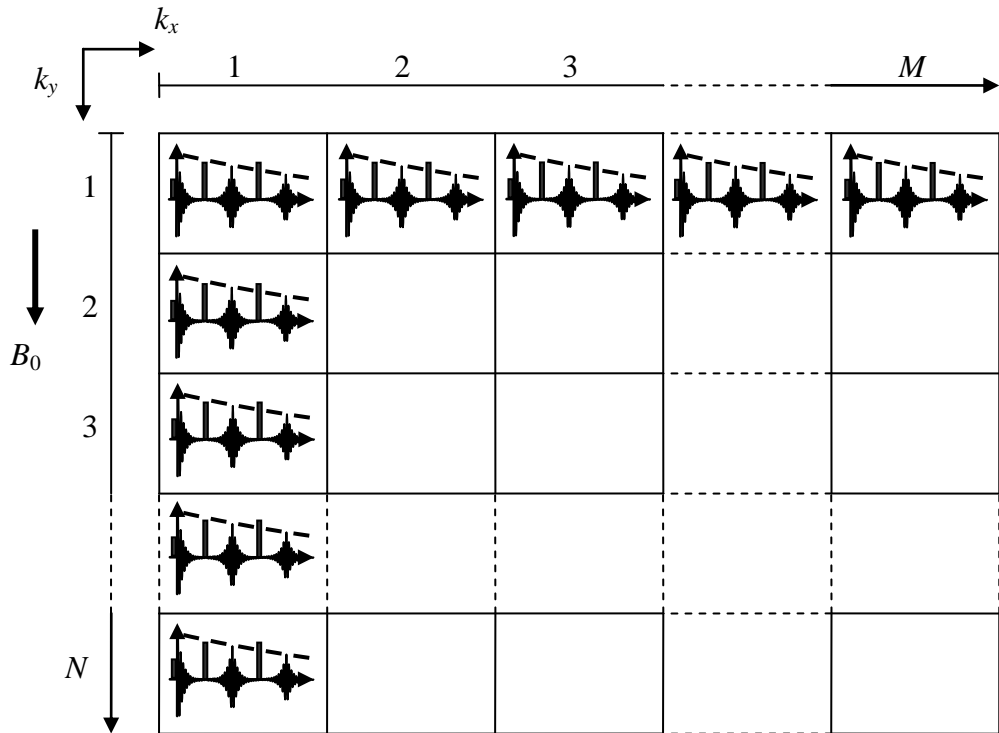
Table II.2: A series of CPMG sequences is used with the switched gradients in order to obtain a two dimensional MRI image. The column and row characterized by dashed lines correspond to several applied CPMGs which are not shown. k_x represents the amount of phase scrambling applied along the x axis and k_y represents the amount of phase scrambling applied along the y axis.

This technique is time consuming (30 minutes to one hour for one image) and tends to yield poor SNR due to how thin the selected slice is, but it makes the instrument's capacity close to that of an MRI scanner.

II.2.4. CPMG sequence exhibiting a long train of refocused spin echoes

The presence of the strong magnetic field gradient that resides across the selected slice can be most successfully [78] exploited in conjunction with the CPMG sequence to collect spin echoes. In fact, due to the strength of the field gradient, by using a single 90° excitation pulse, no FID can be collected with this instrument because T_2^* is very short (typically of the order of 2 μs). However, the CPMG sequence produces a Hahn echo after the initial 90° pulse and the first refocusing pulse, followed by a train of echoes generated by their respective refocusing pulses, see Fig.II.2. The nuclear spins are first precessing in unison which results in a large signal in the receiver coil (RX). Due to a combination of molecular diffusion within the heterogeneities of the field (or field inhomogeneities) and transverse relaxation and coherent phase warping, the spins quickly dephase resulting in a rapid loss of signal. The coherent phase warping is reversible by applying a π pulse to the spins which reverse their direction of precession and thus makes them come back in phase, thereby producing a spin-echo.

II.2.5. The NMR instrument: a powerful tool to resolve 1-dimensional profiles

A single spin echo comprises spatially encoded information across the selected slice. By processing the train of spin echoes, an exponential can be fitted to the amplitude of each echo in order to extract one dimensional profiles of the NMR amplitude and of R_2 of a volume across the slice. The fitted NMR amplitude represents the absolute amount of liquid found at a given z position whereas R_2 provides a range of information including for example the fabric pore size distribution [72] of a liquid sitting in it. The relaxation rate, R_2, can also provide information about adsorption levels in pores in the case of AC for instance.

II.2.6. Causes for profile drift due to hardware imperfections

II.2.6.1. Temperature drift effect

The top plate from the profile NMR Mouse® is made of 2 mm thick Printed Circuit Board (PCB) and might demonstrate sagging when a weight is placed on it. Moreover, under increasing pressure, the fabrics (the texture of which will be described in chapter IV) might experience an irreversible reduction in total thickness. These two effects can cause a shift in the spatially resolved information that the instrument provides. Another cause of such shift, the one due to temperature, was somewhat explored. Indeed, the strength of the permanent magnets (made of highly magnetised iron neodymium boron, FeNdB [79]) assembly changes slightly with ambient temperature variations. The thermal coefficient of a FeNdB magnet is typically $-0.12\%/°C$ which means that if the temperature increases by 100°C, its magnetisation (due to B_0) will decrease by 12%. A simple investigation of the effects of variations of temperature was undertaken. A static sample made of 12 µm of a thin oil slice (see section II.2.1.2.) was laid in the middle of the sensitive volume and a repeated NMR measurement was run continuously over 3 days, with one measurement lasting 20 minutes. The position of the peak of the Fourier-transformed NMR signal was plotted against the time (Fig.II.9).
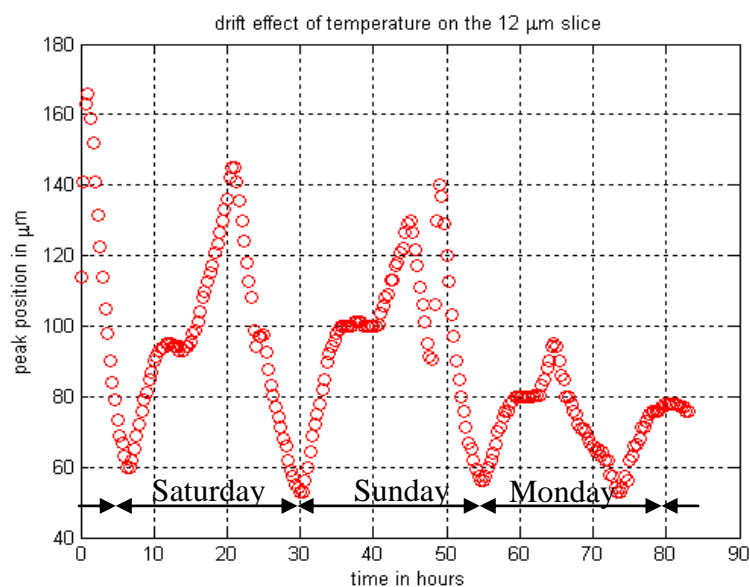
Fig.II.9: variation of the NMR-measured height of the thin sample (due to variations of the temperature in the room), as a function of the time at which the measurement was taken.

Apparent changes of up to 110 µm were observed in the position of the profile of the static sample placed on the instrument. These changes were periodic and synchronized with the on and off switching of the air conditioning system in the laboratory. Throughout the day (8 am-6 pm), the temperature was set to 21 °C. During night time, the temperature can decrease to 18 °C thus producing a substantial temperature variation of 3 °C. In another experiment, very similar to the one described above, the temperature was monitored with a thermocouple (of K type) placed directly on one of the four magnets of the instrument. The rise in temperature was measured and the NMR profile drift was estimated to be (30 ± 4) µm/°C.

II.2.6.2. Conclusion on the static reference for drift compensation

In order to compensate for the shifts in information previously discussed, the following procedure was implemented:

For two types of experiments (which will be fully explored in chapter IV), a layered fabric is separated from a 4 mm thick rubber with a 166 µm microscope slide, see Fig.II.8 in chapter IV. This rubber which is placed on the top of the sensitive volume provides a static reference for the z position of the system under investigation. This allows the z position to be accurately determined despite slight variations in the strength of the permanent magnet assembly caused by slight changes in ambient temperature and despite a load placed on top of the system under investigation. The thickness of the glass (166 µm) between the rubber and the top of the sample is well above the spatial resolution of the instrument (15 µm) so that the signal from either the rubber or the sample can therefore be separated unambiguously during post-experiment signal processing, see Fig.II.10.
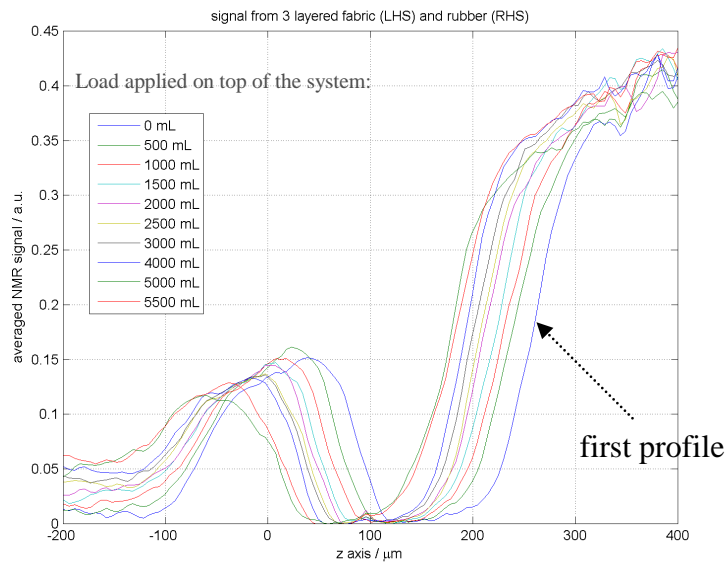
Fig.II.10: The rubber fronts exhibit substantial displacements between experiments involving different vertical loads and slight variations in temperature.

All the profiles can be realigned by using the same reference (the rubber front) in order to be able to calculate the R_2 value and the fitted amplitudes at a specific location inside the fabric during post processing of the collected NMR data.

A MatLab® (The MathWorks Inc., MA, USA) code was developed in-house to first shift the raw NMR profiles along the z axis, by multiplying the complex spin echoes by a complex exponential with a linear phase gradient, see "shift theorem" in appendix G, until the rubber fronts were all matched to that of the first profile, see Fig.II.11. This rubber fronts accounts and corrects for any z position drifts, including those due to temperature, and significant load placed on top of the fabric.
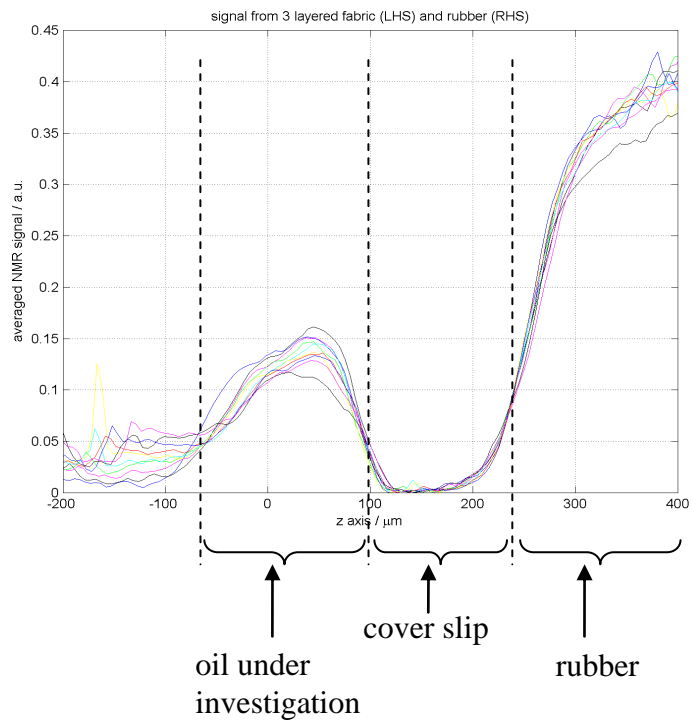
Fig.II.11: Same data than that shown in Fig.II.10 but the drifts have been compensated for.

CHAPTER III: THE ELECTRICAL PROPERTIES OF ACTIVATED CARBON: A HURDLE FOR COLLECTING NMR SIGNAL

INTRODUCTION

In this chapter three different types of activated carbon are investigated: AC monolith, AC composite and AC cloth. The physical structure of all of these carbon materials will be presented in greater detail in chapter V. Here the interest is focused on the fact that AC is a conductive material and that in NMR/MRI experiments, the scanned samples should not be conductive (which disturbs the waves emitted from the Radio Frequency (RF) coil) or metallic (mostly ferromagnetic, which absorbs the polarising field).

It is said in the literature [80] that if one considers carbon, the conductivity at room temperature increases for an increase in compression. Increasing this compression will consequently increase the packing of the material, eventually causing collapse of pores, decrease in air gap between the carbon particles and result in easier movement of electrons from one particle to another.

AC can be manufactured from several raw materials which will also influence the electrical conductivity. As an example, if one considers AC composite from rice husk [80], the carbon matrix in the composite forms an interconnected network with silica, in an irregular fashion so that it can have a major influence on the electrical property of the material. Silica, which is one of the components of the raw material, cannot evaporate during adsorption, and therefore remains intact in the matrix, effecting the porous structure and the electrical conductivity. Silica being an inert material, if removed from the network would result in still higher values of electrical conductivity. The typical electrical conductivity value of silica (which is a good insulator) is approximately 10^{-14} S.cm^{-1}. As the conductivity value obtained for the carbon composites is around 10^{10} times higher, the electrical conductivity in this composite is fully assumed to be due to the carbon matrix and depends on the compression rate it suffered. The conductivity from bulk carbon typically increases from 3.28×10^{-4} to

2.02×10^{-3} S.cm^{-1} for rise in compression pressure from 75.9 to 578.2 kPa [80].

For AC cloth, Ramos correlated the electrical resistivity with elemental carbon content and total pore volume [81]. By comparison, AC cloths made from different cellulose precursors, the maximum electrical conductivity was developed for the ones containing minimum porosity (thus maximum carbon content). Moreover, depending on how AC cloth is activated, its resistivity will also vary. Activation with CO_2 results in a higher conductivity of the AC fabrics, compared to steam activation [82]. AC monoliths are usually very dense carbon materials. Ruiz states that thanks to its low electrical resistivity, some types of AC monoliths show excellent performance as electrodes in high-power supercapacitors [83].

The three types of ACs (composite, cloth and monolith) studied in this thesis are good conductors. In order to collect NMR signal with good SNR, test experiments were designed to quantify the effect of the samples' relatively high electrical conductivity.

The *profile* NMR Mouse® is designed to interrogate proton NMR. A fresh AC is hydrogen free and therefore does not produce any ^{1}H NMR signal. If enough hydrogen-carrying molecules (such as a Volatile Organic Compound (VOC), water,…) reach the network of the AC and are trapped inside, then these molecules yield a signal which is potentially detectable with NMR/MRI.

III.1. Preliminary results assessing the electrical conductivity of an activated carbon

The electrical resistance of the three types of AC was measured between two points 1.27 cm (half of an inch) apart. For the composite and the monolith, the measurements were taken over a diameter of a cross section of the cylindrical plug of carbon network whereas for the cloth the measurement was taken between two points belonging to its plane. The results were as follows, for the monolith: (14 ± 3) Ω, for the composite: (63 ± 5) Ω and for the cloth: (2450 ± 50) Ω. Thus the different ACs demonstrate relatively low resistivity which makes it challenging to collect NMR signal from them as shown in the following sections.

Another example demonstrating the possibility of imaging a highly conductive porous material is shown on Fig.III.1 which represents MR images of heptane saturating pores of an AC monolith (acknowledgement goes to Dr Martin Bencsik who ran the experiment on a Bruker Biospec 2.35 Tesla at the University of Nottingham). These images were made as a pilot study to see whether the B_1 field (RF field) can penetrate the AC monolith. The MRI data was collected with the "spin echo imaging" sequence, with the following settings:

- the echo time T_E was 7.737 ms,
- one experiment was acquired with 16 averages,
- the field of view was 3.257 cm with 128 by 128 pixels, and a spatial resolution of 254 μm,
- the slice thickness was 4 mm,
- the repetition time was 600 ms, resulting in a total imaging time of 20 minutes.

Note that, NMR signal was totally lost in the second echo (15 ms).
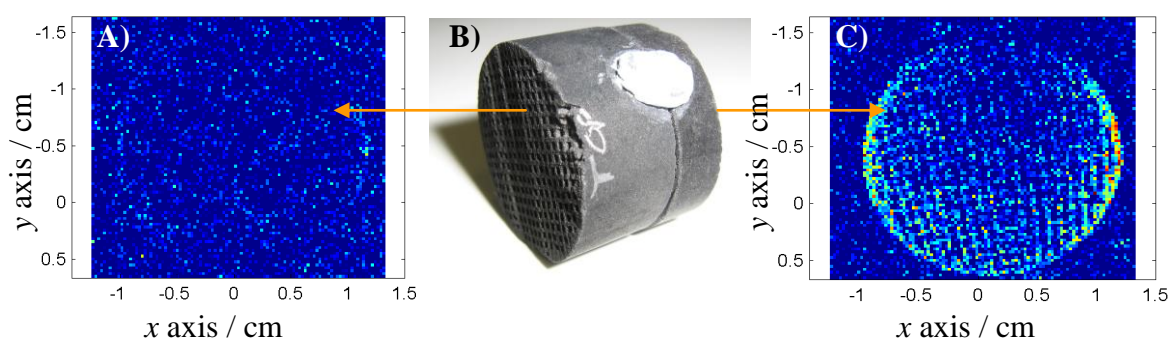
Fig.III.1: A and **C** are spin echo images obtained with a Bruker Biospec 100 MHz. The millimetric channels of the monolith were at 90° to B_0 and 90° to B_1. In **B** a photograph of the sample under investigation (consisting of two AC monoliths held together with blu-tack) is shown. The AC monolith on the left had not been exposed to heptane whereas the monolith on the right had adsorbed 1 mL of heptane for one hour, 10 days prior to running the MRI. Note that a total desorption of heptane only occurs if the sample is degassed by placing it in a vacuum oven (during 4/5 hours) at a high temperature (*ca.* 160 °C), see section V.1.3.

Even with the most conducting samples used, it was found that MRI is possible but rather difficult to achieve. Because of the good conductivity of the three AC samples, it is not easy to collect NMR signal from them with the NMR Mouse® as RF electromagnetic waves are attenuated at the surface of an electrical conductor, further explained in section III.2.5.

III.2. Experimental protocol

In the next paragraphs, one experiment aimed at finding out whether the signal strength is homogenous as the selected slice is moved inwards in an AC sample that had adsorbed heptane prior to the experiment is presented. Another experiment is presented that clarifies the extent to which the transverse size of the sample matters when proton NMR signal is being collected from it. A further experiment is presented in which is designed to explore whether the continuous or discontinuous outer rim of the AC monolith is affecting the NMR signal. Finally there is a brief discuss of measurements of RF heat deposited in the AC monolith.

III.2.1. Depth scanning in two types of activated carbon

To examine the extent to which the RF signal is absorbed in AC as a function of depth, three different samples were prepared. A cylindrical plug of monolith without its outer rim (0.5 cm long and 2.0 cm in diameter, see **C** on Fig.III.4), an intact monolith (0.5 cm long and 2.2 cm in diameter) and a cylindrical plug of composite AC (0.5 cm long and 2.4 cm in diameter) were each placed, once at a time, in an air tight receptacle in close proximity to a heptane source (see Fig.III.2) during 12 hours so that the pores were in a steady saturated state (in chapter V, it is seen that 3 hours is enough to saturate such a sample). Note that the outer rim of an AC monolith is made of a continuous ring of porous material with an i.d. of 2 cm and and an o.d. of 2.2 cm.
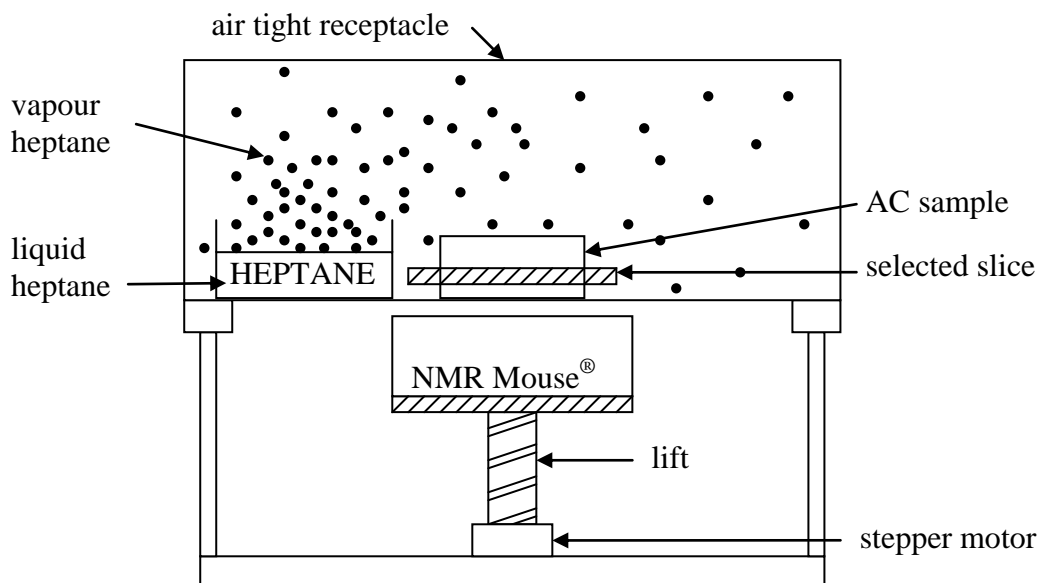
Fig.III.2: Sketch representing an air tight receptacle in which heptane vapour reaches the ACs (as described on drawing) by spontaneous evaporation in order to keep a steady state saturation level in the AC samples.

The receptacle was placed in the sensitive volume on top of the NMR Mouse®. The instrument was secured to a lift which was controlled with a stepper motor having a hysteresis of 15 µm if the directions up/down or down/up is changed. The ACs were scanned vertically with the lift going down so that at the beginning of the experiment the sensitive volume was 4 mm into the sample. The lift moved downwards in steps of 100 µm after each NMR measurement which lasted for 10 minutes. The settings were: $T_R = 400$ ms, $T_E = 100$ µs, acquisition time = 80 µs and 128 echoes were collected.

III.2.2. NMR signal from increasing disc size of activated carbon monolith and composite

Due to the electrical conductivity of the AC samples, when subjected to an RF wave (see further explanation is section III.2.5), current is created inside the carbon samples. The larger the size of the samples, the higher the possibility is for current to accumulate. This experiment was aimed at looking into the effect of increasing disc size of AC samples on the NMR signal.

A source of liquid heptane residing in the cap of a vial (of an outer diameter of 2.3 cm)

was placed in a closed receptacle similar to that used in the previous experiment. The liquid heptane acts as a permanent source of vapour thereby maintaining a steady state in the saturation level of the ACs. The pre-saturated AC composite and monolith samples were cut so as to reduce their diameter, and the corresponding NMR signal was collected for each sample obtained. Discs of rubber were also cut from a large sheet (0.8 mm thick), and the corresponding NMR was also collected. When cuts were produced on the discs, the shape was rendered rather irregular compared with the original perfect circle. Therefore the decreasing sizes of the three different discs areas were measured on a millimetric graph paper by drawing the contour of the disc and then measuring the area within the contour by counting the number of 1 mm^2 sized squares. This technique seems to be accurate enough, and error bars are added so as to reveal possible mismatches in counting. The NMR signal was collected by placing the thin disc samples into the sensitive volume of the NMR Mouse®. From the experiments, the NMR signal was then plotted as a function of the sample's transverse area. Each measurement lasted 8 minutes. The settings were: T_R = 400 ms, T_E = 80 μs, acquisition time = 40 μs and 128 echoes were collected.

III.2.3. Removing outer rim of activated carbon monolith

As described in section III.2.1, and seen on Fig.III.4.**C**, the rim of the monolith is made of a continuous and dense porous carbon material and exhibits the shape of a closed loop which might be exposed to create an electrical circuit when RF waves are deposited into it during an NMR measurement, see further explanation in section III.2.5. Therefore, in this experiment, the effect of this outer rim was examined. The experimental set up was very similar to that described in section II.2.1, and only differed by the technique of feeding the vapour of heptane to the AC. Prior to the experiment, the AC samples were reactivated by means of vacuum at 160 °C during five hours in order to remove as many molecules as possible. The same experimental preparation was used for all three monolith samples, each with different outer rims, all 6 mm tall. The three experiments were run separately and consisted of heptane uptake with a relatively slow rate of evaporation which was obtained by placing three microcentrifuge tubes containing 1.5 mL of heptane, see Fig.III.3. In each of these tubes, two holes of 1 mm in diameter were pierced on its side allowing the heptane

vapour to escape.
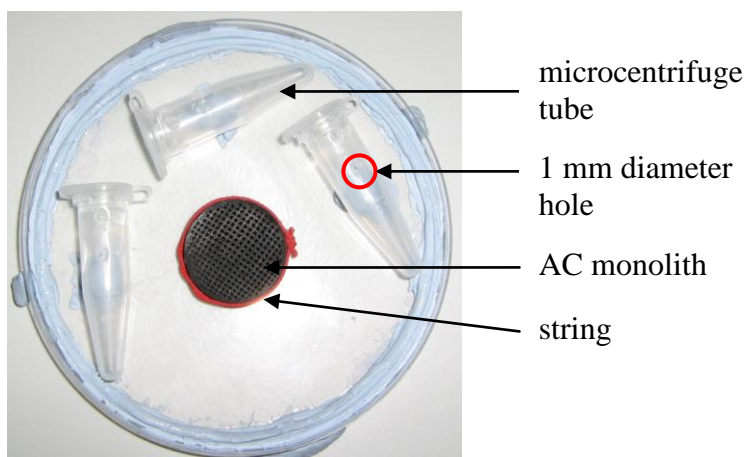
Fig.III.3: Photograph of a receptacle (a petri dish in this case) hosting the monolith and the heptane sources in three microcentrifuge tubes of 2 mL. The dish is made air tight by means of blu-tack holding the lid. The string around the monolith holds the sample together even if it splits into smaller pieces (as is often seen during slow adsorption).

For the three different adsorption experiments, the signal was averaged for 19 minutes and the following settings were used: $T_E = 130$ µs, 128 echoes, $T_R = 800$ ms, acquisition time = 80 µs.

Usually the monolith breaks apart when a slow uptake of heptane is occurring. In order to keep the monolith pieces together (Fig.III.4.**A**), a string was tightened around it. On another monolith sample several cuts were generated in the outer rim (Fig.III.4.**B**) therefore breaking the continuity of the current being created in it. Finally, on a last monolith, the rim had been cut-out altogether (Fig.III.4.**C**).
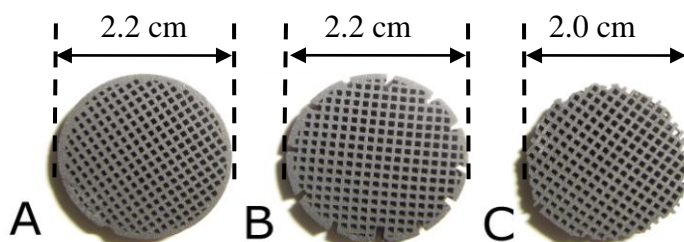
Fig.III.4: Different AC monolith samples. **A)** Intact monolith slice. **B)** Monolith slice with several vertical cuts in its outer rim. **C)** Monolith slice with outer ring removed.

III.2.4. NMR signal from discs of activated carbon cloth with increasing diameter

A shielding effect was encountered when two AC cloths (4 cm x 4cm) are stacked together. Unexpectedly, less NMR signal appears to come from the cloth in the closest proximity of the vapour source, see Fig.III.5. Concern grew after several attempts of monitoring the propagation of the vapour into two stacked AC cloths in which it was systematically observed that more signal occurred in the layer furthest from the vapour source (see also section V.4.2. for experimental set up details). Clearly, the vapour reaches first the top cloth which should thus provide more NMR signal.
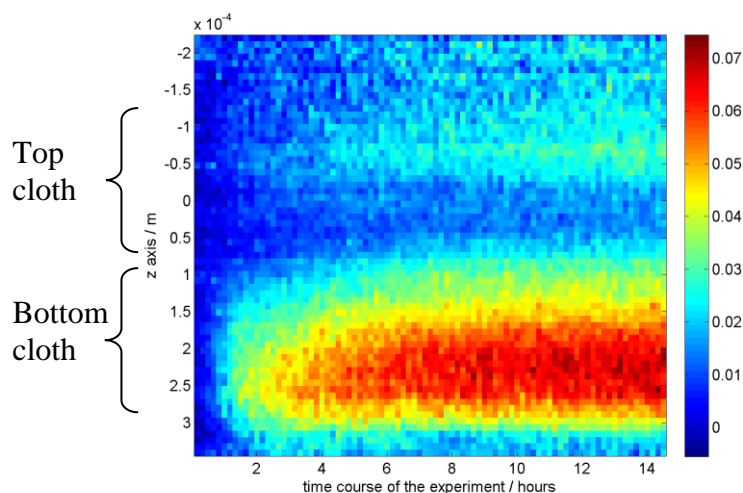
Fig.III.5: Spatially resolved image of the averaged NMR signal over the train of spin echoes in 2 stacked cloths. The colour bar represents the NMR signal in arbitrary units. The top cloth (in the closest proximity of a water source) generates less NMR signal than the bottom, contrary to what is expected.

In order to explore this effect, circular AC cloth samples with increasing diameter were cut and saturated with water for approximately 20 hours prior to the NMR experiment. Pairs of identical discs with increasing diameter sizes by 0.5 cm ranging from 0.5 until 4 cm were cut out from a cloth sheet.

The pair of identical cloth samples was stacked vertically and placed within the sensitive volume of the NMR Mouse®, see Fig.III.6.
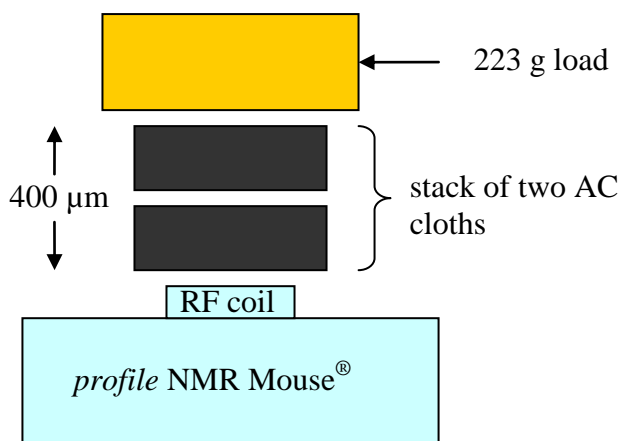
Fig.III.6: Sketch of experimental set up for scanning increasing discs sizes of a stacked pair of identical cloth samples. A load was placed on top of the cloths in order to flatten them. This load (made of Teflon) was chosen for its convenient cylindrical shape and its ability to be fitted easily on top of the system under investigation; it turns out to be 223 g.

The NMR signal was averaged for 10 minutes with the following settings: $T_E = 300$ μs, 64 echoes, $T_R = 600$ ms, acquisition time = 240 μs.

Each AC cloth was 200 μm thick, resulting in a sample total thickness of 400 μm which is well within the 600 μm thickness of the sensitive volume of the NMR Mouse[®]. A load of 223 g was placed on top of the two stacked cloths in order to flatten them.

III.2.5. RF heat deposition into the activated carbon monolith

RF currents generate RF electromagnetic waves which cannot penetrate deeply into electrical conductors but flow along the surface of conductors, through a process known as the skin effect. Skin effect is the tendency of an alternating electric current to distribute itself within a conductor resulting in the current density near the surface of the conductor being greater than that at its core. This is due to eddy currents set up by the alternating electric current. An eddy current is an electrical phenomenon, caused when a conductor is exposed to an externally applied changing magnetic field. The change in magnetic field can be either due to relative motion of the field source and conductor, or to variations of the field with time. This can cause a circulating flow of electrons, or a current, within the body of the conductor.

In order to estimate the heat generated in the AC by the pulsed RF field, a simple thermocouple was secured on one extremity of a channel from an AC monolith cylinder sample, with a height of 1 cm. The thermocouple was placed inside a peripheral channel of the AC monolith. Then the AC sample was placed on the NMR Mouse® to undergo an NMR measurement. This situation is highly representative of that of a "real" experiment except for the presence of the metallic thermocouple, see Fig.III.7.
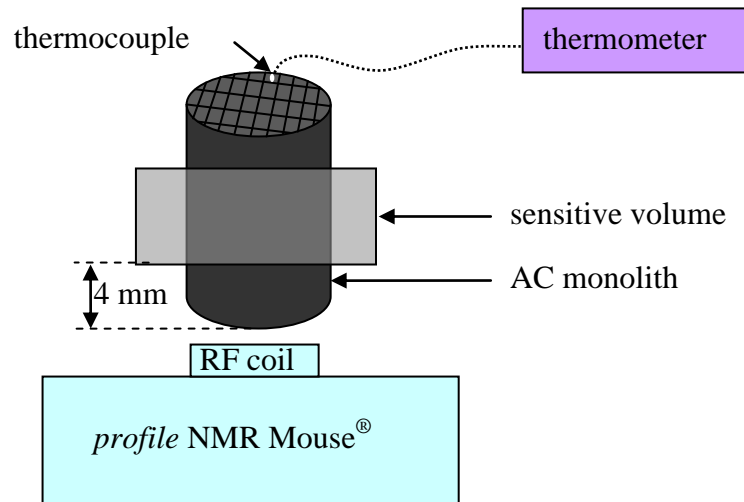
Fig.III.7: Sketch showing the geometry of the system. The selected slice is deep into the monolith as in a real experiment; this allows a measure of the effect of the RF inducing currents. A thermocouple was placed at a peripheral channel of the monolith to monitor the local rise in temperature as a function of the NMR repetition time, T_R.

The NMR pulse sequence settings of the CPMG were:

- $T_E = 100$ μs, a value typical of those echo times used in the experiments, and suitable to measure the typical T_2 values encountered, see Fig.III.11, (T_2 of monolith without rim = 2.7 ms, T_2 of intact monolith = 3.3 ms, T_2 of composite = 4.0 ms);

- acquisition time = 32 μs (irrelevant to heat deposition).

- 256 echoes, (resulting in a train length = 46 ms) a value typical of those echo numbers used in the experiments, and which is suitable to measure T_2 values of the order of tens of milliseconds.

- The repetition time T_R was increased for a set of individual different experiments: $T_R = 300, 500, 700, 1000$ ms.

For any given T_R value, the experiment was run until a steady state in temperature was reached; at that point, the NMR experiment was stopped. Thermometric readings were collected manually and recorded.

Unfortunately the thermocouple picked up some induced current from the RF pulse making the instantaneous thermometric readings rather difficult. To overcome this problem, the RF pulse sequence was simply switched off for 5 seconds, allowing enough time to read the temperature but not enough time for substantial cooling to occur.

A separate similar experiment was set - without the NMR apparatus - in order to measure an estimate of the intrinsic heat deposited within a monolith in the process of uptaking heptane vapour. A thermocouple was placed at the periphery of the monolith which was placed above a polytetrafluoroethylene (PTFE) well (see Fig.III.8) filled with heptane. Heptane vapour could reach the monolith from underneath.
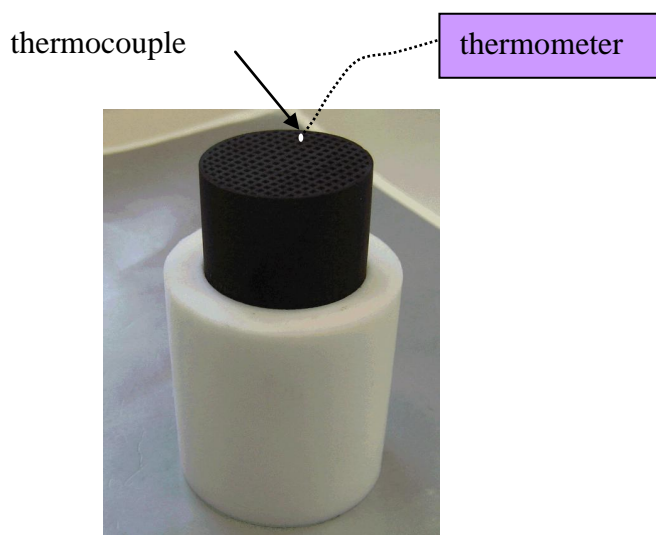
Fig.III.8: PTFE well hosting a source of liquid heptane. A monolith sample was placed above the well so that the heptane vapours reached the sample from underneath only. A thermocouple was placed at a peripheral channel of the monolith, just as is shown in Fig.III.7.

III.3. Results and discussion

III.3.1. NMR signal loss with depth scanning for the activated carbon monolith

The NMR signal was processed by fitting a T_2 exponential decay to the spin echoes in order to be able to extract the fitted NMR amplitude and the relaxation rate R_2.

When the AC sample was scanned at different depths, a severe NMR signal drop was observed with increasing depth for the intact monolith, see red curve on Fig.III.9, the attenuation reaching 50% at 4 mm. A less severe drop was seen for the monolith without a continuous rim, with an attenuation of 25% at 4 mm, see blue curve on the same figure. No measurable signal loss was seen in the AC composite, see black curve. Less absolute signal was seen in the composite than in the monolith samples, at the periphery the signal is 3 times weaker in the composite than in the monolith. The signal drop is due to a combination of B_1 transmit and B_1 receive amplitude drop, although the RF time duration was not optimised for each different depth that was scanned. The skin depth, δ, increases when frequency decreases and can be found through the following equation [76]:

$$\delta = \sqrt{\frac{2}{\sigma\mu\omega}} \, , \qquad\qquad \text{Eq [III.1]}$$

with:

δ: skin depth,

μ: permeability,

σ: conductivity,

ω: angular frequency.
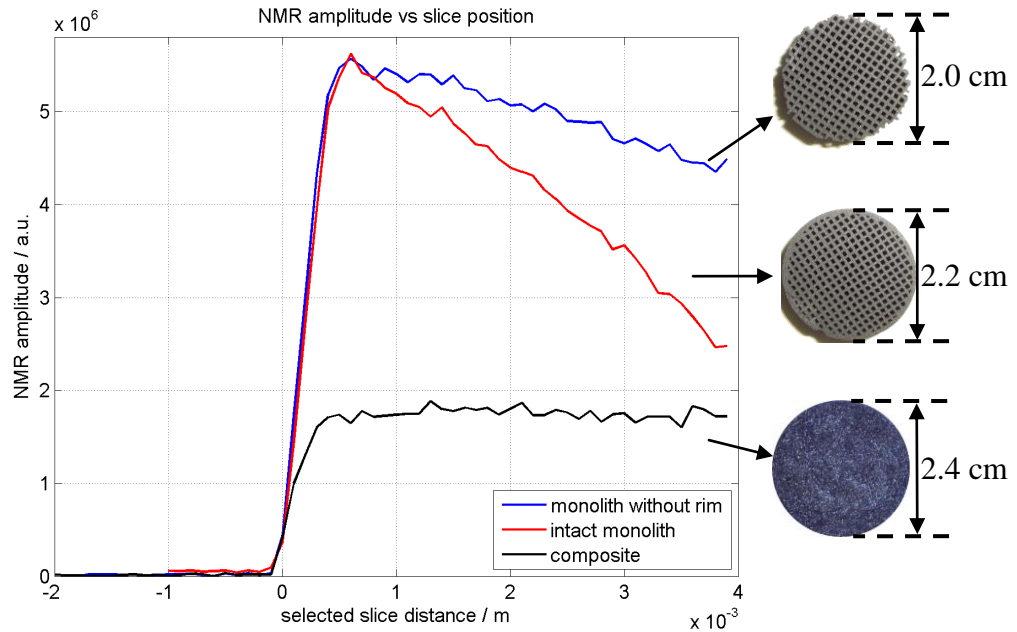
Fig.III.9: NMR amplitude of heptane measured as a function of depth in monoliths and composite. The deeper the selected slice is in the AC monolith, the stronger the attenuation of the measured NMR amplitude. No variation of the fitted amplitude is seen for the AC composite, its amplitude is also lower. For each curve, a photograph of the representative AC is supplied.

The experiment was repeated with the monolith turned up side down. The same phenomenon was observed. This further demonstrates that the RF wave is absorbed in the AC monolith, with strong deviations between different samples.

The assumption that the heptane saturation level had reached a steady-state was also checked. This is shown in Fig.III.10 and Fig.III.11. The depth scanning for the monolith with the intact rim (corresponding to the red curve on Fig.III.9) was done twice. One scan lasted three hours and a half.
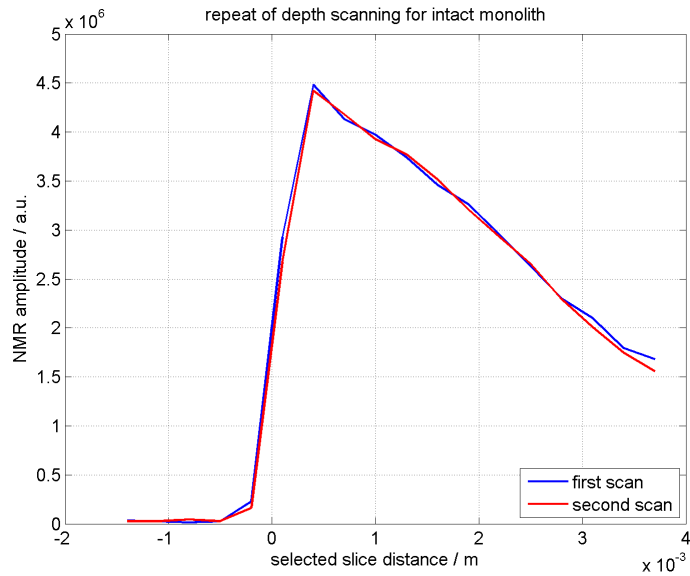
Fig.III.10: Repeat of depth scanning (for heptane) in the intact monolith. The second scan was run three hours and a half later than the first loop. The NMR signal from heptane in the monolith exhibits negligible deviations between the two runs.

It maybe concluded that negligible desorption of heptane (or adsorption of water coming from the laboratory) is occurring as the two curves are virtually superimposed.

Later on in chapter V it is discussed whether R_2 is an indicator of the level of saturation of the liquid residing in the AC. It is therefore very important to find out whether the relatively high electrical conductivity of the samples affects the measurements of the transverse relaxation rate, R_2. In order to do so, in addition of the fitted amplitude (Fig.III.9), the fitted R_2 is also shown for the three separate samples (Fig.III.11).
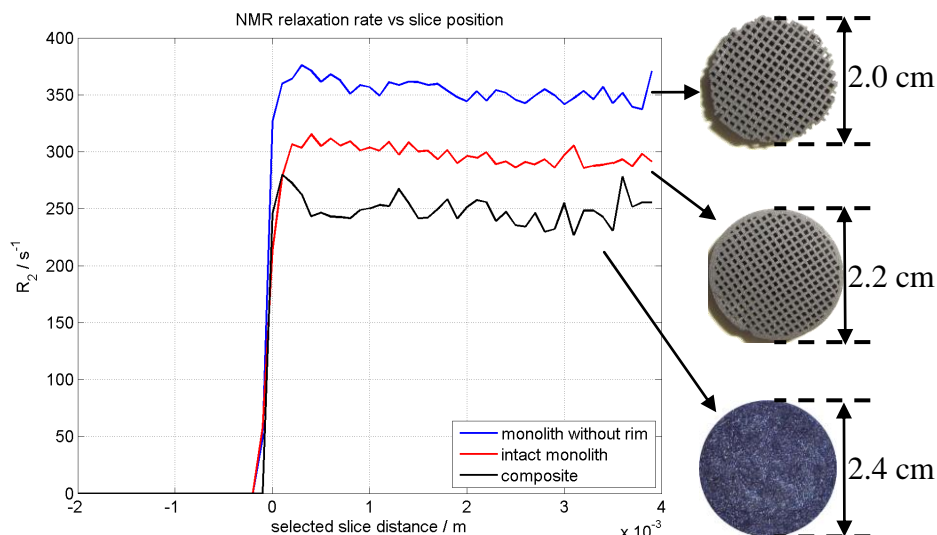
Fig.III.11: NMR relaxation rate of heptane measured at different depths in monoliths and composite. Negligible variations of R_2 as a function of depth are seen for the three separate AC sample. For each curve, a photograph of the representative AC is supplied again.

Inside the AC samples, the variation of R_2 is negligible (meaning that the saturation level of heptane remains constant as is shown later on in this thesis). As soon as the selected slice is moved outside the monolith, R_2 becomes meaningless because no NMR signal is being detected.

This study shows that R_2 is a parameter which may be reliably measured despite the sample's high conductivity. Its measurement is robust in any of the three AC samples, and at any location. This has important consequences in work discussed later (chapter V).

III.3.2. Effect of increasing discs size on the NMR signal

The NMR signal was processed by averaging out the spin echoes in order to plot the amount of the NMR signal for each different sample size.

The monolith and composite sample discs were rendered as thin as possible (by sanding them down) so that the entire sample sits within the selected slice and therefore any change in signal is only due to a change in diameter, see Fig.III.12.
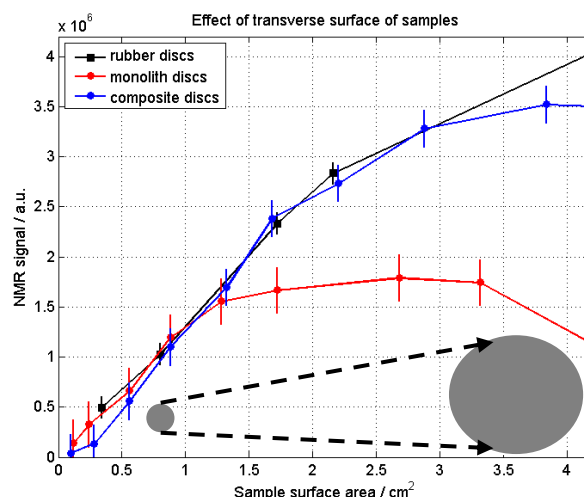
Fig.III.12: Effect of sample's transverse surface area, for monolith, composite and rubber. The monolith and composite sample discs were respectively 0.5 mm and 0.7 mm thick. The rubber samples were cut out of a bicycle inner tube and were 0.8 mm thick. A schematic representation of the increasing disc size is also shown on the graph.

For the monolith discs with varying diameter, the signal increases linearly with area up to an area of 1.2 cm^2. Above this value, linearity is lost and an asymptotic behaviour leading to a plateau is seen. The NMR signals coming from both the rubber and the composite samples are still evolving linearly with surface area until the entire *x-y* surface of the sensitive volume (*ca.* 2 cm^2) is reached. If the monolith is actually intact with its outer continuous rim (very last red point on the right hand side of the plot), the signal actually drops probably due to strong eddy currents generated in this outer ring. Note that the three curves have been scaled so as to compensate for absolute signal strength discrepancies coming from different relaxation times and protons density in each sample.

III.3.3. Effect of outer rim

Altering the rim of the monolith substantially changes the detected NMR signal strength, as can be seen in Fig.III.13. The intact monolith sample (**A** on Fig.III.4) exhibits a continuous conducting rim which, when removed (**C** on Fig.III.4), allows the collection of a signal three-times larger. This outer part of the sample is likely to experience substantial currents induced by the switching of the RF field which is needed for the NMR experiment. In the *profile* NMR Mouse®, the B_1 field is normal to

the instrument and therefore strongly couples with horizontal hoops such as that formed by the rim.
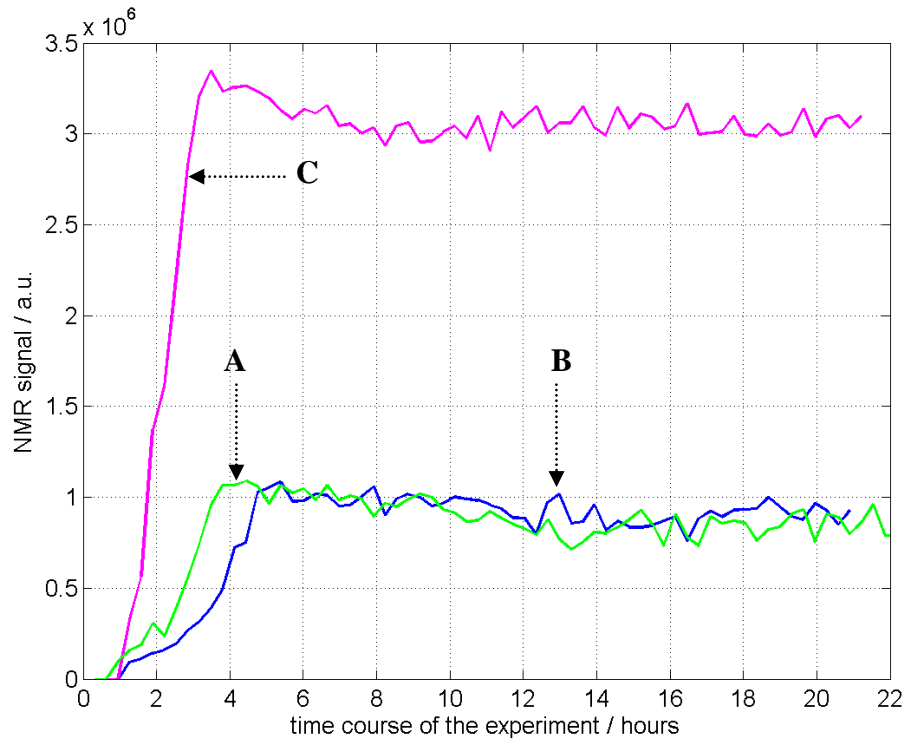
Fig.III.13: NMR Fitted Amplitude (FA) as a function of time for the three separate adsorption experiments. The green curve **(A)** represents the NMR FA from heptane adsorbed in the AC with an intact rim. The blue curve **(B)** is the signal for the case of a discontinuous rim. The magenta curve **(C)** is the signal for the case without the rim.

The data clearly demonstrates that without the rim, the detected NMR signal intensity is higher than when the rim is intact or when the continuity of the rim is interrupted. The signal from the monolith with a discontinuous rim (**B** on Fig.III.4) and with the intact rim (**A** on Fig.III.4) have the same intensity (curves **A** and **B** on Fig.III.13). This is evidence that the pulsed RF wave generates significant amount of current in the outer rim. By simply removing the outer rim, the NMR signal intensity is trebled. The main parameter that deteriorates the measurements seems to be the transverse surface area of the samples.

III.3.4. Effect of size of activated carbon cloth

The NMR signal is Fourier transformed in order to obtain a one dimensional profile along the *z* axis for pairs of increasing disc size of cloth. Note that due to the shape of the frequency response of the instrument, which resembles a gaussian (see section II.1.4.), the profiles from the cloth are modulated by a gaussian. The sensitivity in this gaussian variation is corrected along the *z* axis by dividing the sample profile by a gaussian profile which is obtained from a homogeneous liquid sample. Following this, the NMR signal emitted from the specific part of those profiles corresponding to each individual cloth is integrated, see Fig.III.14. This results in the amount of NMR signal respectively collected for both the bottom and top cloth for the increasing disc sizes.
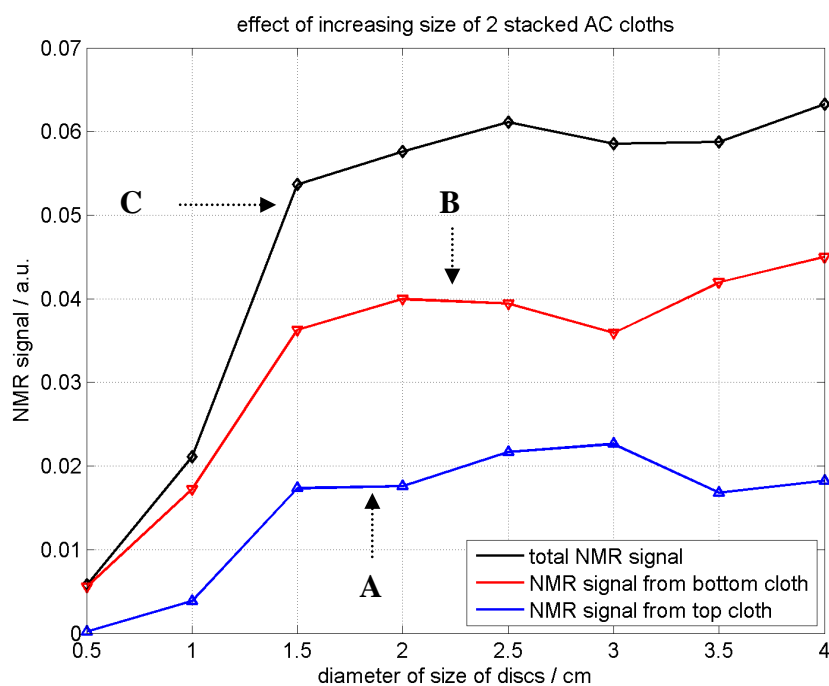
Fig.III.14: Effect of size of diameter of the AC cloth. The blue curve (with triangles pointing upwards) **(A)** represents the NMR signal from heptane sitting in the top cloth. The red curve (with triangles pointing downwards) **(B)** represents the NMR signal from heptane sitting in the bottom cloth. The black curve (with diamonds) **(C)** represents the total NMR signal coming from both stacked cloths. It is seen that the bottom cloth **(B)** systematically demonstrates higher NMR signal than the top cloth **(A)**.

The signal from the bottom cloth clearly shows higher amplitude than that of the top cloth.

For an increasing diameter of cloth from 0.5 to 1.5 cm, the curves increase similarly.

Above 1.5 cm, the signal from the top cloth reaches a plateau whereas that coming from the bottom cloth still increases slowly until a size of 2 cm in diameter is reached. Beyond that, the limitation of the sensitive volume is reached explaining the plateauing of the three curves. Above discs size of 1.5 cm in diameter, the NMR signal coming from the bottom cloth is approximately twice as strong as that coming from the top cloth. This results in the overall integrated NMR signal being similar to the integrated NMR signal of the bottom cloth.

The same experiment was repeated with swapping the stacking order of the cloths, see Fig.III.15.
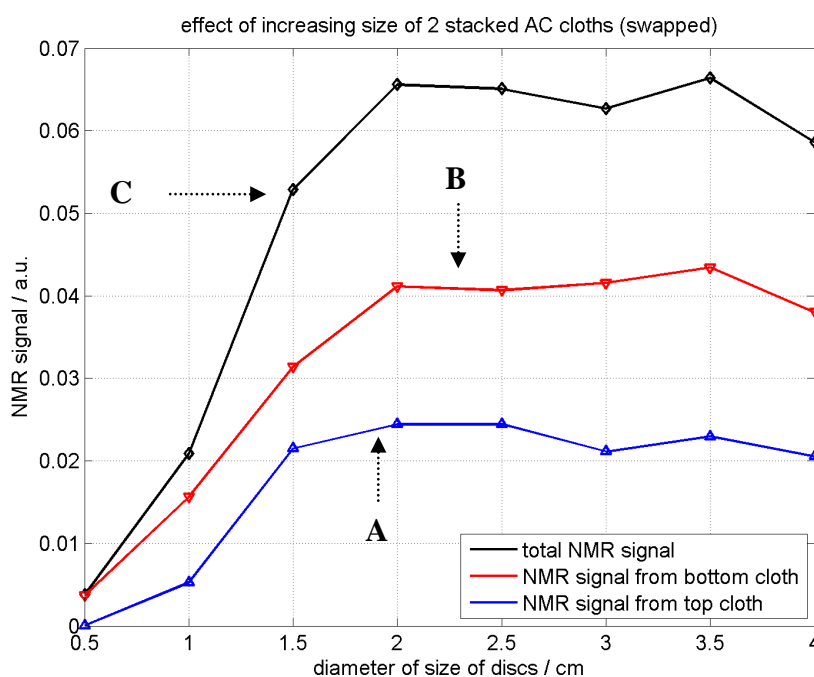
Fig.III.15: Effect of size of diameter of the AC cloth. Data very similar to that seen in Fig.III.14 is obtained. The only difference is that the stacking order of the cloths was swapped. The blue curve (with triangles pointing upwards) **(A)** represents the NMR signal from heptane sitting in the top cloth. The red curve (with triangles pointing downwards) **(B)** represents the NMR signal from heptane sitting in the bottom cloth. The black curve (with diamonds) **(C)** represents the total NMR signal coming from both stacked cloths. The bottom cloth **(B)** systematically demonstrates higher NMR signal than the top cloth **(A)**.

The same results as from the previous figure can be drawn. Although few variations can be seen and reside in the fact that for this particular experiment a high zero-frequency component was encountered, which results from a spurious signal from the electronics operating the amplifiers of the NMR Mouse[®]. This can be somewhat compensated for

in post-processing the data by removing the NMR signal comprising the zero-frequency component and by replacing it with neighbouring NMR signal.

The percentage difference between the strength of the NMR signal found in the two stacked cloths (swapped or not) can be calculated, see Fig.III.16.
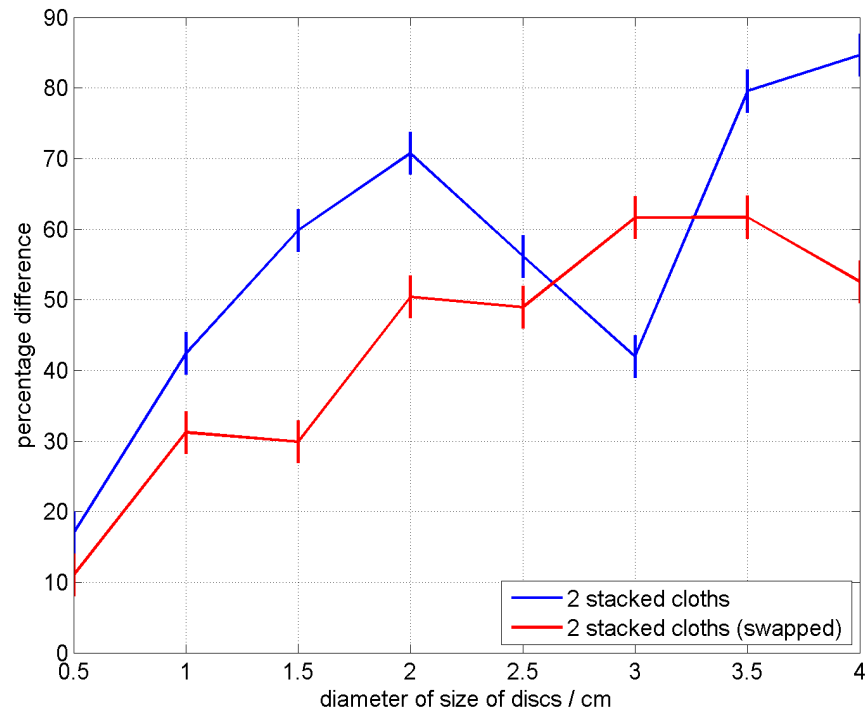
Fig.III.16: Percentage difference between the strength of the NMR signal found in the two stacked cloths. The red curve represents the result for the swapped stacking order of the cloths.

The percentage difference between the two cloths is the smallest for the smallest disc size and is increasing as the disc size increases. This proves that the substantial differences in signals seen between the two cloths in Fig.III.14 and Fig.III.15 do not come from different saturation levels but from electromagnetic shielding.

These experiments show that to quantify the NMR signal coming from the vertical stack of two cloths together, the surface cannot be more than 1.5 cm in diameter. The conductive cloth shields and interferes with the real NMR signal, and this must be accounted for if quantitative measurements are required.

III.3.5. Working at an optimized T_R value to minimize heat generation in activated carbon monolith: temperature drifts due to B_1 effect

In all the heat deposition experiments, it was found that within approximately 30 minutes the steady-state temperature is reached and takes increasing values of 9°C, 7.5°C, 4.5°C and 3.5°C for respective T_R values of 300 ms, 500 ms, 700 ms and 1000 ms, see Fig.III.17.
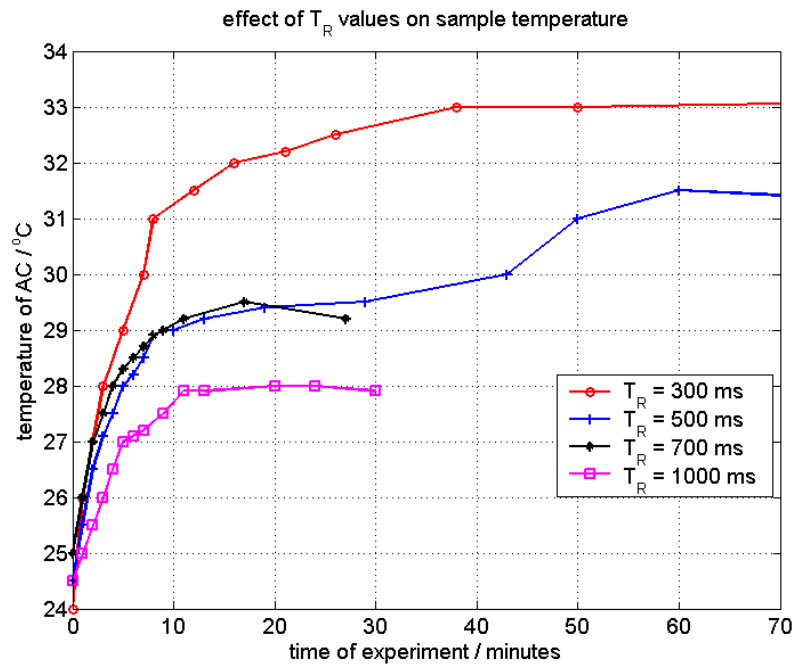
Fig.III.17: Rise of temperature of the AC monolith exposed to pulsed RF. The red, blue, black and magenta curves respectively represent the temperature of the monolith for T_R = 300, 500, 700 and 1000 ms. All measurements were run until the steady state temperature was reached. The increase in temperature seen at 45 minutes for a T_R value of 500 ms is genuine and corresponds to a change of the echo time from 180 µs to 100 µs. This change was unintentional and corrected for towards the end of this particular experiment, which still yielded a meaningful result with regards to the steady state value of the temperature reached at 70 minutes.

It is in the 10 first minutes that the temperature increases most rapidly. Unfortunately, for a short T_R value of 300 ms a temperature change of 9 °C is clearly seen. One way to compensate for this could consist in driving a continuous air flow at a steady temperature to help to keep the sample at a well defined temperature so that the technique remains sufficiently non-invasive. However (if possible) the repetition time should be set to a value well above 300 ms, around 1 s.

Fig.III.18 summarizes the steady state results from Fig.III.17. The maximum

temperature of the monolith is clearly correlated with its value of $1/T_R$ (as expected).
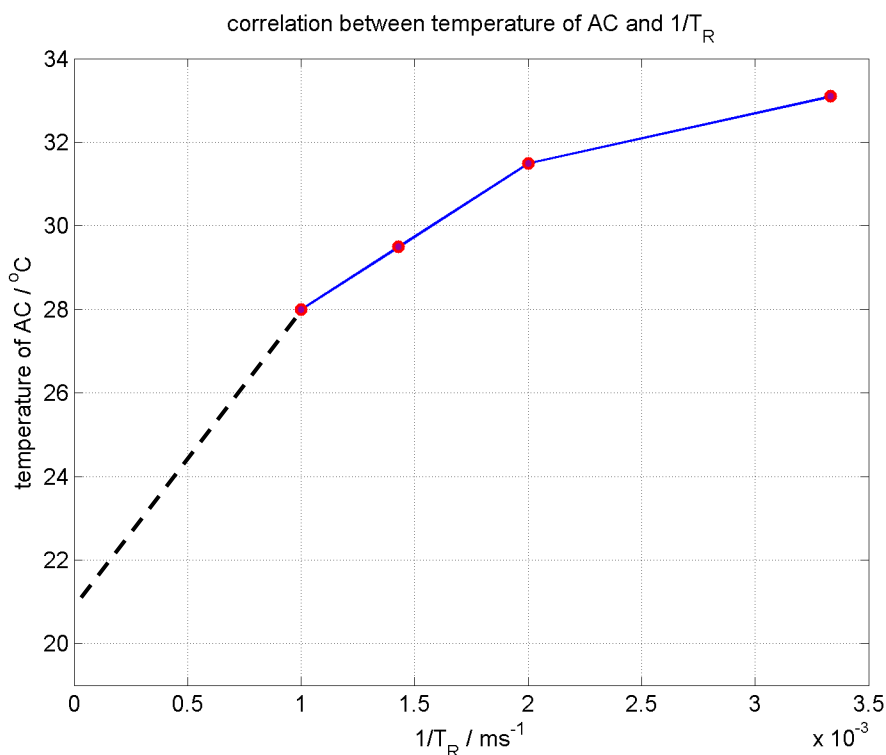
Fig.III.18: Graph demonstrating the correlation between the maximum temperature reached in a AC monolith and the value of $1/T_R$ of the NMR experiment. The higher the $1/T_R$ values, the higher the maximum temperature obtained. The dashed line on the graph is manually added (by interpolation) in order to give an idea of the trend of the curve starting at the y intercept.

Although the curve does not yield a linear relationship, the laboratory temperature (21 °C) is used for $1/T_R = 0$ and this gives the dashed line as an interpolation.

For the experiment where the intrinsic rise of temperature of the monolith (due to the adsorption process) was monitored, the temperature was found to increase by almost two degrees in 11 minutes. After 80 minutes, the temperature started to decrease. The next day, the monolith was again at room temperature, which was 21 °C. The heptane reservoir was not empty demonstrating that the vapour was still being fed to the AC monolith.

These results are accounted for in further experiments (shown in chapter V) by running them with a T_R value of 800 ms with 128 spin echoes, ensuring that the temperature increase was kept to an acceptable level of less than 2 °C in order to keep the technique relatively non-invasive. Note that a temperature change of 2 °C complies with the

random temperature deviations seen over 24 hours whereas 9 °C renders the technique too much invasive.

The AC cloth is substantially less conductive than the monolith samples so that their temperature increase is expected to be well below 2 °C for $T_R = 800$ ms.

III.4. Conclusion

The high conductivity of the AC samples clearly makes them challenging for NMR measurements. NMR signal with good SNR still can be obtained if the periphery along the z axis of the monolith sample is monitored.

Whilst the AC monolith could only reliably be probed at its extremity, the AC composite can be scanned at any depth without any loss of signal. In addition, it can be said that for the monolith a very large SNR can be gained - whilst the relevance of the experiments in chapter V are kept intact - by removing the continuous conducting ring.

It has also been seen that the NMR signal is dependent on the size of the surface area of AC cloth, and that it cannot exceed more than 1.5 cm in diameter in order to obtain quantitative NMR information from two stacked cloth. At this value, a shielding effect created by the cloth is seen but a reasonable amount of NMR signal is still collected.

In chapter V it will be demonstrated that there is excellent agreement between NMR and gravimetric measurements, validating the quantitative nature of the NMR measurements.

Because of its high electric conductivity, monitoring heptane uptake in AC monolith using the *profile* NMR Mouse® is vastly enhanced by physically altering the sample. As far as the author knows, chapter V shows the first successful NMR measurements of gas uptake in such a highly conductive porous medium with the use of unilateral low field pulsed NMR. However, as mentioned in chapter II, Conard *et al.* obtained (in 1970) adsorption measurements on AC by using high resolution NMR spectroscopy. Their work differs from this thesis as they measured adsorption with an instrument that

does not possess any field gradient. They measured the change in line width and/or in chemical shift as a function of surface layer covering of an adsorbate on AC samples which were either in the shape of a thin powder or had suffered grinding prior to the experiment. The AC samples in this thesis work do not require any crushing and can be used as they are found on the commercial market. In this case, the surface layer covering of a vapour on AC is monitored by means of changes in the fitted T_2 and/or in the fitted NMR amplitude or by simply averaging signal from Fourier transformed spin echoes. These T_2 measurements are those that suffer the least from artefacts due to the electrical conductivity of the samples. This suggests that T_2 measurement is a way forward to evaluate the saturation level.

CHAPTER IV: IMAGING LIQUID INGRESS IN PROTECTIVE MATERIALS USING A UNILATERAL NMR INSTRUMENT

INTRODUCTION

Two types of experiments involving liquid ingress were conducted on textiles. In the first, short applications of increasing pressure were used. In the second, ingress due to long duration steady state moderate pressure combined with gravity and capillary flow was monitored.

Experiments into liquid ingress of the "first type" were also realized on a fabric made of a combination of repellent layers and activated carbon cloth.

Since the signal frequency can be calibrated as a function of the z coordinate, spatially resolved measurements where liquid ingress occurs can be conducted without the need for moving the sample relative to the instrument, provided that the vertical field of view of interest is less than 500 µm.

In this chapter the advantages and drawbacks of spatially resolved Fourier Transform (FT) NMR are described followed by the description of the experimental protocol and the results of experiments exploring oil ingress firstly in fabric and secondly in fabric and cloth combined all together.

IV.1. Advantages and disadvantages of FT NMR against physical spatial resolution

There are at least two ways that can be used in order to spatially resolve (vertically) the NMR signal with the *profile* NMR Mouse®.

One technique, named as the FT NMR technique, consists of acquiring NMR signal without moving the sample relative to the instrument. The strong intrinsic field gradient is used in conjunction with the RF pulses in order to collect spin echoes that can be

processed by at least two separate procedures in order to obtain 1D profiles: one consists in averaging the spin echoes of the CPMG train (for one measurement) and then Fourier transforming it in order to reveal an averaged T_2 weighted 1D profile. The second consists in fitting a T_2^{eff} exponential decay to the spectra of the spin echoes in order to extract a 1D profile of both the transverse relaxation rate and the fitted NMR amplitude (proportional to the absolute volume of liquid present at a given position across the slice).

The other technique, referred to as the physical motion method, consists in acquiring NMR signal at different positions of the selected slice of the instrument relative to the sample under investigation. Either the instrument or the sample needs to be moved physically (which can be done manually or by the help of a lift). If needed, the NMR signal can be processed just as in the first technique, or the spin echoes can simply be averaged together without any further processing.

Note that the group in Aachen (Germany), manufacturing the *profile* NMR Mouse[®], has extensively published work by mostly (if not exclusively) using the physical motion method.

In the case of the instrument used in this thesis work, the powerful FT NMR technique was used to produce 1D spatially resolved profiles. This method can generate extremely high spatial resolution: 15 μm if the entire surface is sampled or even less (1 to 5 μm) if part of the sensitive transverse section is used. This is due to the shape of the selected slice which is not a "perfectly" flat section but exhibit a curvature with a sag of *ca.* 15 μm between its middle and its extremities (which are *ca.* 1.5 cm apart of each another). In addition, the temporal resolution is good (here 4 minutes for one profile) as it captures the whole sample at a time. It suffers no hysteresis whereas with the second method there is a 15 μm hysteresis due to the use of the stepper motor.

The FOV does not exceed 500 μm whereas when the sample is moved physically relative to the instrument, up to 10 mm can be spatially resolved. This FOV is also adjustable by changing the distance between the RF coil and the magnet assembly

(already explained in section II.2.2.) but a rapid drop of B_1 field strength also causes a rapid drop of the SNR with increasing distance.

Finally, as discussed already, the instrument is sensitive to temperature. Both methods suffer for a spatial shift of the signal due to temperature drift (*ca.* 20 μm for 2 °C).

IV.2. Description of the fabrics composed of thin textile layers

IV.2.1. Heterogeneous fabric

The model heterogeneous repellent textile sample used in this work was constructed from three layers (see sample under investigation on Fig.IV.8) of a non-woven material (with surface density of 17 g.m^{-2}) supplied by Web Dynamics Ltd (based in Blackrod, UK) to the DSTL who then modified some of them in order to render the fabrics liquid repellent. These fabrics were then provided for use in the research of this thesis. These layers, each approximately 70 μm thick, were cut into approximately square (23 × 24 mm) sections for the NMR measurements (the first time those layers had been cut, attention was not brought to the fact that they were not rendered perfectly square). The textiles are composed of entangled meltblown polypropylene fibres (approximately 10 μm in diameter, Fig.IV.1) that have been consolidated into a non-woven textile.
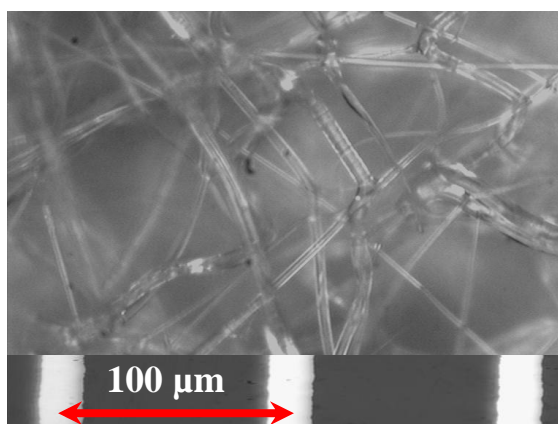
Fig.IV.1: Optical microscope image of entangled fibres within a repellent layer. The image would be the same for a non-repellent layer.

The porosity of a non-repellent fabric was measured using the NMR instrument. This was done by dividing the NMR profile of the fabric sample which was saturated with

oil, by the NMR profile of a bulk sample of the same oil. This oil (Duckhams 15W/40 Mineral formula) is commercially available as an engine oil for motorcars. In chapter II, the reasons for using this particular oil were given (rapid collection of good SNR for short T_R values). Its T_1 is 31.3 ms and its corresponding optimum T_R value is 37.6 ms. The density of this oil was measured by gravimetric resulting in a value of (850 ± 20) kg.m^{-3}. Note that the NMR profiles were constructed by averaging out the spin echoes and not by performing a T_2 measurement as it was found that T_2 (27 ms) is not affected by the oil residing in the fabric. This measurement revealed a very high porosity (80 ± 9)% which allows a large quantity of liquid to be driven into the fabric.

IV.2.2. Repellency obtained with coating

In order to render the textile liquid repellent a fluorocarbon coating was applied prior to the construction of the three-layered non-woven material.

The fluorocarbon coated materials that were used in this investigation were supplied by the DSTL based in Salisbury (UK). The coating procedure that was used by them is described in detail elsewhere [84]. In brief, the samples were treated with a thin coating (approximately 100 nm) of a fluoro-polymer via the plasma-assisted polymerisation of the fluoroacrylate ($C_8F_{17}CH_2CH_2OC(O)CHCH_2$). This technique operates at the vapour pressure of the fluoroacrylate monomer (8×10^{-2} Torr). In order to exclude air from the system the sample is initially pumped down to a pressure of 1×10^{-3} Torr prior to the monomer vapour being introduced. A plasma is then produced by using an RF electric field (typically 13.56 MHz) to ionise the fluoroacrylate monomer. The RF power is pulsed on the microsecond timescale to limit fragmentation of the monomer and the deposited polymer thereby maintaining the structure of the liquid repellent fluoropolymer.

A droplet of liquid will not wet a textile treated with the fluorocarbon coating if the contact angle formed between the liquid and the textile is sufficiently large [20, 85-86].

The Young's law contact angle, defined in section I.1.2., applies for an *ideal surface*. When performing experimental measurements of contact angles on rough and not

homogeneous surfaces, hysteresis exists and a range of contact angles are possible. In addition, the surface roughness can modify the measured contact angle [85, 86]. Experimentally, for a given drop resting on a surface an apparent contact angle is measured. The history of the theory behind these phenomena has been reviewed elsewhere [19, 87, 88]. The apparent contact angle [89, 90] is the angle measured from the direction parallel to the x-y plane at any given point on the contact line to the tangent to the liquid-fluid interface at this point, see Fig.IV.2.
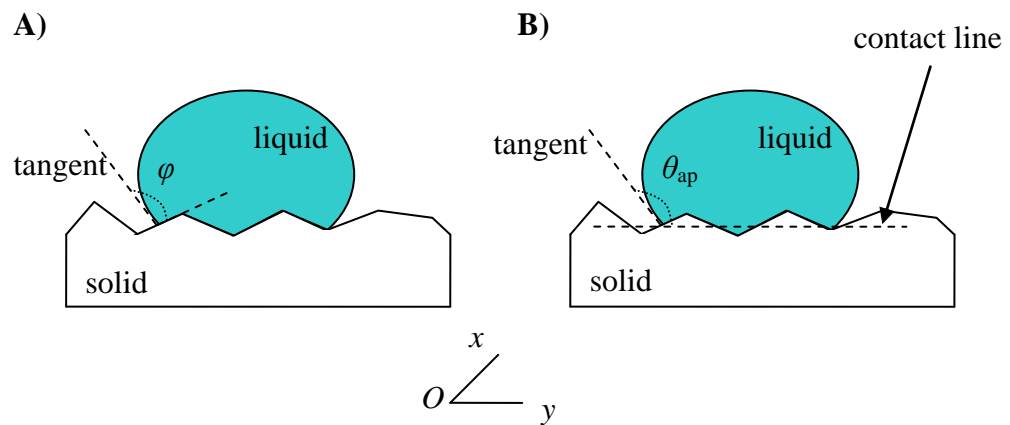
Fig.IV.2: Sketch [89, 90] representing **(A)** Young's contact angle, φ, and **(B)** the apparent contact angle, θ_{ap}, of a liquid resting on a non-ideal surface (rough and heterogeneous). The x-y plane is determined by the axes Ox and Oy, and is parallel to the solid surface.

More recently, McKinley [91] demonstrated that the wetting of a fabric is correlated to a factor referred to as the robustness factor. The robustness factor is defined as a parameter characterising the quality of being able to withstand stresses, pressures, or changes in procedure or circumstance *i.e.* if the droplet is subjected to a sufficient applied pressure it can be forced into or through the fabric.

The porosity of a repellent layer is difficult to measure as it is not wettable. In addition this repellent layer is designed to either stop liquids penetrating the fabric or to re-take its unsaturated state once the liquid as been forced across it. The fact that only 100 nm of fluoropolymer coats the 10 µm thick fibres gives a low relative percentage of difference in porosity of 1% between the coated and non-coated fabrics. Therefore, the porosity of the repellent layer can be estimated to be similar to that of the non-repellent layer within 1%.

The contact angle of a Duckhams oil droplet resting on a repellent layer was measured and found to be (137 ± 1) degrees. This angle was determined using a digital JVC colour video camera and Drop Shape Analysis software produced by KRUSS, see Fig.IV.3.
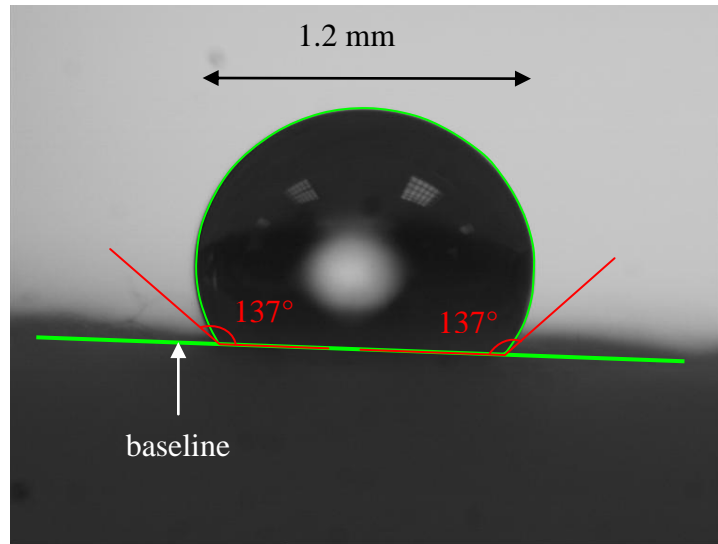
Fig.IV.3: Contact angle formed by 6 μL of Duckhams oil sitting on a repellent layer. The photograph was taken with a digital JVC colour video camera.

On Fig.IV.3, the baseline is determined manually for contact angles greater than 90°. The contrast between the droplet and the white background needs to be very sharp so that the software can reliably fit the profile of the droplet. The software then estimates the contact angle. The red lines showing the angles were added manually to the photograph.

From the contact angle, physical properties of interaction between solid and liquid like wettability (liquid spread), and repellency can be studied. Typical evaluations are as listed below:

- Low values of the contact angle, φ, indicate that the liquid spreads, or wets well, while high values indicate poor wetting.
- If φ is less than 90° the liquid is said to partially wet the solid, if it is greater than 90° it is said to tend to non-wetting. A zero contact angle represents complete wetting.
- Another case is considered where φ can exceed 150° and the droplet is mobile; the surface is then called superhydrophobic or superoleophobic to that liquid.

Such surfaces are seen in nature where the leaves of the lotus plant have surfaces that are extremely difficult to wet by water.

According to the measurement done with the high speed JVC camera, the surface of the coated layer is strongly hydrophobic because the contact angle is high.

An additional parameter that is informative when determining liquid repellency is the contact angle hysteresis. This is the difference between the advancing angle (the largest contact angle before the contact line moves when droplet volume is increased) and the receding angle (the smallest contact angle before the contact line moves when droplet volume is reduced) of a droplet. Often the difference in front and rear contact angles at the point when a droplet first moves as a substrate is tilted is taken as an indication of the extent of contact angle hysteresis, see Fig.IV.4.
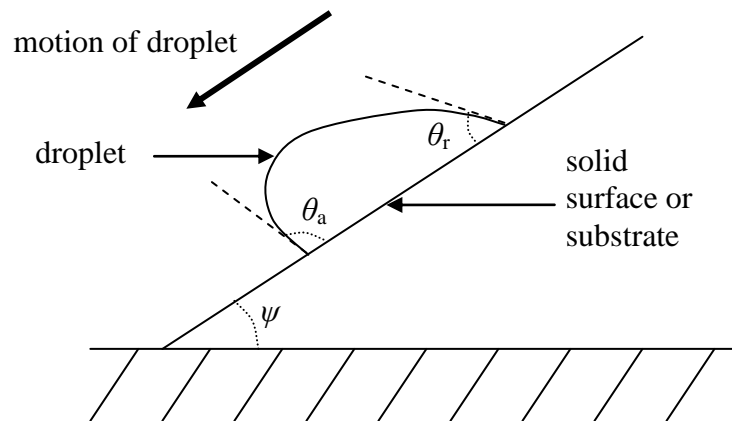
Fig.IV.4: Droplet moving on a repellent layer. The advancing angle, θ_a, and receding angle, θ_r, are as defined on the sketch. The angle, ψ, of a substrate when the droplet starts sliding downward is called the sliding angle.

In this case, the contact angle hysteresis is high because the droplet does not roll or slide on the surface even when the fabric (supporting the droplet) is rotated to a vertical orientation.

The fact that both the contact angle and the contact angle hysteresis are high indicates some penetration of liquid between the fibres corresponding to a *penetrating state*. In the literature, when the liquid is in intimate contact with the solid asperities, it is said that the droplet is in the Wenzel state, see Fig.IV.5. The lack of sliding motion in this case indicates either a full or partial Wenzel state.
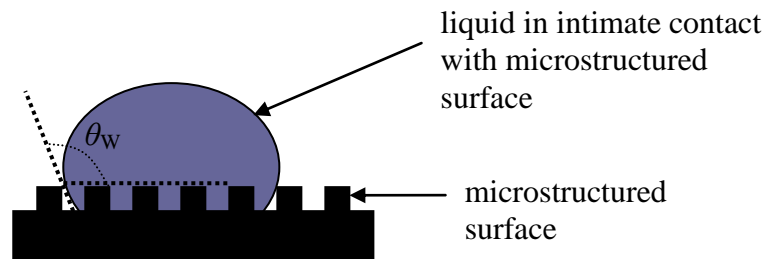
Fig.IV.5: Sketch representing Wenzel's state of a droplet resting on a solid surface. θ_W is the Wenzel contact angle. The liquid is in intimate contact with the solid asperities.

IV.2.3. An activated carbon cloth as a textile layer

Instead of building a fabric by only combining repellent and non-repellent layers, one alternative is to use an AC cloth layer. As opposed to the repellent and non-repellent layers, AC cloths can adsorb vapours in high quantities.

Two different types of AC cloth (see Fig.IV.6), each having a different size of channels were produced by MAST Carbon International ltd (based in Guildford, UK) and provided for use in this thesis work by the DSTL. The channels are in the shape of a diamond with diagonal sizes of 300 μm x 120 μm for cloth **A** on Fig.IV.6 and sizes of 1000 μm x 400 μm for cloth **C** on Fig.IV.6. In this chapter, the focus is on the one having smaller channels. Further details and characterisation of the cloth are presented in the next chapter.

Here, the focus is on textile cloth so that it is used as wettable material but in the next chapter the adsorbent properties of the AC cloth, monitored by NMR, are also explored.
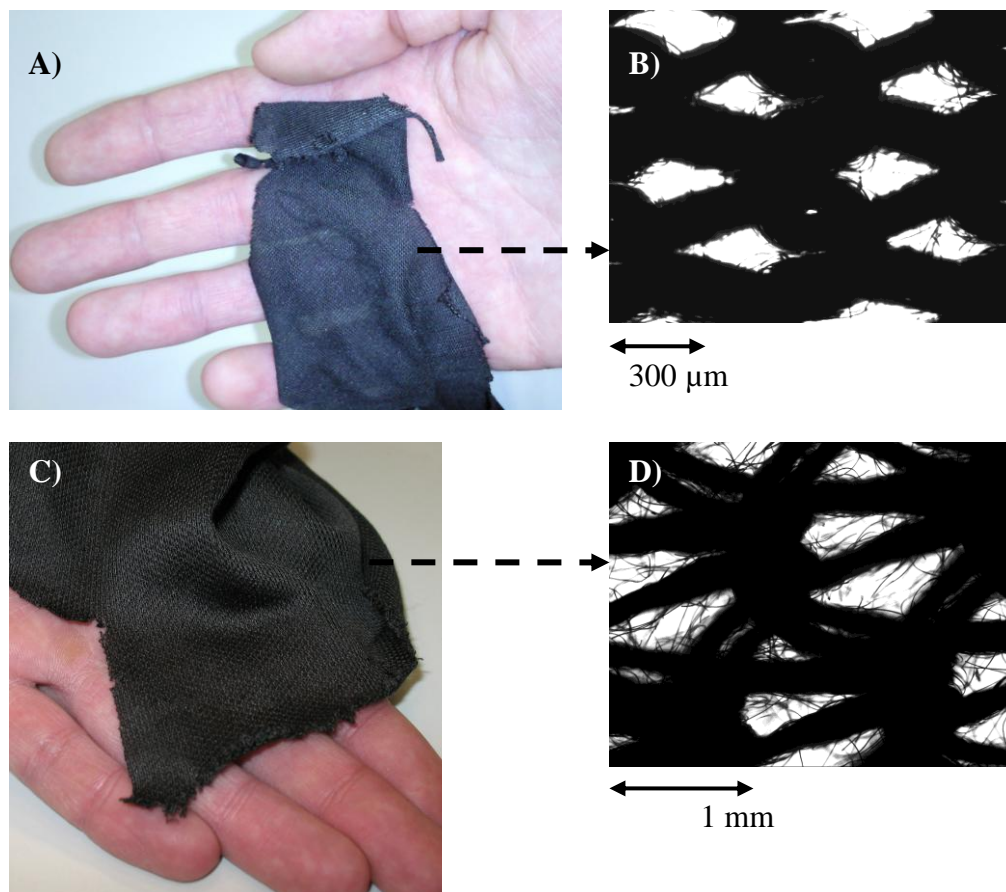
Fig.IV.6: **(A)** and **(C)** are photographs of two different AC cloths obtained by woven method, *viz.* respectively CF2 and JP2. **(B)** and **(D)** are optical microscope images of the AC cloths showing more details. The voids, in white, are channels and the ones seen on the AC cloth JP2 are of a bigger size than the ones seen on the AC cloth CF2.

IV.3. Experimental protocol

IV.3.1. Oil ingress into textile fabric

In this type of experiment, the first step in setting up the instrumentation consists of placing the thin layer of fabric in the centre of the sensitive volume of the *profile* NMR Mouse®. For the first experiment described in this chapter the NMR apparatus was used without its lift, therefore a combination of 1 mm and 166 µm thick microscope slides were placed between the sample and the top plate of the NMR instrument so as to achieve correct sample-to-instrument relative location.
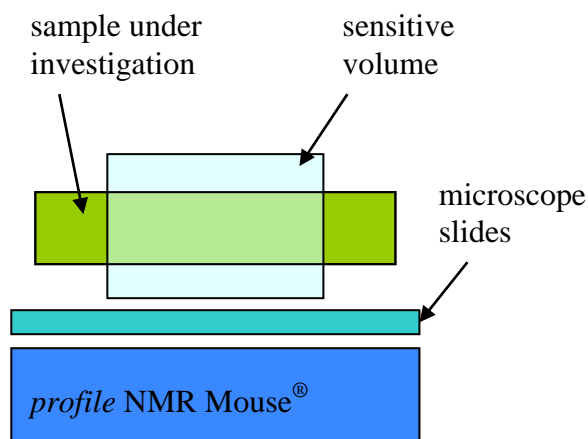
Fig.IV.7: Schematic representation of a sample placed at correct height so that it sits within the thickness of the sensitive volume.

The experiment consisted of placing a 7 µL droplet of Duckhams oil on the fabric, in the (x, y) centre of the sensitive area. The deviations in the volume of the droplet deposited with a 10 µL Gilson pipette were measured by calculating the standard deviation of 20 different samples where the mass difference of liquid sitting on a glass plate and the same glass plate without the liquid was measured. It was found that small quantities of liquid sitting outside the end of the tip can cause very large deviations in this volume, and thus very large increases in this volume. When this effect is minimised by driving the tip of the pipette gently in and then out of the liquid and thus avoiding liquid hanging at the end of the tip, the expected volume of 7 µL is reached with enhanced accuracy, with deviations of the order of 2% instead of 29%.

The sample under investigation was made of three layers where the middle layer of meltblown non-woven material was non-repellent whereas the outer layers were liquid-repellent, see Fig.IV.8.

Prior to any NMR measurement, a light load (40 g) was systematically applied on the top of the sample under investigation so as to keep the space between the individual layers a constant between successive experiments (each NMR measurement took approximately 4 minutes, representing 1500 accumulated averagings) and so as to minimise any naturally occurring warping of individual layers. In order to produce various pressure loads acting on the droplet of oil, the 40 g load was temporarily replaced by increasing volumes of water in increments of 60 mL, added to a plastic container placed on the top of the sample under investigation. This mass can be

converted into an effective applied pressure, because the weight is applied over the entire surface (5.5 cm^2) of the sample. The water load was removed after a duration of 30 s and the 40 g load was replaced onto the system prior to the NMR measurement. It is not known how much movement there is in the textile substrate under pressure. By choosing a load time of 30 s, a fair bit of the material is deformed as the liquid is forced through it; however, even for a "fixed" porous structure, wetting will occur under sufficient pressure. The experiment was repeated until a final water volume of 1080 mL was reached.

The NMR data was collected using a CPMG sequence with 40 spin echoes, (echo time, $T_E = 510$ μs, repetition time, $T_R = 170$ ms and acquisition time = 400 μs).
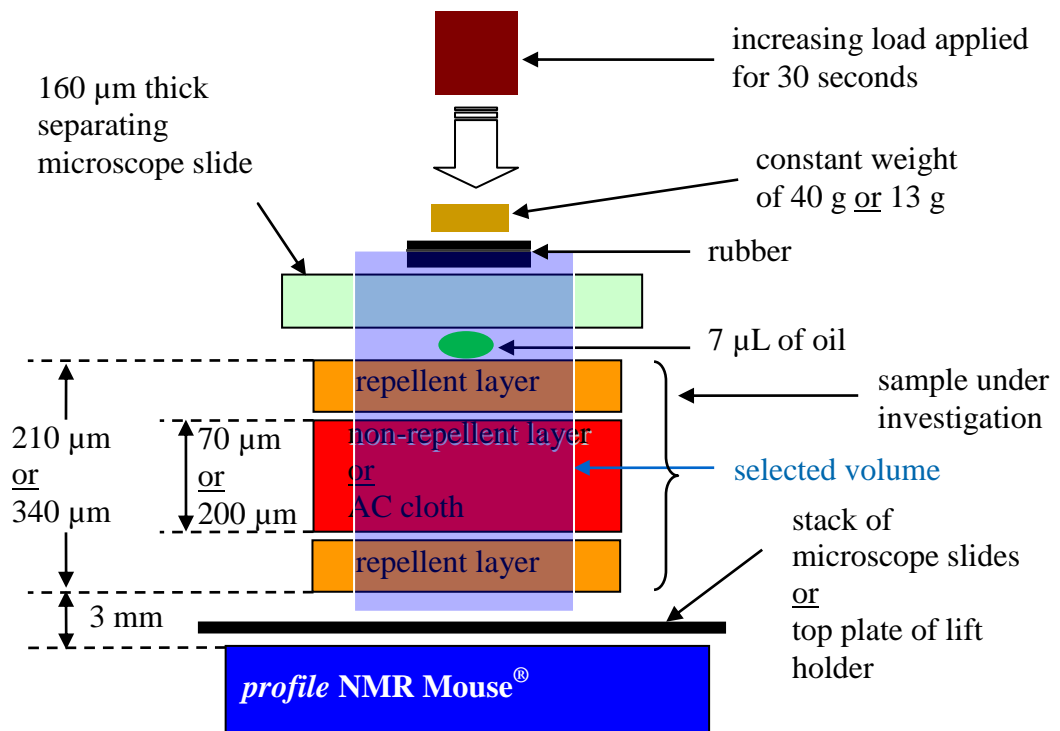
Fig.IV.8: Schematic representation of the experimental set up for the monitoring of oil ingress into textile based fabric. This representation is also used to describe the monitoring of oil into combined repellent layers with cloth (described in the next section IV.3.2.). These two set ups are very similar; they can be distinguished on this figure where the description preceding and following the word "or" is used respectively for this experiment and the one of the next paragraph. The oil droplet flattens out horizontally under the pressure applied by the constant weight forming a thin layer of oil between the bottom of the microscope slide and the top repellent layer.

In the case of liquid ingress due to long steady state pressure combined with gravity and capillary action driven fluid flow, the full final load was not applied. Instead, the

experiment was interrupted with a relatively light final load (180 g), just enough to ensure that some ingress through the first repellent layer had occurred. The light load was then replaced by the 40 g mass (as in all other measurements), and the ingress was then continuously monitored in an over-night NMR experiment for 18 hours, with profiles acquired every 25 minutes (and not 4 minutes) because the T_R value was set to be longer (1 s instead of 170 ms) in order to reduce RF-induced heat deposition, and also because high temporal resolution was not needed in this particular experiment. Note that the number of accumulated scans was kept constant, thereby producing the same SNR in both experiments.

IV.3.2. Oil ingress into fabrics containing activated carbon cloth

The fabric described in the previous paragraph can be altered by simply changing its inner layer with an AC cloth material. In this particular work a stack of 3 layers with an AC cloth (200 μm thick) sandwiched centrally instead of the non repellent fabric is investigated, resulting in the total thickness of the fabric under investigation of 340 μm instead of 210 μm. The new experimental arrangement is very similar to that of the one described in the previous paragraph; therefore the same Fig.IV.8 is used. However, here the Mouse® is secured to a lift allowing vertical motion with an accuracy of 15 μm. This lift simplifies the preparation of the experiment in that there is no need to use any stack of microscope slides between the sample under investigation and the Mouse®. A software controlled stepper motor allows the lift to be positioned in its stage.

The system is placed in the sensitive volume of the NMR Mouse®, the selected slice of which is set to be 3 mm above the instrument for enhanced sensitivity, as discussed in the previous section II.2.2., with a RF pulse time duration of 2.2 μs. Seven μL of oil was deposited on the repellent layer. The oil droplet was flattened with a 160 μm thick microscope slide. The previously used constant weight of 40 g was replaced by a 13 g weight because it was found to be heavy enough to ensure suitable stacking of the fabrics. Also, in this manner the drive of producing ingress (due to the constant weight) was reduced as less weight was acting on the oil droplet during the NMR experiment. The same loading protocol as described in section IV.3.1. was applied on the 5.5 cm^2 sample under investigation. However, the AC cloth acts as a RF shield, therefore the

averaging factor was increased from 1500 to 2300 in order to compensate for SNR loss, resulting in an experimental time increase to 7 minutes 43 s. The NMR experiment was repeated after each increase of 60 mL of water starting at a volume of 0 mL until a maximum volume of 1200 mL was obtained. The NMR data were collected using the usual CPMG sequence, but in comparison with the previous experiment, the settings were altered (128 spin echoes, T_E = 400 µs, acquisition time = 350 µs and repetition time T_R = 150 ms) as a response to the use of AC cloth.

IV.4. Dynamics of liquid ingress into multi-layered fabric

IV.4.1. Data processing

The spatially resolved NMR profile corresponding to a specific experiment can be drawn using the following data processing: each digital point of the Fourier transformed spin echo train (except for the three first, see explanation further down) was fitted to an exponential decay function (Eq [II.11]) in order to extract the vertical profiles of the NMR amplitude and the relaxation rate (R_2). Each individual profile was shifted relative to the first one, so as to have all rubber fronts aligned, as discussed in section II.2.6.2. The profiles of the local amplitude were then scaled (method explained in section III.3.4.) according to that of the homogeneous sample, so as to obtain the local oil linear density at a position, z.

The first echo in a CPMG train measured in a strongly inhomogeneous field is a direct echo or a pure Hahn echo and only emanates from the transverse magnetisation while the second and further echoes are affected differently by transverse and longitudinal relaxation as well as by diffusion in gradient fields [92]. Therefore, the first echo is typically lower than the second echo. However, the echoes following the second one exhibit an exponential decay, to which an "effective" T_2 relaxation time may be fitted, which is relatively close to the "true" T_2 time [78]. In spite of not being the "true" relaxation time, this effective relaxation time is extensively used, for example for oil well logging purposes [72].

IV.4.2. Results

IV.4.2.1. Oil ingress into layered fabric

The processed NMR profiles were stacked from left to right, interpolated and colour-coded, see Fig.IV.9. Note that when the repellent or non-repellent fabric, free from any fluid (except air) saturating its pores was placed in the sensitive volume of the instrument, no signal was detected, thus confirming its transparency to the NMR experiment.
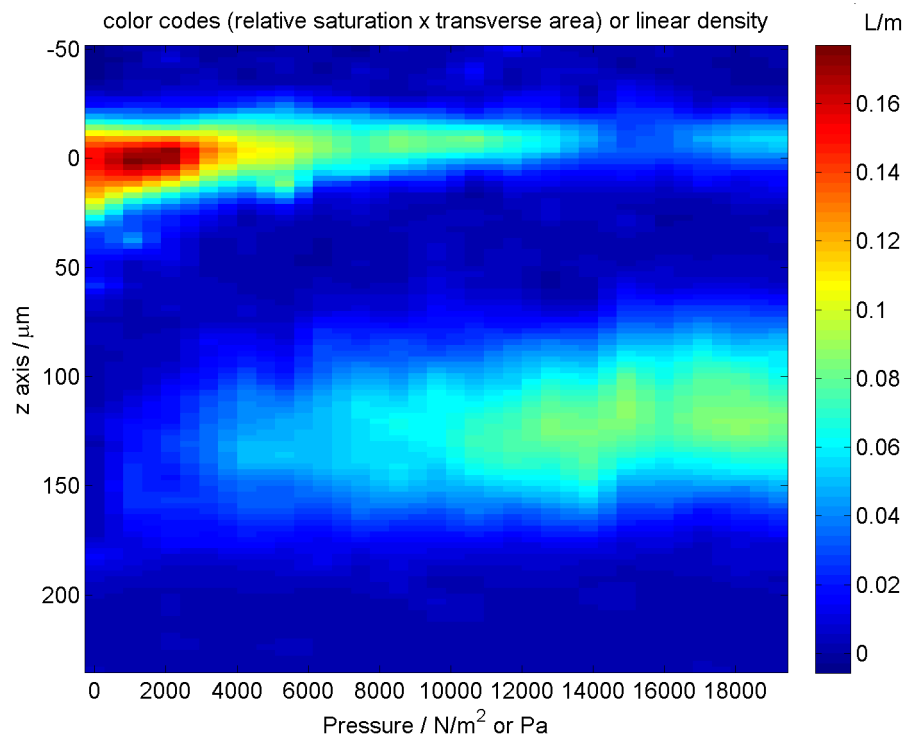
Fig.IV.9: Colour-coded linear oil density as a function of *z* (vertical axis) and applied pressure (horizontal axis) revealing the dynamics of the ingress of the liquid into the system. Note the absence of signal seen between approximately 30 and 100 μm, due to the repellent layer around this position. The origin of the *z* axis is made to coincide with the interface between the top of the system under investigation and the glass microscope slide.

The curvature of the selected slice dictates the effective spatial resolution (15 μm) of the profiles, rather than the digital spatial resolution (5 μm in this case). Each original pixel is therefore an integral of NMR signal collected over 5 μm which is obtained with

a sampling rate of 500 kHz, 400 digital points per echo and the strong intrinsic field gradient (11.38 T/m).

The full protocol for the same experiment was repeated three times to assess the repeatability of the measurements, thereby leading to four data sets shown in Fig.IV.10, together with the original experiment, for comparison purposes.
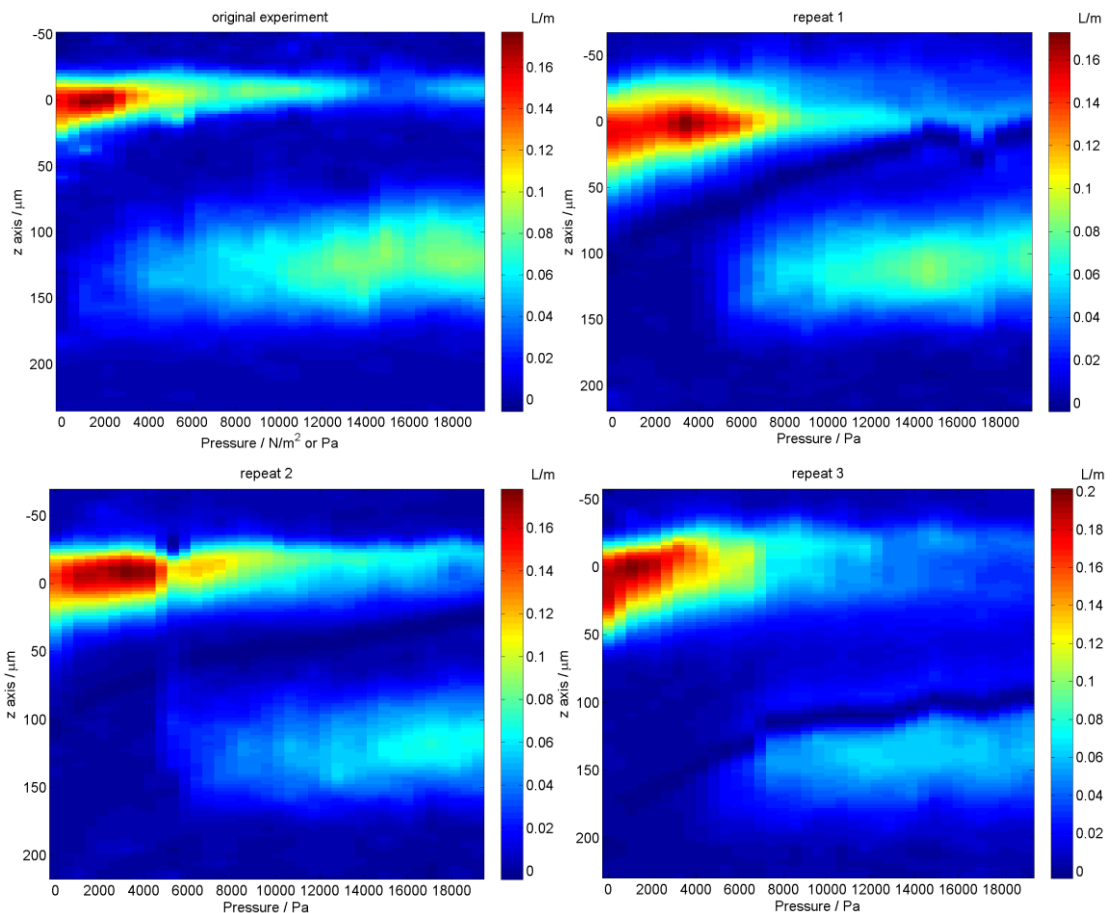
Fig.IV.10: Repeats for oil ingress. Colour-coded linear oil density as a function of z (vertical axis) and applied pressure (horizontal axis). The top left plot is the same as Fig.IV.9 and the 3 others are repeats done in similar conditions.

Further quantification (Fig.IV.11) of the data from Fig.IV.9 was done as follows: the signal was integrated for z between -55 and 53 μm (the falling curve, corresponding to oil residing between the microscope slide and the top repellent layer) and z between 53 and 214 μm (the increasing curve, corresponding to oil residing in the non-repellent layer) and z between -55 and 214 μm (upper curve, corresponding to oil residing in the total system under investigation). These z boundaries for the integrals were chosen visually, based on the data in Fig.IV.9.
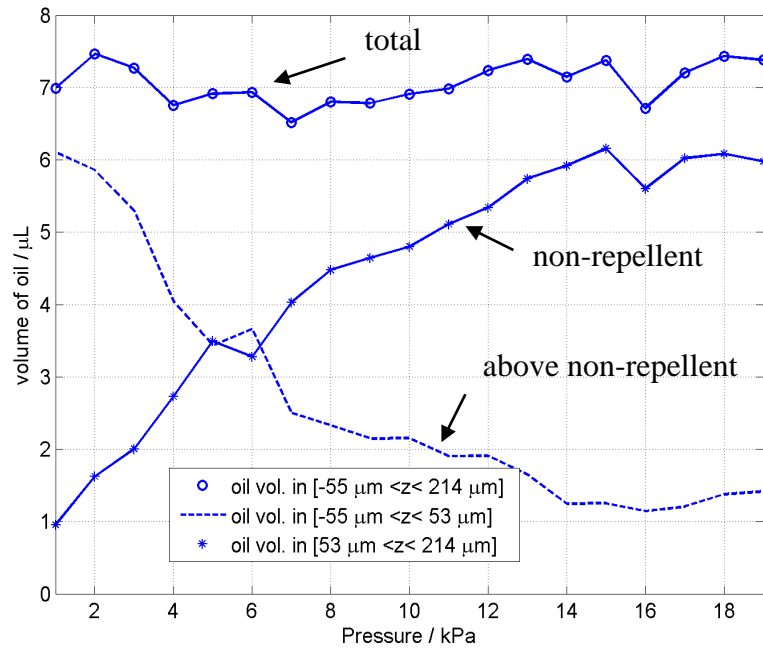
Fig.IV.11: Same data as in Fig.IV.9, but with each NMR profile integrated over a specific range of z values, to reveal the dynamics of the ingress in terms of the oil content in each individual layer.

These integrals reveal the dynamics of the volume of oil found in each layer, and further validates the quantification of the data, as the total amount of oil measured in the system can be confirmed as remaining constant. However, a maximum total signal loss of approximately 26% was sometimes observed due to excessive lateral spread (of the liquid) reaching an area out of the 2 cm^2 of the transverse volume as defined in section III.3.2.

IV.4.2.2. Oil ingress into activated carbon cloth

As a continuation of the above work, a different layer combination to make a different type of protective material was used. A carbon cloth was sandwiched between two repellent layers. The data processing was done with a similar technique to that used in the previous experiment but a bi-exponential decay needed to be fitted to the train of spin echoes, see Fig.IV.12, requiring the use of four fitted parameters: the amplitudes of both short and long T_2 and their respective T_2 values.
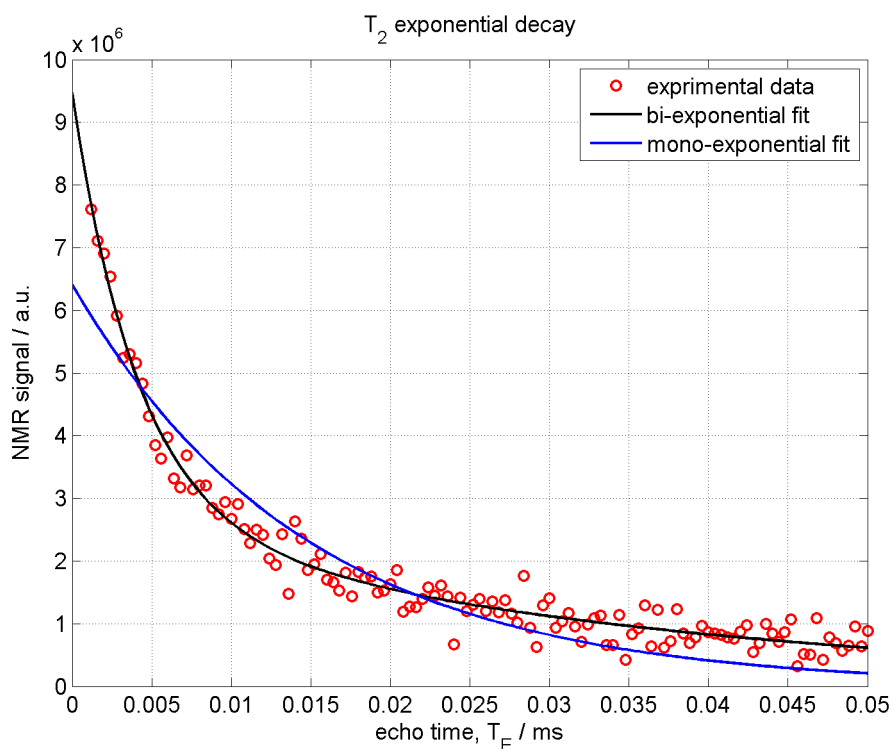
Fig.IV.12: T_2 fitting to experimental data (red dots). The mono-exponential decay is represented by the blue curve and the bi-exponential decay is represented by the black curve. The graph clearly demonstrates that a bi-exponential fit is required.

It is assumed that negligible adsorption was happening because the Duckhams oil is not volatile and therefore entirely ingresses into the pores in the liquid state. It was discussed in chapter II that T_2 can probe the size of the pores in non adsorbing porous media such as sandstones; the smaller the T_2 value, the smaller the pore in which the fluid resides. As a reminder, a molecule in a small pore will interact with the pore walls more than in a bigger pore. Therefore, the R_2 will be higher for molecules trapped in small pores. In this experiment, two separate values of R_2 from the NMR data were extracted and were interpreted as a distribution of two sizes of pores. Those values of R_2 (reciprocal of T_2) were obtained by processing the signal coming from all the pixels within the AC cloth, which provided T_2 values which were remarkably constant with the progress of the ingress, see Fig.IV.13.
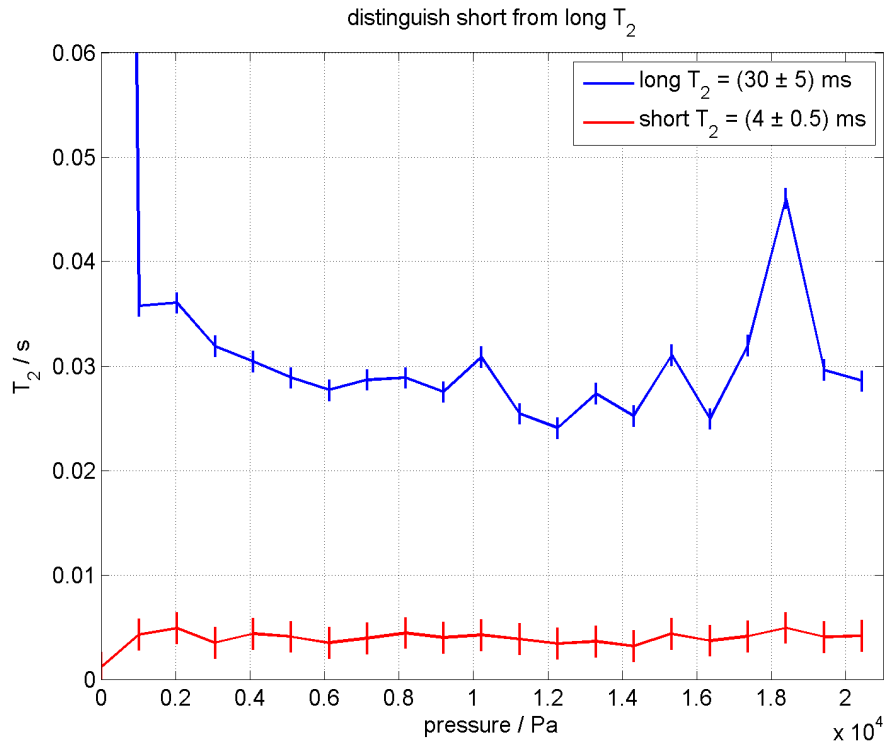
Fig.IV.13: Graph showing the values of both short (red lower curve) and long (blue upper curve) T_2 as the ingress is progressing. The short T_2 was calculated by averaging the values oscillating between 3 and 5 ms for the whole range of increasing pressure; its corresponding high R_2 is (250 ± 30) s^{-1}. The long T_2 was calculated by averaging the values oscillating between 20 and 50 ms for the whole range of increasing pressure; its corresponding low R_2 is (34 ± 5) s^{-1}.

A second piece of software was then written in which the values of T_2 were held constant and equal to the values extracted from the bulk signal (Fig.IV.13). Only the amplitude of both the short and the long T_2 were fitted. On Fig.IV.14, the correspondence between the sketched layered fabric (comprising the cloth) and the resulting plot can be seen.
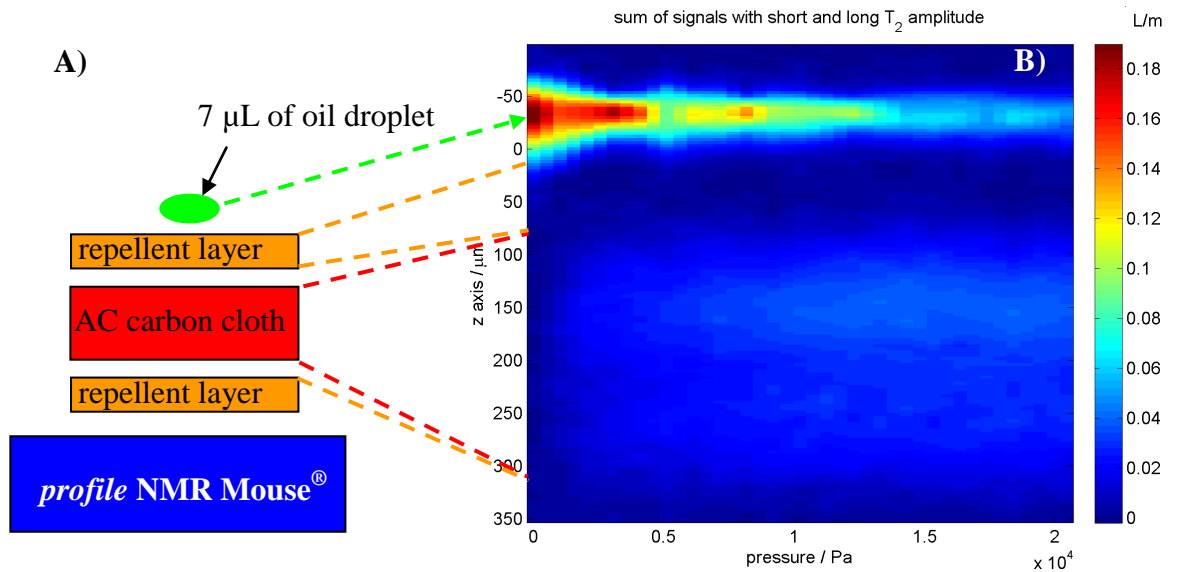
Fig.IV.14: A. Sketch of the experimental set up showing the sample under investigation above the NMR Mouse®. **B.** Colour-coded linear oil density (representing the sum of short and long T_2 amplitudes of Duckhams oil NMR signal) as a function of z (vertical axis) and applied pressure (horizontal axis) revealing the dynamics of the ingress of the liquid into the system. Note again the absence of signal within approximately 70 µm below $z = 0$, due to the repellent layer around this position. The bottom repellent layer is not represented in its totality as liquid never penetrated so far and thus only shows an absence of signal.

The plot on Fig.IV.14 **B** can also be decomposed in two separate figures processed with the amplitudes of the individual T_2 components, see Fig.IV.15.
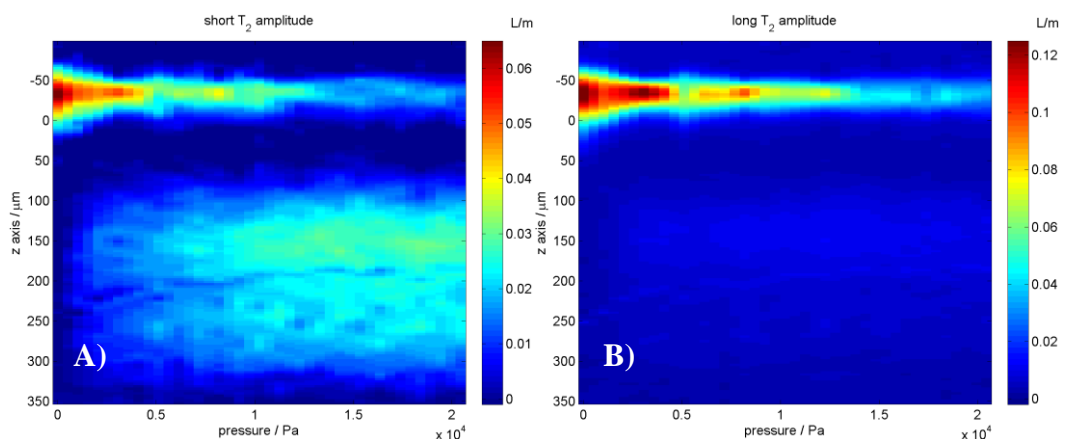
Fig.IV.15: Plots representing respectively the colour-coded amplitude of the short T_2 of linear oil density **(A)** and the long T_2 of linear oil density **(B)** as a function of z (vertical axis) and applied pressure (horizontal axis) revealing the separate dynamics of the ingress of the liquid into the system.

In order to be able to reach the cloth, transport of oil has to occur through the micro-channels of the first repellent layer (just as seen for the ingress of oil in the layered

fabric, see preceding section IV.4.2.1.). So as to enhance the colour-coding of the signal residing within the AC cloth, Fig.IV.16 includes only the results of the field of view encompassing the AC cloth. The origin of the z axis was shifted downwards by 175 µm so that it sits well within the AC cloth.
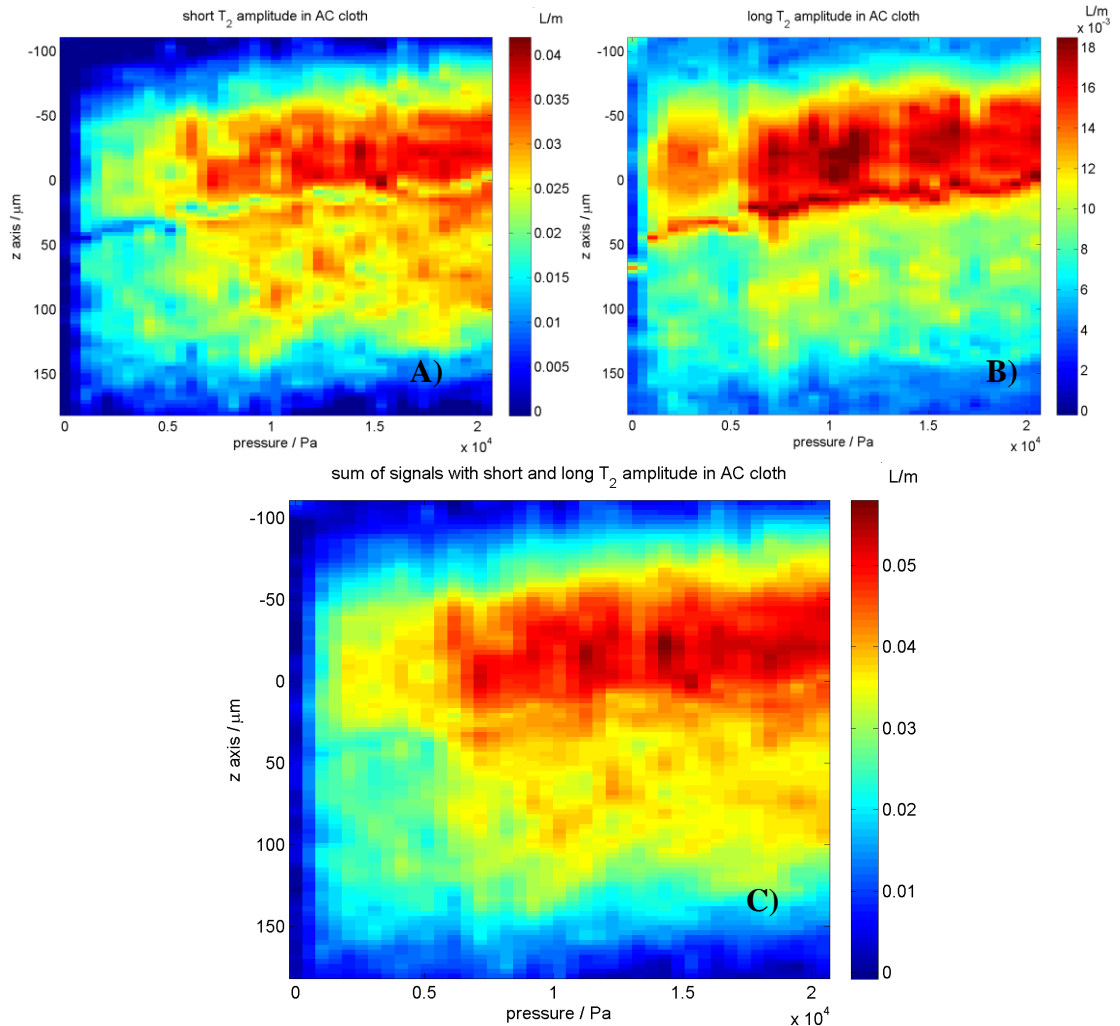
Fig.IV.16: Plots representing respectively the colour-coded amplitude of the short T_2 of linear oil density **(A)**, the long T_2 of linear oil density **(B)** and the sum of both the short and long T_2 of linear oil density **(C)** as a function of z (vertical axis) and applied pressure (horizontal axis) revealing the separate dynamics of the ingress of the liquid into the AC cloth.

On Fig.IV.16, the vertical axis of the three plots represents the vertical axis above the NMR Mouse®. A total thickness of about 275 µm is shown so that data from 50 and 25 µm respectively above and below the cloth are evident. Some signal is found beyond the 200 µm-thick cloth due to the moderate warping of the selected slice as already mentioned in the previous section IV.1.

The horizontal axis corresponds to the temporary pressure in Pascal (Pa) applied on top of the droplet. To start with, no signal is seen in the cloth. As increasing pressure is applied on top of the system, the droplet of oil progressively invades the AC cloth and stays into it. Note that the first half upper part (from -70 μm until 30 μm) of the AC cloth is seen to retain most of the oil (66%) as can be seen on **A**, **B** and **C** in Fig.IV.16. Likewise, the amplitude of the short T_2 is stronger by a factor 2 compared to that of the long T_2.

The full protocol for the same experiment was repeated three times to assess the repeatability of the measurements, thereby leading to four data sets shown in Fig.IV.17, Fig.IV.18 and Fig.IV.19, together with the original experiment, for comparison purposes.
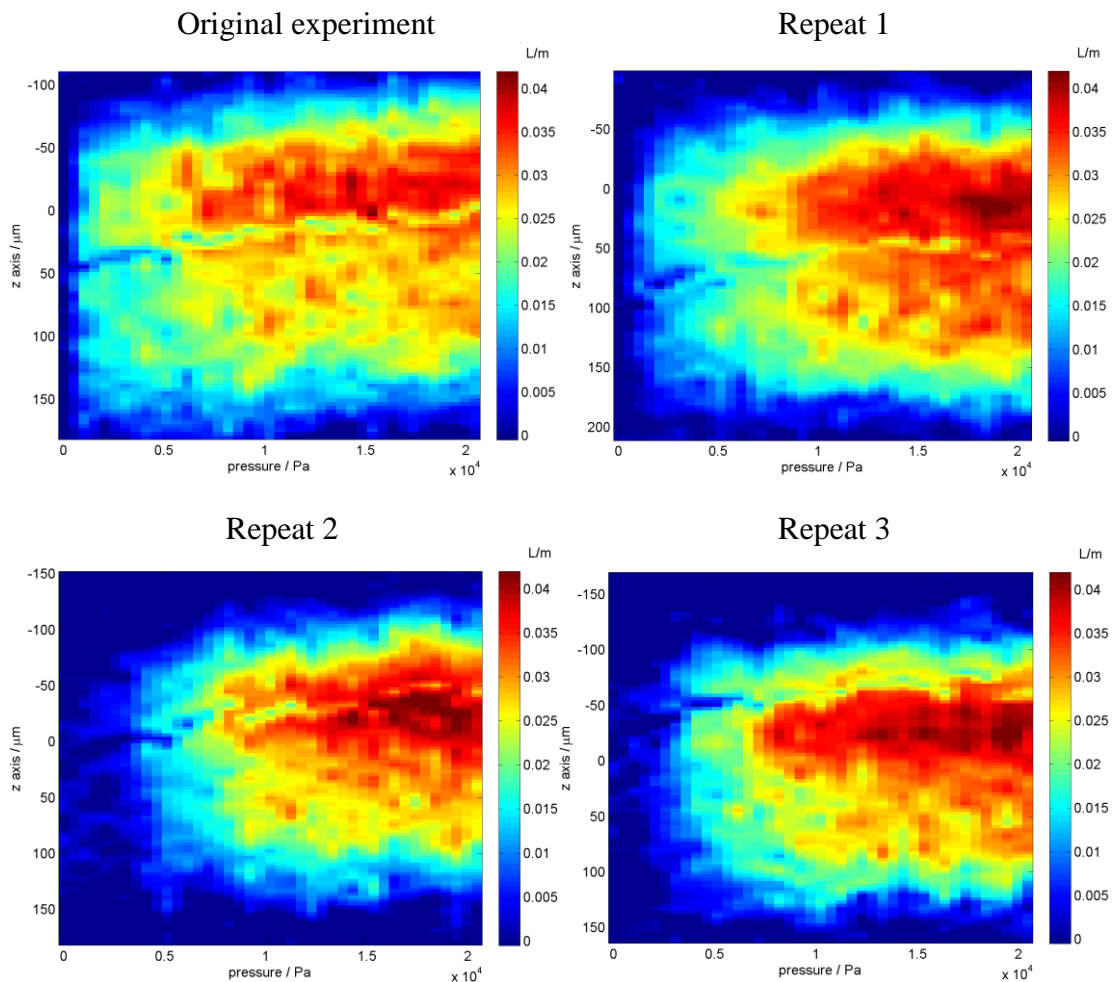
Fig.IV.17: Repeats for oil ingress in AC cloth. Colour-coded amplitude of the short T_2 (converted into linear oil density) as a function of z (vertical axis) and applied pressure (horizontal axis) revealing the dynamics of the ingress of the liquid. The top left plot is the same as Fig.IV.16 **A** and the 3 others are repeats done in similar conditions.
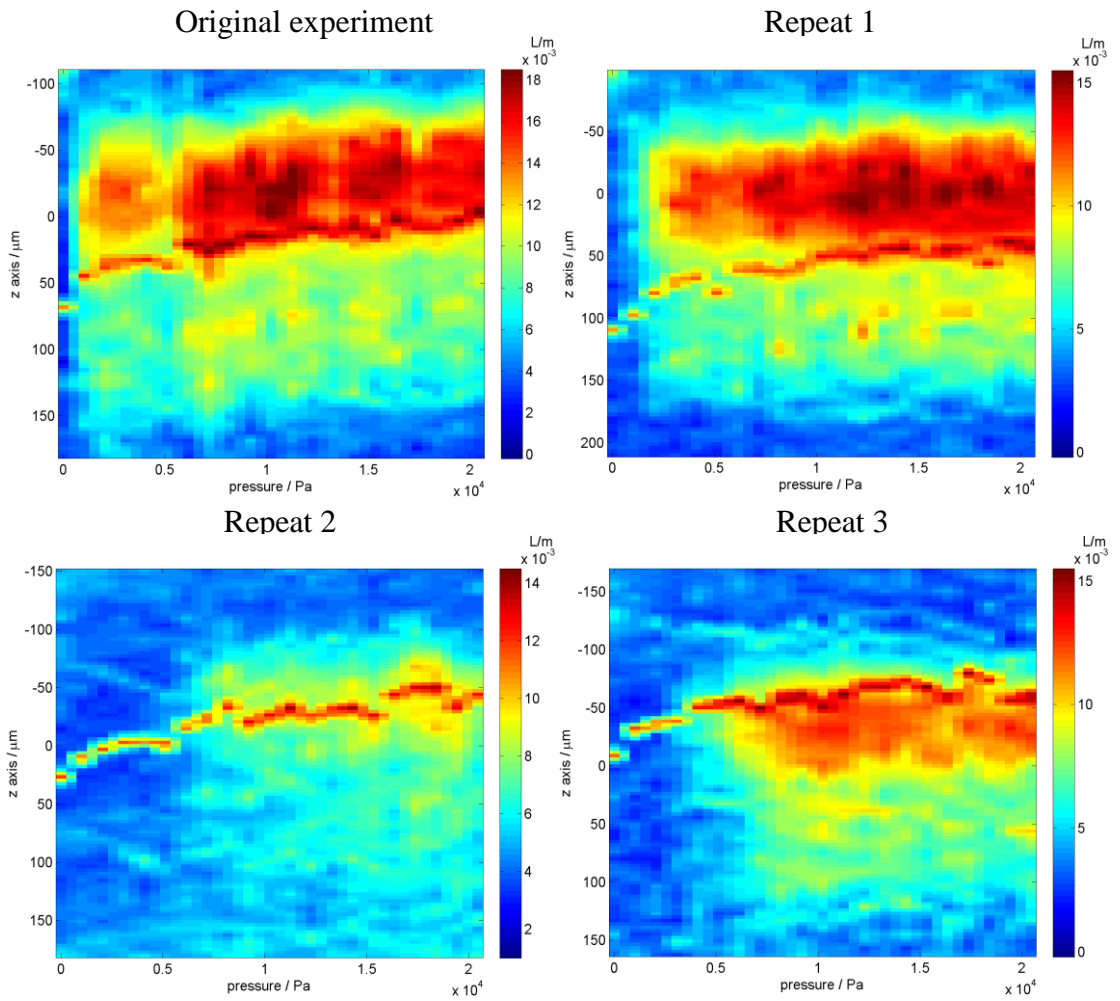
Fig.IV.18: Repeats for oil ingress in AC cloth. Colour-coded amplitude of the long T_2 (converted into linear oil density) as a function of z (vertical axis) and applied pressure (horizontal axis) revealing the dynamics of the ingress of the liquid. The top left plot is the same as Fig.IV.16 **B** and the 3 others are repeats done in similar conditions. The zero-frequency component (defined in section III.3.4.) is quite pronounced for these experiments. It can be seen particularly well for the amplitude of the long T_2. The (low) intensity of the amplitude (of the long T_2) is almost the same as the (high) intensity of the amplitude of the zero-frequency component.
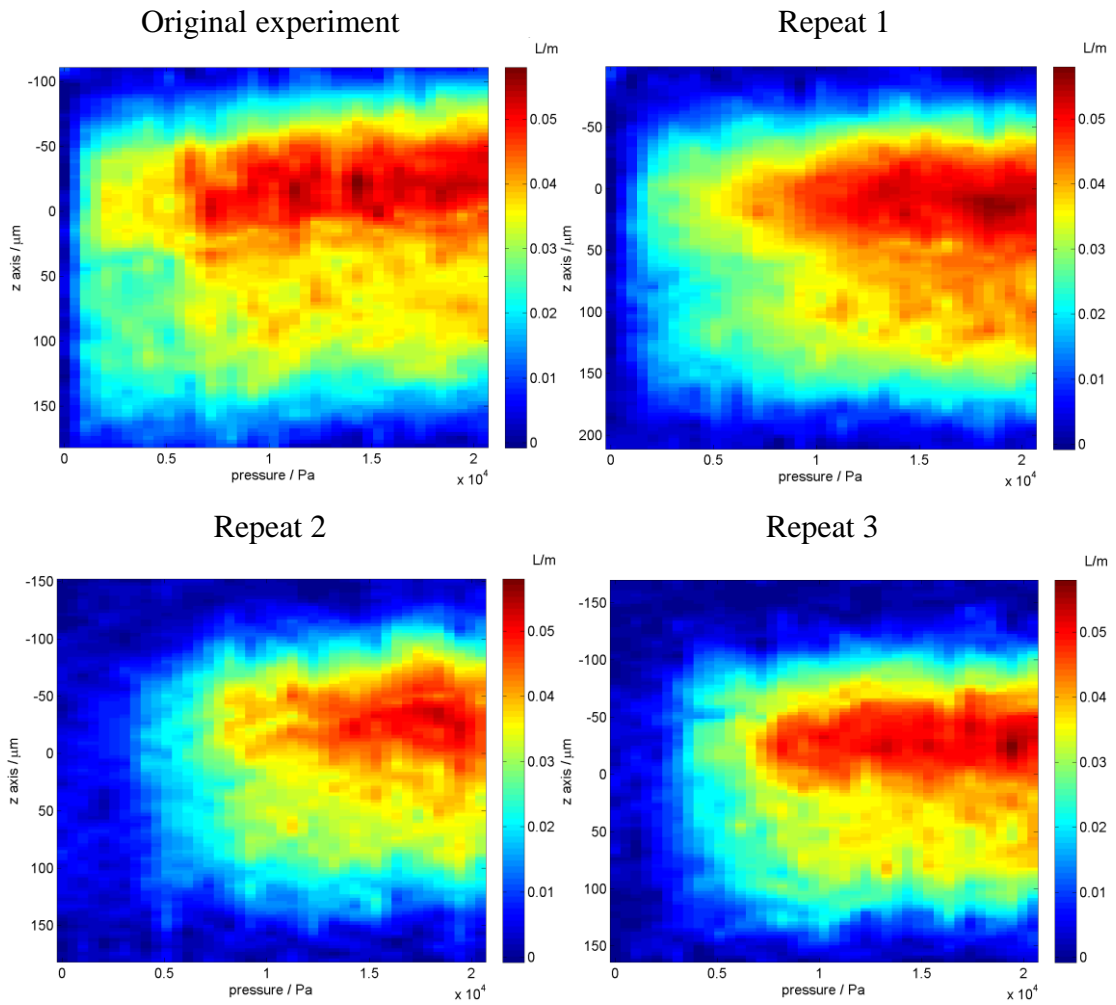
Fig.IV.19: Repeats for oil ingress in AC cloth. Colour-coded amplitude of total NMR signal (converted into linear oil density) as a function of *z* (vertical axis) and applied pressure (horizontal axis) revealing the dynamics of the ingress of the liquid. The top left plot is the same as Fig.IV.16 **C** and the 3 others are repeats done in similar conditions.

Furthermore, the amplitudes of the short and long T_2 can be integrated between -70 μm and 130 μm, to show the respective fluid dynamics with regards to the applied pressure they are experiencing, see Fig.IV.20.
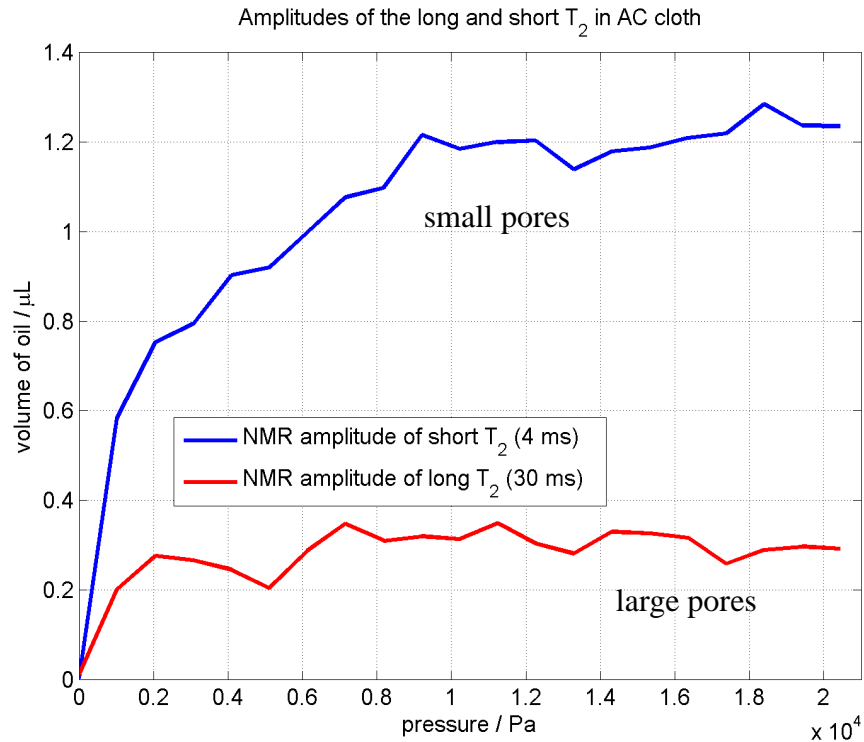
Fig.IV.20: Same experimental data as in Fig.IV.16 **C**, with each NMR profile integrated over z values from -70 μm until 130 μm, to show the fluid dynamics of both the short and the long T_2 in the AC cloth layer.

The amplitude of the short T_2 (blue upper curve, representing the smaller pores being filled) is reaching a plateau after an applied pressure of 8 kPa whilst the amplitude of the long T_2 (red lower curve, representing the bigger pores being filled) is doing so after 2 kPa of applied pressure.

IV.4.3. Discussion

IV.4.3.1. Oil ingress into layered fabric

The details of the ingress of oil are clearly displayed in Fig.IV.9. At first, by increasing the temporary pressure until 1300 Pascal, the whole layered system is being squeezed resulting most probably in a thinner slice (between the microscope slide and the top repellent layer) in which the oil is allowed to reside. This can be seen in Fig.IV.9 by the apparent increase in signal within the four first profiles at $z = 0$. Some oil even rests within the solid asperities of the top repellent layer as may be seen from relatively low

signal for z values between 10 μm and 20 μm. The oil penetrates the second non-repellent layer even for the lightest load; this is seen for all repeats. Since no signal can be observed in the first 70 μm, the ingress process must be exploiting microchannels linking the first layer to the second. A steady state is reached for pressures higher than 14×10^3 N/m^2, and by then, most of the oil (6 ± 0.5) μL has ingressed into the second layer. If further pressure were to be applied vertically, it would probably cause no further vertical ingress, since the sandwiched layer is non-repellent and encourages transverse flow. When a non-repellent layer (followed by a repellent layer) is used on the top of the stack, vertical ingress to the second layer has not been seen at all (even for twice more load than the highest load explored) and in this case the integrity of the oil remains in the top non-repellent layer. This three layered structure is therefore a very effective barrier to vertical flow. Ingress across the third layer of the structure presented in Fig.IV.9 has never been observed either (both visually or by NMR), over the range of loads that has been explored. In Fig.IV.9, the colour can also be interpreted as the product of the local porous medium saturation by the transverse (x, y) saturated surface. Transverse field gradients could be used to spatially resolve the signal from a layer and so provide information on the dynamics of liquid saturation occurring within each layer. Fig.IV.11 also demonstrates that the signal coming from all of the oil in the fabric has been successfully monitored quantitatively. However, a loss of signal was sometimes seen resulting from a loss of volume, as mentioned earlier, suggesting that the oil eventually spreads transversally (out of the sensitive volume) to locations where the drop in B_1 field homogeneity is too poor for quantitative assessment of oil density, and where it is thus difficult to detect NMR signal.

Finally, small variations are seen on Fig.IV.10 from one experiment to another and these are most likely to be due to genuine experimental set up variations rather than from the NMR monitoring technique. The threshold at which a particular amount of oil is seen to ingress varies; it can be triggered at a low pressure (400 Pa) or at higher pressures like 4000 or 5000 Pa. Also, the thickness and/or the coating of the textile layers present some slight inhomogeneities from one location to another in the same plane, therefore some liquid can penetrate deeper in the asperities of the top layer. Eventually, the absolute signal of the oil in the entire fabric might show some dissimilarities at a given pressure for different experiments due to fluctuations in the

potential success of channels creating links between each another so that ingress of oil can progress.

IV.4.3.2. Oil ingress into activated carbon cloth

The results where the inner non-repellent layer is replaced with the AC cloth layer suggests a way of resolving the dynamics of the separate ingress in smaller pores and bigger pores in AC cloth by a T_2 measurement, see Fig.IV.16. The amplitude of the short T_2 is stronger typically by almost a factor 2 than the amplitude of the long T_2. Therefore, when the two respective amplitude maps are being superimposed, the amplitude of the short T_2 is a close representation of the final result. This sggests that twice more porosity is available in the small pore pool than in the large pore pool.

Another result drawn with this type of cloth, is that the bigger pores are being filled first (for a pressure of 2 kPa) and that the smaller pores are being filled at later stages (for a pressure of 8 kPa), see Fig.IV.20. The high viscosity of Duckhams oil compared to the low viscosity of some organic compounds (*e.g.* heptane, nonane …) makes it difficult for the oil to move into small cavities. This might explain why the bigger pores are filled first. However, under higher applied pressures, the oil succeeds to move into the smaller pores.

Finally, small variations are seen on Fig.IV.17, Fig.IV.18 and Fig.IV.19, from one experiment to another and these are most likely to be due to genuine experimental set up variations rather than from the NMR monitoring technique. In addition, systematic differences are seen in the spatial distribution of the oil seen in large pores and that seen in small pores. Indeed the oil residing in the bigger and smaller pores is more present in the upper part (100 μm) of the AC cloth, although it seems that the oil residing in the smaller pores is more homogeneously spread over the entire AC cloth than that sitting in the bigger pores.

IV.5. Spontaneous oil ingress into layered fabric

IV.5.1. Results

The time-course of the results from an overnight experiment are shown in Fig.IV.21, in the same way as in Fig.IV.9, but with a horizontal axis that shows the time at which the profile was acquired.
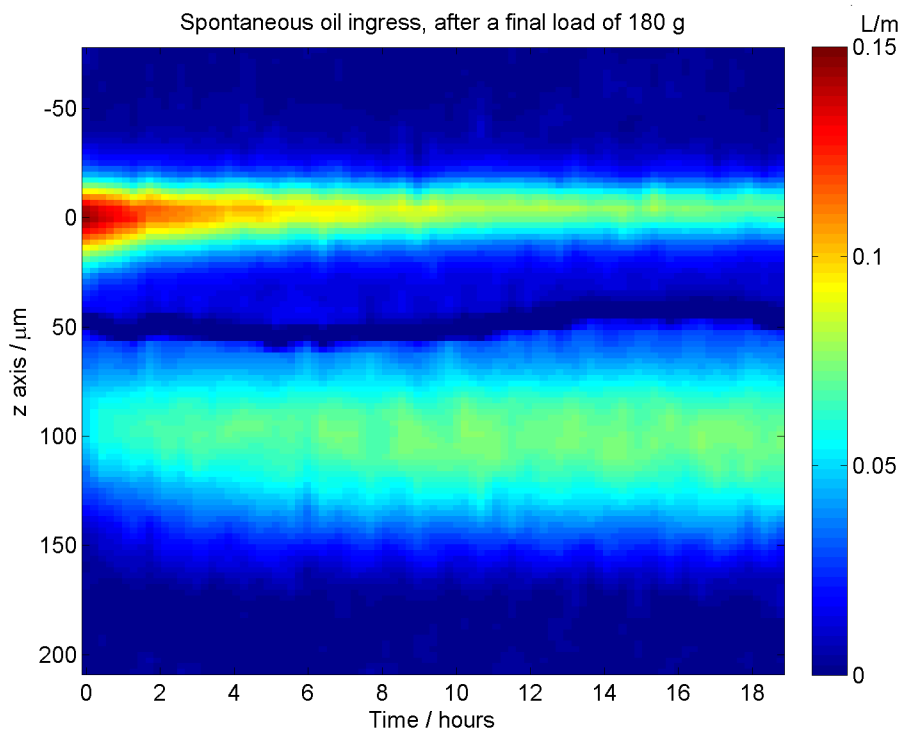
Fig.IV.21: Colour-coded linear oil density as a function of *z* (vertical axis) and time (horizontal axis) for an over-night experiment.

The final temporary load (180 g) which was applied on top of the system in order to trigger the breakthrough for liquid crossing the top repellent layer was found after the third attempt.

Although this experiment demonstrates interesting features of the long term oil ingress into a fabric occurring after breakthrough has succeeded, it was not repeated nor further explored, as the focus of the studies here was the monitoring of the spatial distribution of the oil *immediately* following breakthrough.

IV.5.2. Discussion

The first profile demonstrates that some oil has passed the barrier of the repellent layer. Slow ingress from the top layer to the middle one, due to both gravity and capillary action, is clearly seen in the profiles acquired at later times. This suggests that the continuity of the fluid between the two layers has been retained, at least at a few transverse locations, when only 40 g of vertical load is present in the system. The usual lack of signal is also seen between the two layers, suggesting again that this continuity is fulfilled with a very small, not measurable, volume of oil. The post-acquisition quantification method used and demonstrated in Fig.IV.11 did not yield a constant signal for the overnight experiment. Instead, a total signal loss of approximately 15% was seen, suggesting that in these lengthy experiments the oil eventually spreads transversally to locations where the drop in B_1 field homogeneity is too poor for quantitative assessment of oil density.

IV.6. Conclusion

This work demonstrates a promising method to quantitatively and non-invasively explore the dynamics of liquid ingress into a complex layered liquid-repellent fabric. It has been shown that a low-field unilateral NMR instrument can provide an excellent match between the geometry of the system of interest and the features of the measuring device, thus allowing a suitable choice of spatial and temporal resolution and overcoming the usual limitation of MRI. This match of geometries also allows exploitation of the Fourier Transformed NMR signal (1D MRI), rather than physically moving the instrument relative to the sample as is usually done. The approach has been extended to a more complex (differently constructed) fabric where an AC cloth layer is inserted instead of a non repellent layer. The vertical profiles of oil ingress into this fabric were successfully obtained using a simple NMR instrument. These measurements are also quantitative in favourable conditions and therefore variations in the spatial resolution can be observed. Indeed, it is seen that most of the oil remains in the upper half of the carbon textile. From the T_2 measurement pore size distinction is suggested and the corresponding dynamics of oil ingress can thus be assessed. The data suggest that the bigger pores are filled before the smaller pores.

CHAPTER V: MONITORING VAPOUR ADSORPTION/DESORPTION AND SATURATION IN ACTIVATED CARBON SAMPLES WITH NMR

INTRODUCTION

Four different AC samples (manufactured by MAST Carbon International ltd, based in Guildford, UK) were provided by the DSTL:

- AC monolith,
- AC composite,
- and two types of AC cloth.

The two different AC cloth samples were named CF2 (see Fig.IV.6 **(A)**) and JP2 (see Fig.IV.6 **(C)**). For information, CF2 and JP2 have no specific meaning, they are just sample codes used by the DSTL. The cloth JP2 is suggested for a pilot study presented in future work (see section VI.2.7.) and its characteristics have therefore not been explored. Throughout the main body of this chapter, only the AC cloth CF2 is used and is thus simply called AC cloth, as was done in chapter III.

This chapter starts with a section dedicated to the presentation of the AC samples followed by the presentation of the experimental set up for different NMR and non-NMR experiments that were undertaken. The results are then exposed and discussed.

V.1. Experimental protocol

V.1.1. Three different activated carbon samples with different geometrical structures and microporosities

Before proceeding to the presentation of the three different AC samples (monolith, composite and cloth), a few definitions needs to be given.

- A binder is a chemical or an ingredient used to bind together two or more substances in mixtures.
- Mesophase (also known as the liquid crystal phase) is a state of matter between the crystalline solid and isotropic liquid phases.

- A self-sintering material is a material that starts to diffuse by heat.

- Pyrolysis is a thermochemical decomposition of organic material at elevated temperatures in the absence of oxygen.

- The soak time is the time for a tracer gas to penetrate inside the walls of the material in preparation.

- A ball mill is a type of grinder used to crush materials into extremely fine powder.

- Pitch is a residue from pyrolysis of organic material.

- Aromatic hydrocarbon is a hydrocarbon with a conjugated cyclic molecular structure.

- Mesophase pitch is a pitch with a complex mixture of numerous essentially aromatic hydrocarbons containing anisotropic liquid-crystalline particles.

V.1.1.1. Activated carbon monolith

AC Monolith is a binderless material which can be prepared from a self-sintering mesophase-based (pitch) precursor [93]. The process of preparing an AC monolith is long [83]: a petroleum residue (ethylene-tar) is pyrolyzed in a laboratory pilot plant at 440 °C and at a pressure of 1.0 MPa, using a heating rate of 10 °C/minute and a soak time of 4 hours to yield mesophase pitch (MP). Detailed description of the procedure is described in ref [93]. The synthesis of the AC monolith involves several steps [83]:

1. Mixture of the MP with KOH in different proportions in a ball mill during 30 minutes.

2. Extrusion: the carbon precursors and the activating agents are extruded through a die to produce a 3D structure. This is conducted at a pressure of 400 MPa and due to the plasticity of the mixture a permanent structure can be produced which can subsequently survive the carbonisation process. This process is used to produce the monoliths (22 mm in diameter) that possess millimetric channels down the length of the monolith.

3. Heat treatment at 800 °C under nitrogen atmosphere, heating rate of 2 °C/minute and soak time of 2 hours.

4. Washing of monoliths with a solution of 1 molar HCL, followed by extensive washing with distilled water until the solution in the monolith reaches pH 7. The final step consists in drying the monolith at 100-110 ºC for 24 hours.

2.2 cm
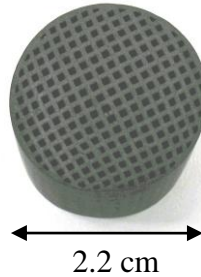
Fig.V.1: Photograph of a monolith. The apparent channels have a square section with a size of 1 mm.

V.1.1.2. Activated carbon composite

AC composite materials are defined as a multicomponent material that contains carbon nanofibres dispersed within a continuous phase composed of a suitable matrix such as polyetherimide [94], $(C_{37}H_{24}O_6N_2)_n$. As an example of using rice husk as a precursor for AC composite, during heat treatment the cellulose component gets converted into carbon, while the pores are created as a result of the release of volatile decomposition products [80]. Carbon fibre (fibres consisting of at least 92 percent weight carbon [30]) and phenolic resin can be used to fabricate cylindrical shaped composites. Carbon fibre, phenolic resin and water at a predetermined ratio are introduced into a vacuum moulding unit and as the water is withdrawn using a vacuum, the mixture takes the shape of the mould [95].

Fig.V.2: Photograph of an AC composite cylindrical sample. The actual height of this cylinder is 7 cm and its diameter is 2.4 cm.

V.1.1.3. Activated carbon cloth

AC cloth, see Fig.IV.6 **(A)**, can be prepared from cellulose-based fabrics by H_3PO_4 activation which is a chemical activation but it can also be synthesized by physical activation. The cellulose precursor is a polymer generally coming from cellulose itself, regenerated cellulose (mainly, viscous rayon which is a manufactured regenerated cellulose fibre), polyacrylonitrile, C_3H_3N, and phenolic fabrics. The precursor is soaked in H_3PO_4 at 100 ºC for 30 minutes. The impregnated dried H_3PO_4 samples are thermally treated in a tubular stainless steel reactor of horizontal configuration under a nitrogen (N_2) flow (100 mL/minute). It is externally heated by an electric furnace with a programmable temperature controller, which provides control of the heating rate, temperature, and heating time. The temperature is raised at a rate of 5 ºC/minute up to a final thermal treatment temperature of 800 ºC which is maintained for 1 hour. The N_2 flow is kept throughout the thermal treatment and further cooling of the samples up to room temperature. Afterwards, the resulting cloths are rinsed thoroughly with distilled hot water until neutral pH, in order to remove the acid. They are subsequently dried, periodically weighted until constant weight, and stored in sealed bags [81].

Scanning Electron Microscopy (SEM) images were produced on the AC cloth with Dr Belton's assistance. The results are displayed in Fig.V.3. SEM images of the two other types of AC were not produced because the pore structure of the material is below the spatial resolution of the instrument.
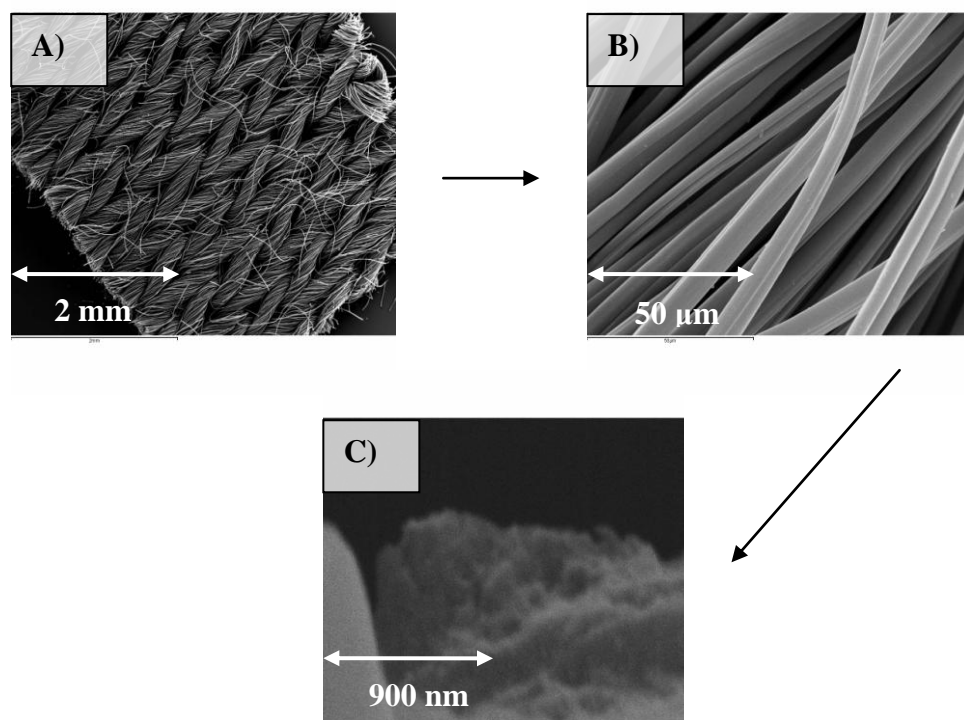
Fig.V.3: SEM images realized on AC cloth. **A.** It is clearly seen that the cloth is woven. **B.** Each fibre is approximately 10 μm thick. **C.** On a broken end fibre, larger pores can be seen.

With the SEM images details of the woven material can be seen. At a broken end of a fibre large pores of around 200 nm can be seen; but it is difficult to conclude whether those pores are genuine or if they appeared whilst the fibre broke. The SEM equipment's spatial resolution (100 nm for this sample) limits the ability to distinguish mesopores.

V.1.2. Gravimetric experiments

A very thin (0.5 mm) slice was cut out from a monolith without its outer rim and its weight was monitored every 15 min with a mass balance (KERN ALJ 160-4NM) during a heptane uptake process that was also monitored with the NMR Mouse®, for a total experimental time duration of seven hours. The monolith was exposed to a continuous feed of heptane by using a liquid pool of 1.5 mL continuously producing

heptane vapour. The sensitive volume of the NMR Mouse® encompassed the entire volume of the sample.

Two similar gravimetric measurements were also done for the cases of nonane vapour and water vapour, on two different square sections of AC cloth. The cloth sat between two repellent layers within an air tight vessel in order to reproduce the same experimental conditions as for an NMR experiment. A thin flat round Perspex disc flattened the fabric. All three sections were made of a similar size of 2.4 cm x 2.4 cm. The two different cloths (one undergoing a nonane vapour experiment and the other undergoing a water vapour experiment) were of a similar size and weight. The Perspex (5 cm in diameter, 3 mm thick and of a weight of 6.61 g) had a bore in its middle of 6 mm in diameter allowing 7 µL of liquid to be deposited through it. The droplet was thus resting on the repellent top of the system. By means of evaporation the molecules reached the cloth. The two separate experiments were prepared and run simultaneously in two different vessels.

V.1.3. NMR experiments

Numerous adsorption/desorption experiments were undertaken using several VOCs and water vapour on the different ACs. The first experiments were run with the selected slice deep (3 or 4 mm) into the monolith. The monolith sat onto a PTFE well in which a pool of heptane was placed. Vapours of heptane reached the bottom of the monolith and then further progressed upwards into it. The vapour uptake was monitored with the NMR Mouse® which was turned upside down together with the lift holder, see Fig.V.4.
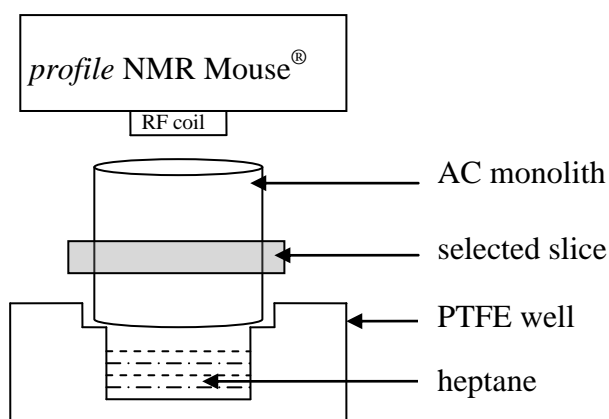
Fig.V.4: Uptake of heptane in an AC monolith. The NMR Mouse® including its lift was rotated by 180°. A pool of liquid heptane sits in a PTFE reservoir. The heptane can evaporate from the well and invade the monolith. PTFE was chosen because it is both easy to shape and hydrogen free.

Later experiments were run on a very thin monolith with the selected slice at its extremity. The motivation for going for a thin disc was to minimize signal loss seen in this highly conductive sample and also to make the relative volume of sample under NMR investigation larger. Note that with the set up shown on Fig.V.4, the rate of evaporation is poorly controlled, leading to variable results. Therefore a gravimetric experiment of the monolith (see section V.1.2.) was designed in order to corroborate the NMR results.

It is important to free the AC samples from any molecules (*i.e.* degassing it) before running an uptake experiment. This *reactivation* enables to evacuate the totality of the pores and thus to reactivate its surface area. It was found that this can be done by placing the AC sample in a vacuum oven at 160 °C for 4 to 5 hours (and this also releases oxygen molecules).

V.1.3.1. Protocol for adsorption of water and heptane in activated carbon monolith

The experimental protocol was the same as for "Removing outer rim of activated carbon monolith", see section III.2.3. However the preparation of the experimental set up for the water uptake differed a little from that of the heptane uptake.

Similar sections of monolith samples (6 mm for heptane and 0.5 mm for water) were used for both experiments and were placed in a capped petri dish next to respectively three identical reservoirs for heptane and one for water, each filled with 1.5 mL of adsorptive and with a small aperture of 1 mm in diameter allowing a small rate of evaporation. The system was placed onto the NMR Mouse®. For the heptane uptake experiment, the selected slice was made to coincide with the bottom boundary of the activated carbon sample in order to minimise signal loss due to induced currents. For the water uptake experiment, the selected slice was set so that the entire activated carbon sample was encompassed. Fig.III.2 illustrates well the experimental set up, however Fig.III.3 shows a better representation of the source of adsorptive. At the end of the two separate measurements the reservoirs were not totally emptied, demonstrating that vapour "challenge" was kept fairly constant all along the experiment.

The NMR data were collected with the CPMG sequence with the settings described in section III.2.3. To monitor the adsorption and desorption, the FA and transverse relaxation rate (R_2) are extracted by fitting an exponential decay function to each digital point of the Fourier transformed spin echo. The FA represents the absolute amount of adsorbate trapped in the pores of the monolith. The relaxation rate represents the extent to which the molecules of the adsorbate under investigation are interacting with the walls of the monolith.

V.1.3.2. Protocol for T_2 measurement during water and nonane uptake in activated carbon cloth

In the second set of experiments, two different vapours (water and nonane) were supplied to a textile cloth which was sandwiched between two repellent layers. The adsorption was monitored with the NMR Mouse® by the use of the CPMG sequence with the following settings: $T_E = 120$ μs, 256 echoes, $T_R = 800$ ms, acquisition time = 80 μs and each experiment was averaged for 10 minutes. Seven micro litres of adsorptive (either water either nonane) were deposited on top of the repellent layer inside a 6 mm bore of a 6 mm thick Perspex spacer used to squeeze the layers together. The Perspex load, with a mass of 9.6 g, had an octagonal shape. Finally a sandstone

load (2.5 cm in diameter, 1 cm thick, with a mass of 13.5 g) covering the Perspex was used to further flatten the layered system without interfering with the evaporating water or nonane vapour. The entire set up was placed inside an air tight glass vessel. The top lid of the vessel had two incorporated pipes which had been closed with blue tack. The vapour slowly invaded the cloth after having crossed the top repellent layer, see Fig.V.5.
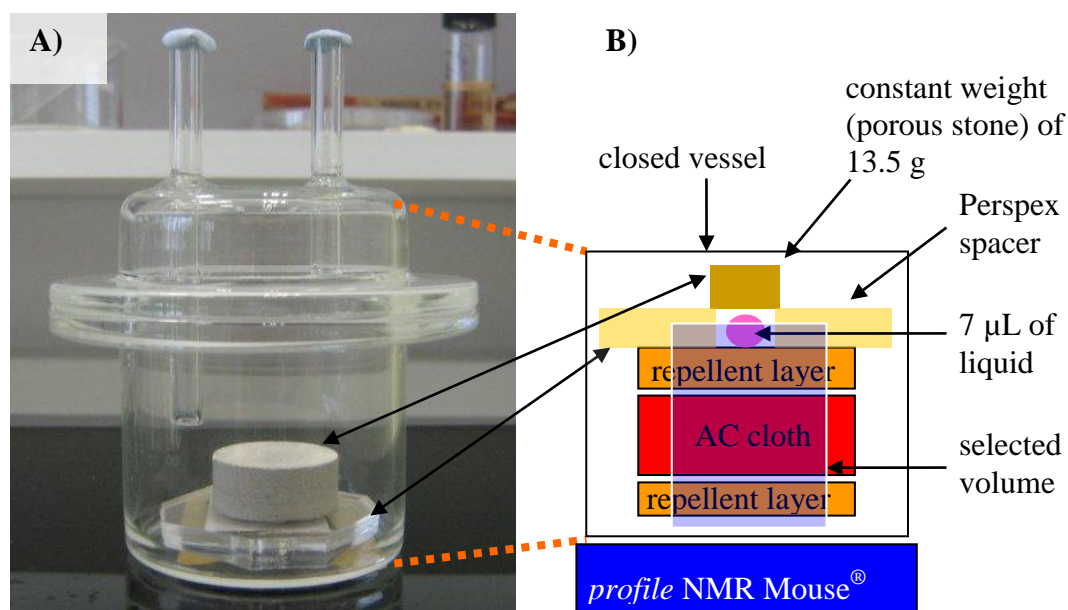
Fig.V.5: A. Photograph of experimental set up. The layered fabric was placed into an air tight vessel; a Perspex spacer with a sandstone load was put onto the fabric to squeeze the layered system together. **B.** Schematic of experimental set up.

V.1.3.3. Protocol for T_1 measurement of water vapour uptake in activated carbon cloth

The set up was the same as for water and nonane vapour uptake presented in the section V.1.3.2. For simplicity the investigation was started with water instead of nonane because it was known that water will exhibit a clear NMR signal. In addition 14 μL of liquid were used in preference to 7 μL so that even more NMR signal could be collected.

The saturation recovery sequence was used by varying the repetition time from 10 until 130 ms in steps of 30 ms. The CPMG sequence was used to collect the NMR data for a specific T_R value. The settings were: T_E = 120 μs, 32 echoes, acquisition time = 50 μs

and each experiment was averaged for 10 minutes. All the T_1 fittings were done with three parameters search (NMR amplitude, T_1 value and the thermal noise).

V.1.3.4. Protocol for dodecane uptake in a fabric made of activated carbon cloth protected between two repellent layer

The experimental set up was similar to the one described in section V.1.3.2. The Perspex was of a different design: it was made of a square sheet (4 cm x 4 cm) with a mass of 11 g. A small, 3 mm (instead of 6 mm) bore was drilled in its middle, in order to minimise warping of the top repellent layer at the location of the bore. A drop of 7 μL of dodecane was deposited on the top of the repellent fabric inside the Perspex bore. Dodecane was used because it possesses a lower volatility than water, heptane and nonane. The volatility is related to a liquid's boiling point, see Table V.1, which is the temperature at which a substance changes its state from liquid to gas at a specific pressure.

Element	Boiling point in °C
heptane	98.5
water	100
nonane	151
dodecane	216
Duckhams oil	260-370

Table V.1: Boiling points for five different elements under standard atmospheric conditions [96]. The lower the value of the boiling point, the easier the element evaporates at room temperature. Note that the evaporation process is actually more complicated and a few other parameters need to be taken into account for a full description. For instance, heptane evaporates much faster than water because air is already charged in water vapour. In addition, the boiling point of this particular Duckhams oil was not found; nevertheless it is a mineral oil (for diesel engine motorcars) which belongs to the polyalkenes.

As the volatility of dodecane is less than nonane, heptane and water, saturation of the cloth through vapour adsorption will be slower for dodecane than the other chemicals.

The NMR experiment was set up so that the sensitive volume integrated the entire layered sample. The NMR signal was monitored for 16 hours and averaged over 20

minutes. The CPMG sequence was used with the following settings: $T_E = 120$ µs, 512 echoes were collected, $T_R = 800$ ms, acquisition time = 50 µs.

The NMR data were processed by fitting an exponential decay function to each digital point of the Fourier transformed spin echo in order to extract the profiles of R_2 and FA.

V.2. Results and discussion

V.2.1. Characterisation of different activated carbons through isotherms

Some characteristics of the three different samples (AC monolith, AC composite, AC cloth) used in this work have been explored in greater detail with equipment available at the Nottingham Trent University, in the biochemistry department by Dr Belton. The adsorption/desorption isotherms were obtained with the "NOVA 4200-P instrument" produced by Quantachrome Intruments. This machine is linked to a remote PC and is operated with the NOVAWin2-P software.

The gas phase adsorption exhibited different isotherms for the three different AC samples, see Fig.V.6, from which qualitative and quantitative information can be drawn. Quantitative information was extracted from the isotherms using two separate methods: the BET method and the BJH method. The first method gives an estimate of the specific surface area of the micropores. The second method provides the size of the averaged pore radius and the total specific pore volume. The total specific pore volume is derived from the amount of vapour adsorbed at a relative pressure close to unity. The average pore size can be estimated from the specific pore volume. This method also conveys the specific surface area of the mesopores.
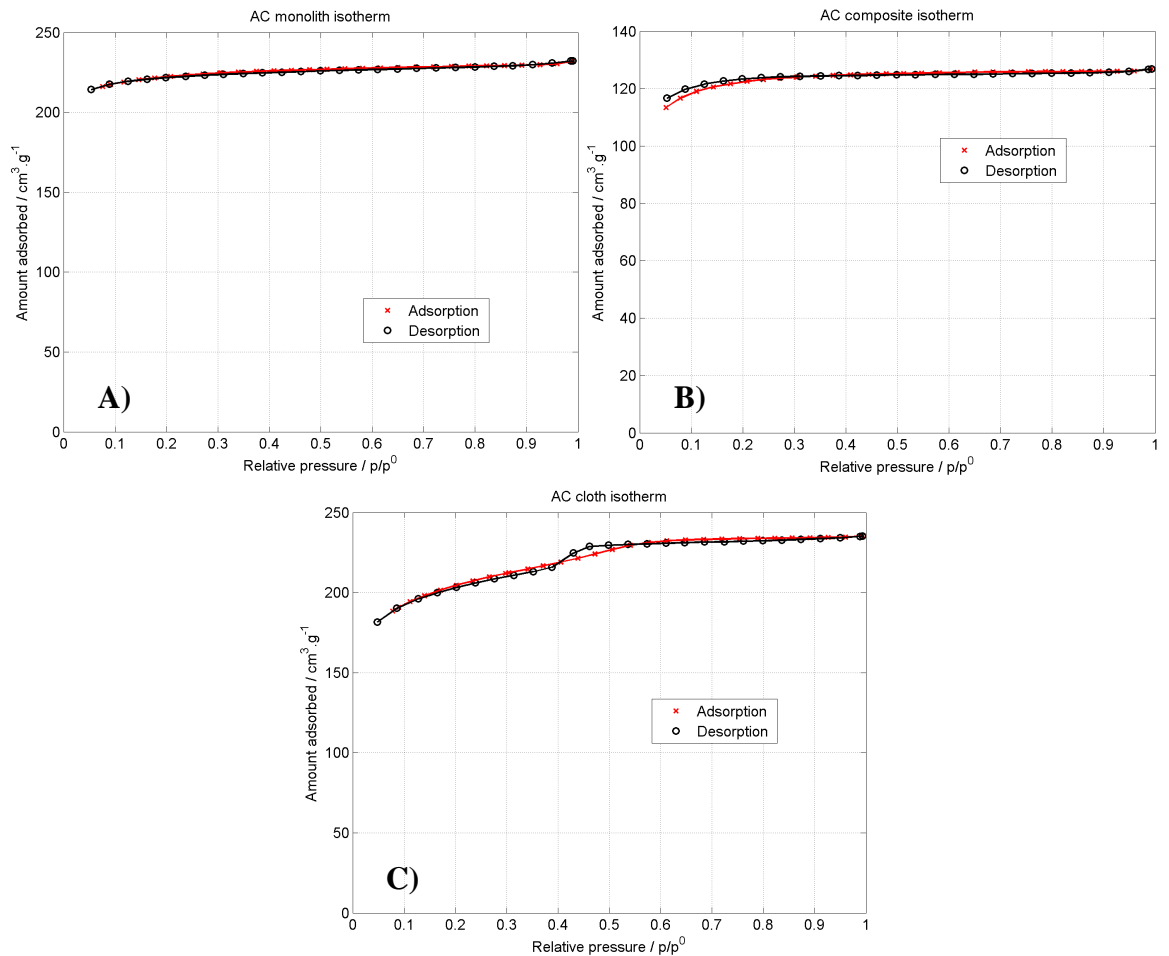
Fig.V.6: Isotherms of adsorption (red curve) and desorption (black curve) of nitrogen at 77 K on **(A)** AC monolith, on **(B)** AC composite and on **(C)** AC cloth. All adsorption isotherms are accompanied by an increase of amount adsorbed at low relative pressures (between 0.05 and 0.3) which means that the three different samples contain microporosity. Only plot **(C)** exhibits a modest hysteresis clearly denoting the presence of a slight amount of mesoporosity in the AC cloth. Note that at low relative pressure (< 0.1), the desorption isotherm does meet the adsorption isotherm on plots **(A)** and **(C)** whereas it does not on plot **(B)** which means that the degassing (before running the isotherm) was not totally completed and there may be still some residual molecules. However, this difference is little and only happens at the end of the desorption making the plot still in the limit of being acceptable. Note that (later on) the Fig.V.7 shows the same data with an expanded *y* axis.

On Fig.V.6, the three different adsorption isotherms start at relative low pressures signifying that mainly microporosity is present in the three AC samples. The isotherm **(C)** exhibits moderate hysteresis meaning that some mesopores are present in the cloth sample. From the shape of that hysteresis it appears that the cloth possesses a low energy and a homogeneous solid surface of mesopores [30]. Furthermore, all the plots present a **point B** (= inflection point, defined in section I.1.5.) which is slightly noticeable, meaning that a tiny amount of mesopores are present in the three AC

samples. The absence of hysteresis on plots **(A)** and **(B)** also confirms that only a few mesopores are present on both the AC composite and monolith. At high relative pressure for plot **(C)**, the isotherm is leveling off horizontally suggesting that only one mesopore size is available. In addition, all those isotherms remain nearly horizontal over a range of p/p^0 approaching unity implying that the three separate solids do not contain macropores. The presence of the **points B** seen on all the plots signify that at relative pressures above these points, a multilayer covering is starting to fill the mesopores. Finally, from the readings of the amount of nitrogen gas adsorbed into the samples, the isotherms on plots **(A)** and **(C)** are almost twice higher than the isotherm on plot **(B)** which indicates that there is more porosity available in the monolith and in the cloth than in the composite.

From each isotherm, the following quantitative information is extracted (based on both the BET and BJH methods) with the NOVAWin2-P software:

- the specific surface area (of both micro- and meso- pores),
- the total specific pore volume,
- and the averaged pore radius.

The methodology is briefly described in section I.1.5. and the results are given in Table V.2.

AC ⟍ Characteristics	Monolith	Composite	Cloth
Specific surface area of micropores / $m^2.g^{-1}$	685	387	626
Specific surface area of mesopores / $m^2.g^{-1}$	59	2.1	71
Total specific pore volume / $cm^3.g^{-1}$	0.040	0.005	0.067
Averaged pore radius / nm	0.80	1.77	1.64

Table V.2: A few characteristics of three different types of AC, established by the "gas adsorption technique".

Table V.2 implies the presence of microporous and mesoporous AC samples since the averaged pore radius which is smaller than 2 nm. The specific surface area of micropores of the monolith (685 $m^2.g^{-1}$) is only moderately higher than that of the cloth (626 $m^2.g^{-1}$). The specific surface area of the composite (387 $m^2.g^{-1}$) is smaller by almost a factor two compared to the monolith. The monolith has fewer mesopores (59 $m^2.g^{-1}$) than the cloth (71 $m^2.g^{-1}$) whereas the composite has a very small amount of mesopores (2.1 $m^2.g^{-1}$) compared to the two other AC samples. This means that the monolith is the densest material as in one gram the surface is the highest which requires more carbon material. Despite the fact that the AC monolith has the highest microporosity, the total specific pore volume of the AC cloth (0.067 $m^3.g^{-1}$) is greater than the one of the AC monolith (0.040 $m^3.g^{-1}$). This might be explained by the presence of a higher mesoporosity found in the AC cloth.

The qualitative and quantitative results bring complementary information from each another.

Note that all the isotherms on Fig.V.6 start with the y axis at the origin, which is how they should be presented and from which qualitative information should be extracted. However Fig.V.7 presents the same results with a zoom on the y axis. For a relative pressure of 0, the amount of adsorbate is 0 $cm^3.g^{-1}$, but usually the first point that is detected by the instrument is the one represented on the isotherm.
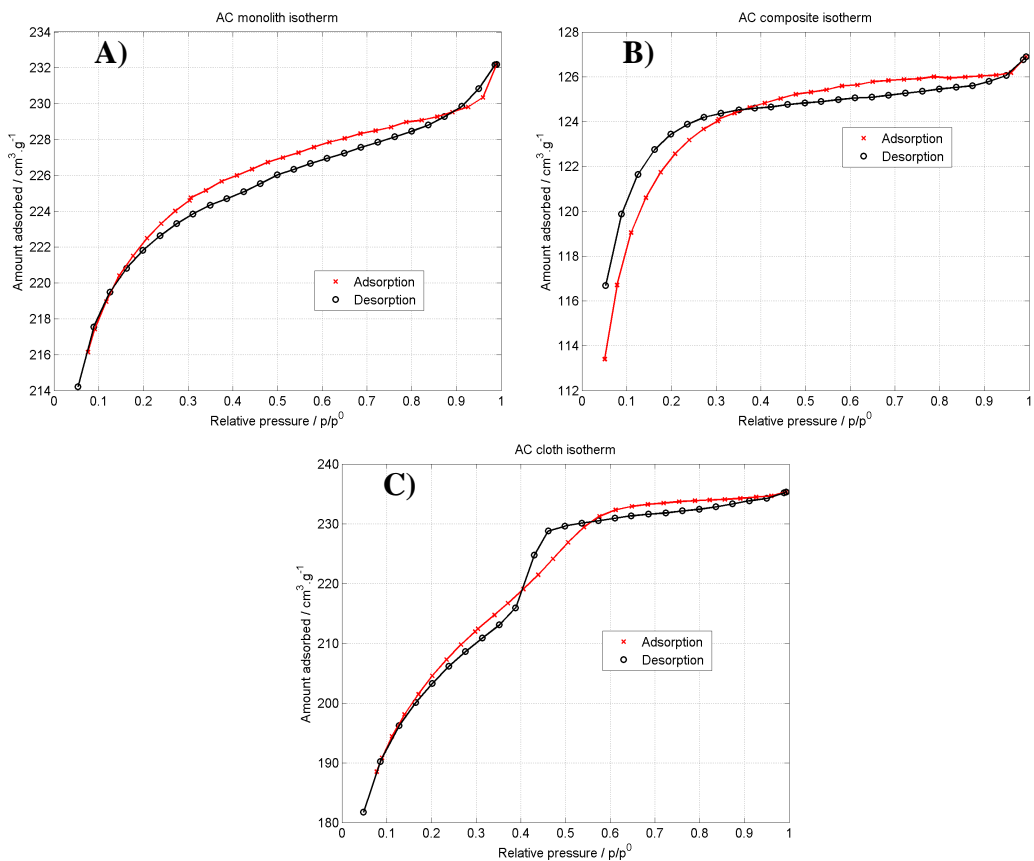
Fig.V.7: Isotherms of adsorption and desorption of nitrogen at 77 K on **(A)** AC monolith, on **(B)** AC composite and on **(C)** AC cloth. The isotherms are the same as in Fig.V.6 but are presented with a different scaling of which the origin of the *y* axis is not shown. This allows the reader to appreciate better visually the differences seen between the adsorption (red curve) and desorption (black curve) isotherms.

V.2.2. Correlation between gravimetric and NMR measurements

V.2.2.1. Gravimetric experiment on activated carbon monolith

The result of the gravimetric measurements of the uptake process (of heptane in this case) matches very well that achieved with the NMR amplitude, see Fig.V.8.
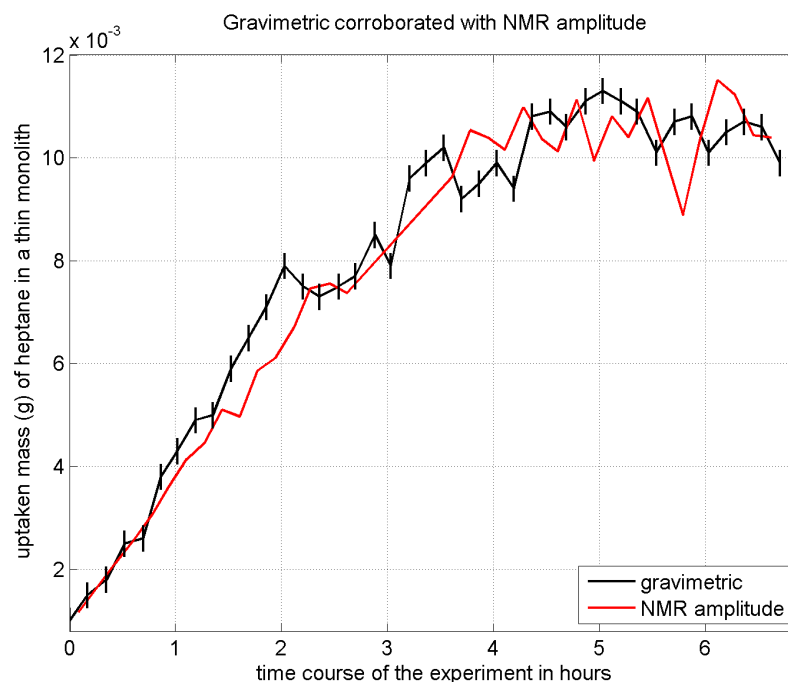
Fig.V.8: Gravimetric study compared to NMR amplitudes on the 0.5 mm thick slice of monolith. The black curve represents the gravimetric experiment and the red curve represents the NMR amplitude. The NMR amplitude was scaled so as to achieve optimal superimposition of the two curves. To do this, the NMR amplitude was linearly scaled with intercept corresponding to (1.2 ± 0.5) mg and slope corresponding to (3.1 ± 0.8) mg/hour so as to minimise the sum of the squares of the vertical deviations between the two curves. Note that it is legitimate to scale the NMR amplitude because it results from a voltage signal that has been amplified with an arbitrary gain (compensated for by the slope) and that comprises of an inherent thermal noise (compensated for by the offset/intercept). The aggrement is excellent and deviations look similar.

After 150 min the discontinuity seen in the gravimetric measurement is due to a self re-calibration of the scale. This shows that the NMR measurements are actually more steady than the gravimetric ones. Furthermore, error bars on the gravimetric measurement curve were added in order to reflect the accuracy of the scale (although they do not reflect the error inherent in the need for periodic recalibration of the scale). The relative percentage difference between the two curves was also calculated and found to be 3.9% for 10 mg of uptaken heptane. Therefore, excellent agreement between NMR and gravimetric measurements is demonstrated, validating the quantitative nature of the NMR measurements (to within a calibration) with high accuracy.

V.2.2.2. Gravimetric experiment on activated carbon cloth

The gravimetric results of water and nonane uptake provide an estimate of the evolution of adsorption followed by desorption into AC cloth. On the plot on Fig.V.9, the density of points on the horizontal axis is low. For each separate experiment, only four gravimetric measurements of the cloth were taken using the KERN mass balance. The first measurement was taken on a freshly reactivated piece of cloth. For the next measurements the fabric had to be delaminated and then reconstructed as fast as possible in order to keep good quality quantitative gravimetric data measurements. The second gravimetric measurement was taken 150 minutes later; this is usually the amount of time needed for the adsorption to reach its maximum and for the liquid droplet to vanish. During desorption two other measurements were taken, one 28 hours later and another one 67 hours later.
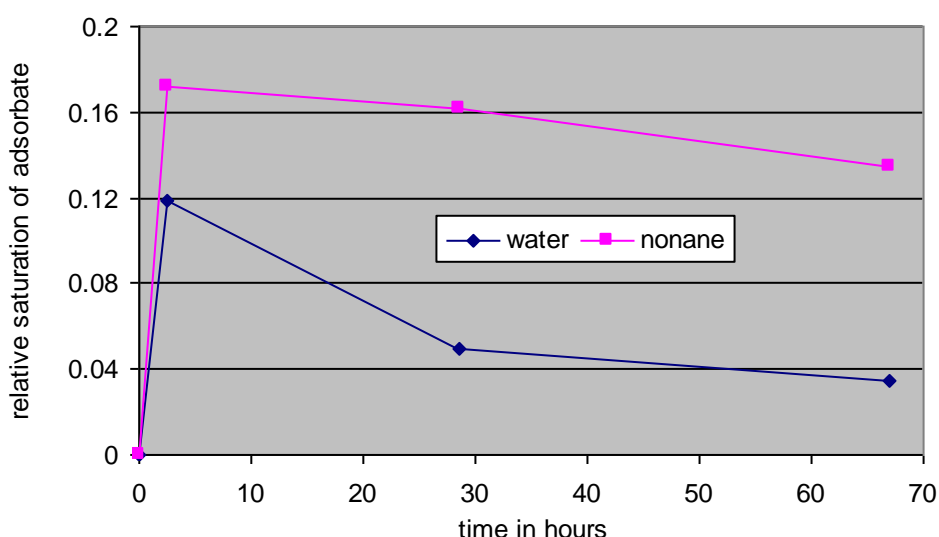
Fig.V.9: Gravimetric results of uptake of water and nonane in AC cloth. The blue curve with diamonds and the magenta curve with squares represent respectively the evolution of the relative saturation for water and for nonane into the AC cloth. In both cases, adsorption (occurring in the beginning from 0 until 150 min) followed by desorption (after 150 min) are clearly seen.

Due to small variations obtained by cutting, the two square sections of degassed cloths were not of identical weights. The cloth used for nonane uptake was 4.8 mg lighter than the one used for water uptake. As the focus of interest is the evolution of the amount of vapour adsorbed (and then desorbed) into the cloths, the saturation level (obtained by dividing the mass uptaken by the freshly reactivated cloth) is plotted. The two graphs show similar results to those seen when adsorption/desorption is monitored with NMR.

133

The rates of adsorption of both water and nonane are fast and similar although more nonane is invading the AC cloth by about 30%. The desorption is slower for nonane than for water which is also in accordance with the NMR results. After almost 3 days of desorption, 71% of water had left the cloth whereas only 22% of nonane had left the cloth.

Intermolecular attractions in the smallest pores result in adsorption forces, which cause condensation of adsorbate from solution into these molecular scale pores [97]. These adsorption forces are obviously stronger for nonane than for water as is demonstrated by nonane desorbing at a slower rate than water.

V.2.3. Adsorption in activated carbon monitored with NMR

The various effects of the high conductivity of AC on the NMR instrument has been explored in chapter III. The corroboration between the NMR amplitude and mass of adsorbate being uptaken in AC has also been shown to be excellent. Therefore the amount of water or of a specific VOC can be quantitatively monitored with the NMR Mouse®.

V.2.3.1. Adsorption of water and of heptane in activated carbon monolith

The FA increases as heptane is uptaken in the AC, for the first three hours representing the active adsorption process, see Fig.V.10.
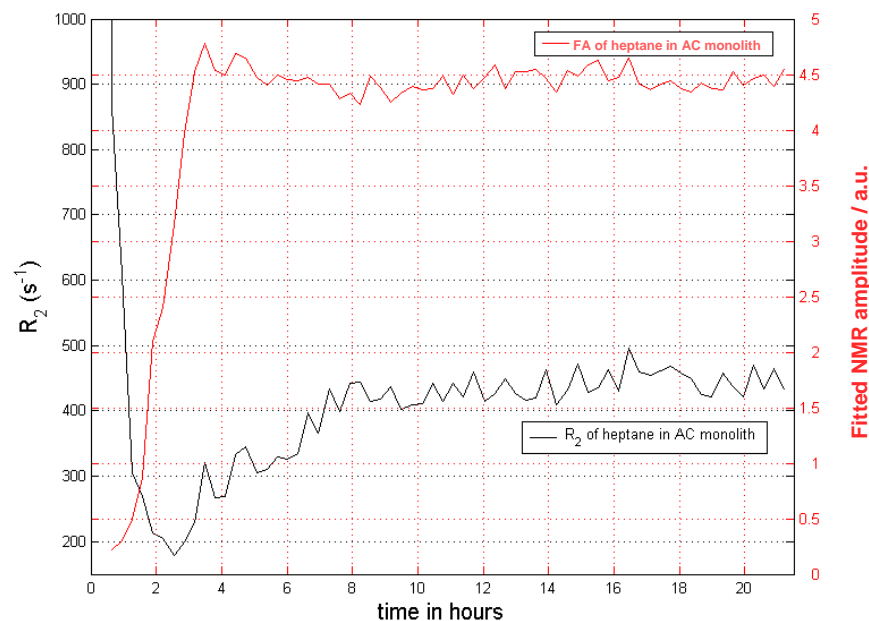
Fig.V.10: Fitted NMR amplitude (red curve) and R_2 (black curve) as a function of time, for heptane uptake in an AC monolith section (6 mm long).

A rapid and strong initial decrease of R_2 is the signature of pore filling during these 3 first hours. The first adsorbed molecules are in strong interaction with the walls of the monolith and exhibit a very high value of R_2. As small pores fill up, the molecular interaction gradually weakens and R_2 decreases (both for water and heptane, see Fig.V.15). This rapid decrease in R_2 stops (for heptane) after three hours. Following that, a small (approximately 10%) and slow decrease in FA is seen for approximately 5 hours during which R_2 also increases slowly to approximately twice its lowest value. Although this small decrease in FA might be caused by changes in T_1 value *i.e.* the T_R value (400 ms) could be too short resulting in only a partial recovery of the magnetisation, it cannot be proved for fact as the T_1 measurement had not been performed. Note that this decrease in FA is moderate and within the range of deviations seen to come from thermal noise, whilst the increase in R_2 is much more pronounced and well above thermal noise deviations. After a total of 8 hours of adsorption, the system reaches a steady state and both the NMR amplitude and its associated relaxation rate remain constant. This demonstrates that during the first 8 hours, the heptane molecules' interaction with the AC undergoes important dynamic changes. This suggests that even though the adsorption process has more or less reached a steady state from the point of view of the amount of molecules adsorbed after 3 hours of the

experiment, substantial changes still occur within the system from the point of view of molecular interactions with the AC.

Another way of presenting this result is by plotting the fitted NMR amplitude versus the relaxation time, see Fig.V.11.
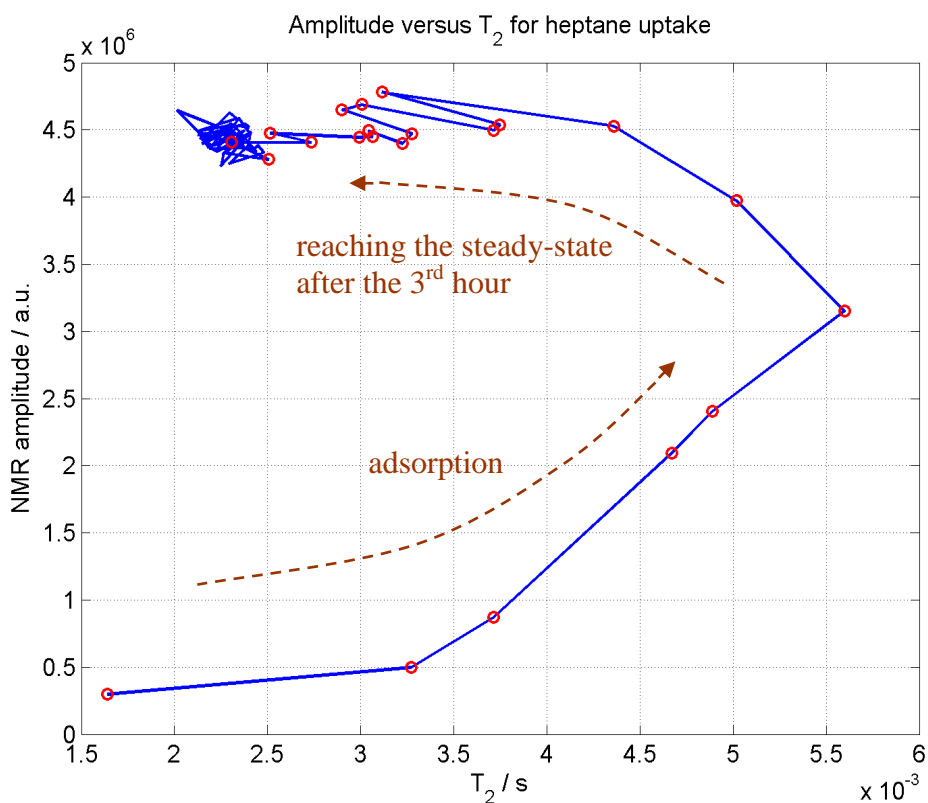
Fig.V.11: Correlation plot of the fitted NMR amplitude versus T_2. During adsorption (see arrow), the NMR amplitude goes up, whereas T_2 increases. As the adsorption process slows down, a formation cloud of segments can be seen on the curve which corresponds to a steady-state saturation obtained in the AC monolith. Note that the first 8 hours of adsorption are represented by red dots on the blue curve.

It is seen in chapter I that in the early 70's, Conard measured a change in chemical shift and linewidth with surface layer covering, see Fig.I.2 and Fig.I.3. In addition, in chapter II the relationship between the linewidth and T_2 is given through Eq [II.15]. Therefore, the data from Conard can be rearranged by reading his linewidth and converting it to T_2, which is what is shown in Fig.V.12. The relationship between the surface layer covering, θ, and saturation level is given in [98, 99], which suggest that θ is proportional to saturation level and therefore to the value of FA.
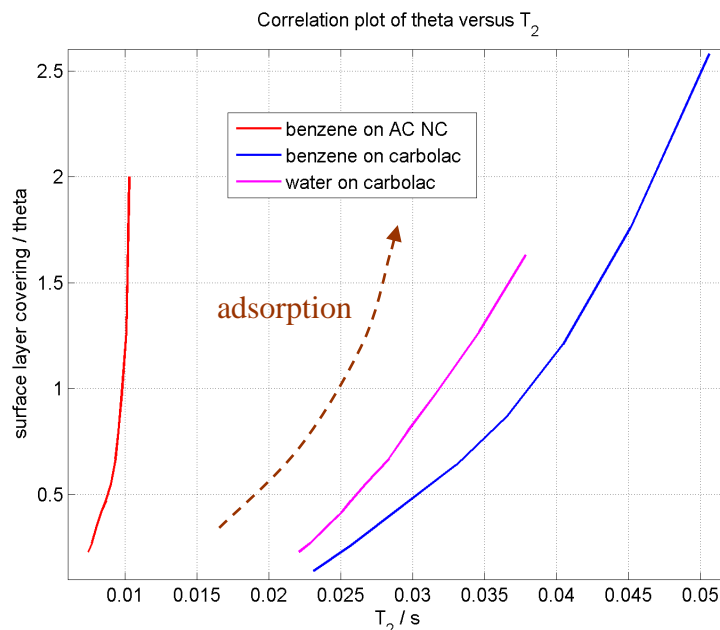
Fig.V.12: Correlation plot of the surface layer covering theta, θ, versus T_2. The data source was taken from the fitted curves of Conard's results [33, 34]. During adsorption of benzene or water on a certain type of activated carbon, the T_2 goes up. The surface layer covering can be assimilated to measurements of the NMR amplitude, FA, in this thesis because it is probing an amount of molecule adsorbed in AC. In this case the value of T_2 is increasing, in a non-linear fashion, with surface layer covering during adsorption.

The relationship between the NMR amplitude and T_2 that is measured in this thesis corresponds extremely well with Conard's converted data. Indeed, during the initial active adsorption, T_2 also increases non-linearly with the NMR amplitude. The adsorption curve of benzene on AC NC (Activated Carbon CocoNut) exhibits values of T_2 (from *ca.* 3 until 10.5 ms) which lay within the range of values found on the measurements of T_2 (from *ca.* 1.5 until 5.5 ms) of heptane on AC monolith. Also, the adsorption curves of benzene and water on carbolac exhibits values of T_2 (respectively from 23 until 51 ms and from *ca.* 22 until 37 ms) which lay within the range of values found on the measurements of T_2 (from *ca.* 8 until 29 ms) of water on AC monolith. It is more complicated to relate Conards' results of theta to the results of FA because it is not known how many layers of adsorbate are covering the AC monolith. However, it is known that the AC in this thesis work is mainly constituted of microporosity with a little mesoporosity, which means that there is more than one layer covering and therefore Conard's curve might represent only the beginning of the FA measured here.

The results for the water uptake process, which is simpler than the one occurring for heptane, are now presented, see Fig.V.13.
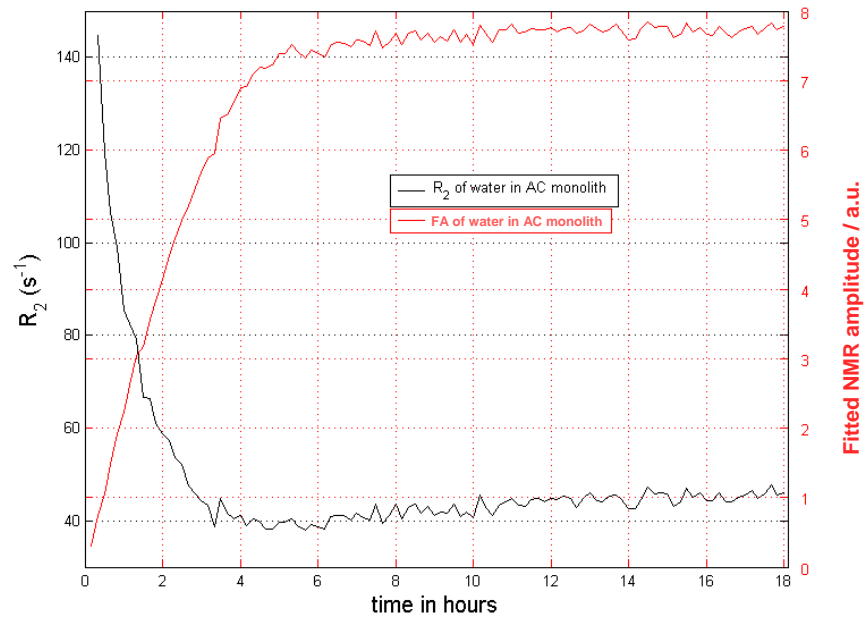
Fig.V.13: Fitted NMR amplitude (red curve) and R_2 (black curve) as a function of time, for water vapour uptake in a very thin (0.5 mm) AC monolith section without its outer rim.

The FA increases as water is uptaken in the AC, for the first 4 hours representing the active adsorption process. As seen previously for heptane uptake, a rapid and strong initial decrease of R_2 is the signature of pore filling during the three and a half first hours. During the next 6 hours of uptake, the increase of the FA is slow and at the limit of being measurable. Finally, after 10 hours of uptake, the FA is reaching a plateau probably resulting from the AC monolith being saturated with vapour and thus becoming inactive. When the time course of the FA is in a "slow regime" or not evolving anymore, the relaxation rate value increases slowly and continuously which must correspond to some moderate molecular distribution rearrangement, resulting in a small fraction of molecules gradually becoming strongly adsorbed (as seen for heptane molecules in the previous section). By displaying this result as the fitted amplitude versus T_2, see Fig.V.14, a typical curve which is characteristic of adsorption leading to saturation is obtained.
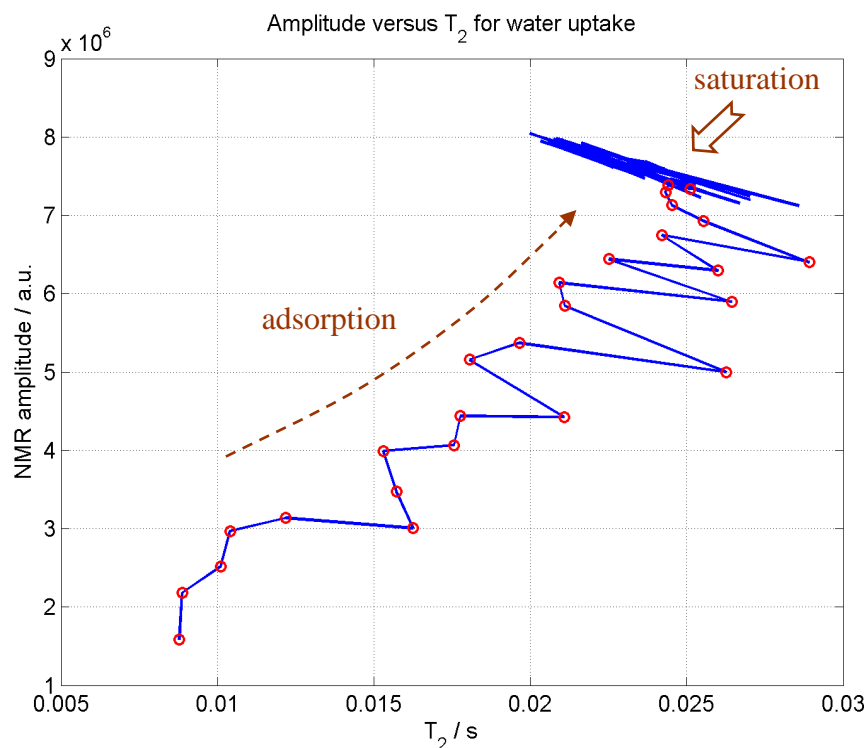
Fig.V.14: Correlation plot of the fitted NMR amplitude versus T_2. During adsorption, both the NMR amplitude and T_2 increase. When the system approaches full saturation, a formation of cloud of segments can be observed, this time residing in a location quite different from that seen in Fig.V.11. Note that the first 5 hours of adsorption are represented by red dots on the blue curve.

Again the relationship found between the NMR amplitude and T_2 corresponds extremely well with Conard's converted data, see Fig.V.12, although here the data seems remarkably linear. This confirms Conard's results where T_2 increases with the surface layer covering.

During the uptake process for both heptane and water vapours, the correlation plot of the fitted NMR amplitude versus T_2 clearly exhibit different shapes which allows a differentiation between different adsorptives invading the AC monolith. The correlation plot for water is linear, but is non-linear for heptane. Indeed, the correlation plot for water seems to follow a straight line whereas the one for heptane goes around a rotation of *ca.* 180 degrees. The reason for this might be explained partly due to differences in T_1 values, as mentioned earlier. This strongly implies that vapours of heptane and water undergo different molecular interactions with the AC monolith during adsorption.

The transverse relaxation rate of water (found between approximately 145 and 40 s^{-1}) substantially differs from that of heptane (found between approximately 1000 and 200 s^{-1}) with no overlap which means that these two particular molecular species could be fully differentiated from one another on the basis of their relaxation rate.

V.2.3.2. Contrast between water and nonane vapours uptake in activated carbon cloth

One aim of this thesis is to characterise a protective material's performance against a vapour rather than against a liquid. Oil is not suitable for such a characterisation because it does not adsorb onto AC but ingresses into it (in a liquid state) as discussed in chapter IV. Compared to heptane and nonane, Duckhams oil has a higher viscosity and a higher boiling point (as is seen in Table V.1), which makes it almost impossible to evaporate at room temperature. As a reminder, the experimental set up is made of an AC cloth sandwiched between two repellent layers. In the laboratory's atmosphere, a droplet of heptane placed on top of the repellent layer passes through it within seconds whereas nonane does not (as is measured experimentally). Therefore, heptane is not suitable for this experiment. Nonane has got a longer carbon chain and remains liquid for longer. Water also evaporates slowly compared with heptane. Therefore water and nonane were chosen for the monitoring of adsorption/desorption in AC cloth.

V.2.3.2.1. T_2 Measurement for water and nonane in activated carbon cloth

Adsorption of the two different vapours (water and nonane) in textile cloth was successfully monitored with the profile NMR Mouse$^{®}$. During adsorption, R_2 is decreasing for both water and nonane. When the adsorption process is finished, R_2 remains constant for nonane whereas R_2 increases for water as can be seen respectively on Fig.V.15 and Fig.V.16.

Fig.V.15: Fitted NMR amplitude (red curve) and R_2 (black curve) as a function of time, for nonane vapour uptake in AC cloth. R_2 goes down during adsorption and then reaches a steady state. FA goes up during adsorption and then reduces moderately (approximately 9%). The vertical dotted line highlights the time at which the droplet totally evaporated.

For nonane, the relaxation rate decreases from 580 s^{-1} to 310 s^{-1} perhaps followed by a slight increase of 10 s^{-1} (although this is within the thermal noise-driven deviations), whereas for water it goes down from 480 to 200 s^{-1}, then it goes up slowly to 320 s^{-1} after which it reaches a plateau, see Fig.V.16. The time course of the individual relaxation rates is again most probably a signature of pore filling and is, again, seen to be different for different molecular species.

For nonane, the FA (see Fig.V.15) reaches a maximum after two hours and a half which corresponds to the total evaporation of the droplet (as was observed by eye during the experiment). This does not necessarily mean that the cloth is fully saturated as the droplet has totally evaporated and the challenge has therefore been altered. For later stages of the experiment the NMR amplitude decreases very slowly by approximately 9% before reaching a plateau.

For water, the NMR amplitude is going up for 135 minutes (which is the time required for the total evaporation of the water droplet as was measured experimentally). After that, it rapidly decreases by approximately 45% most probably corresponding to desorption, see Fig.V.16. This strongly suggests that the water in this AC cloth desorbs substantially and spontaneously after reduction of the challenge, whilst this process is hardly measurable for the case of nonane.
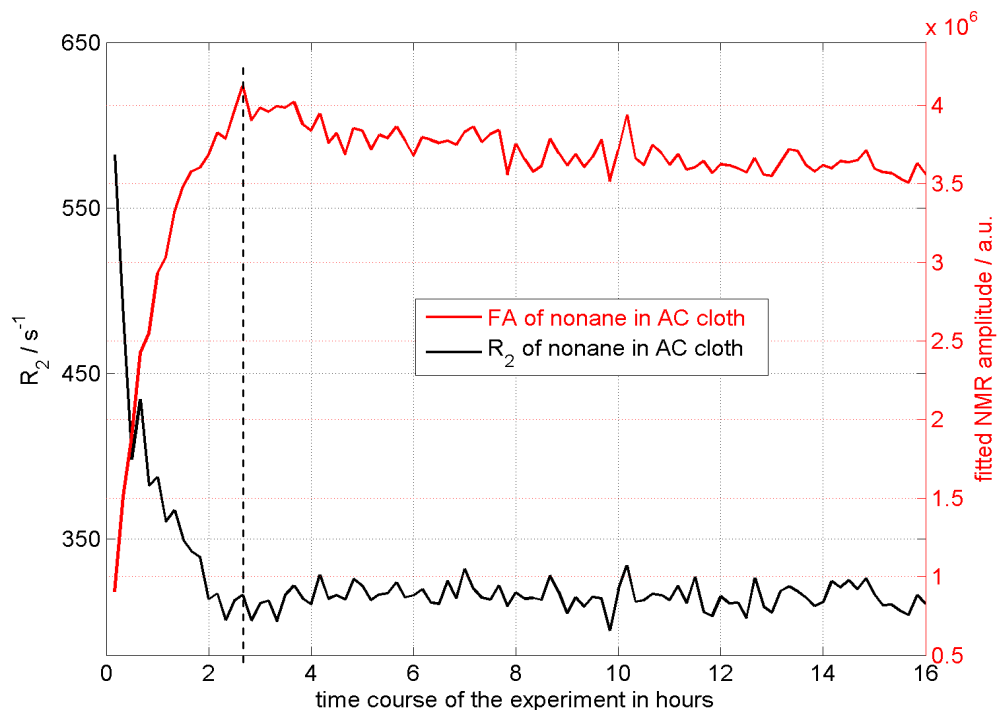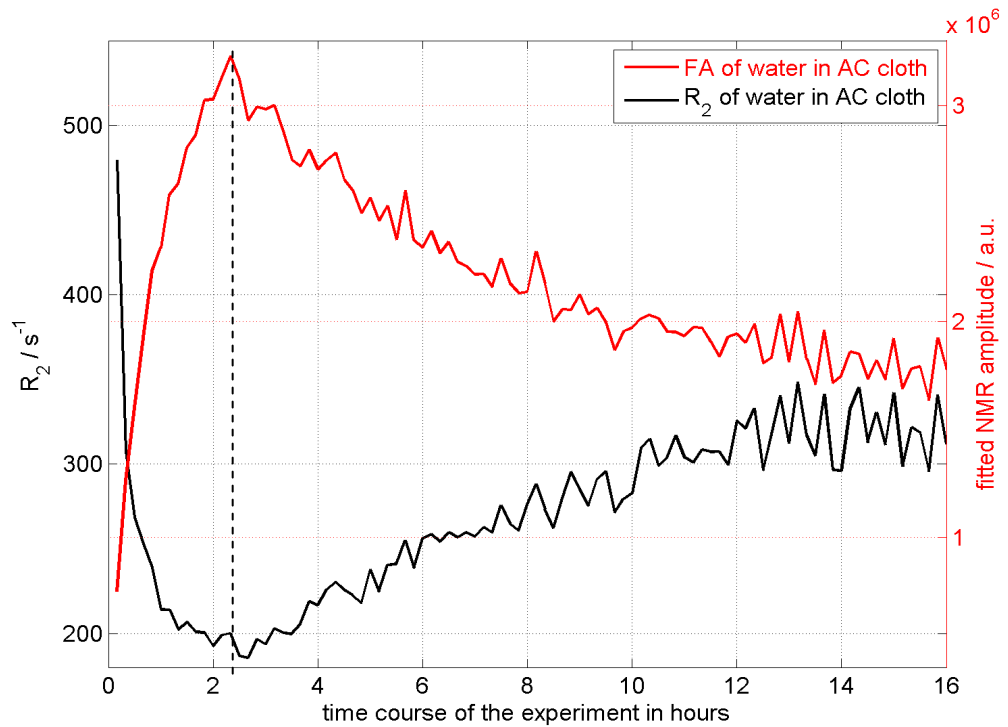

Fig.V.16: Fitted NMR amplitude (red curve) and R_2 (black curve) as a function of time, for water vapour uptake in AC cloth. R_2 decreases during adsorption and then increases slowly. FA increases during adsorption and then decreases substantially (approximately 45%). The vertical dotted line highlights the time at which the droplet totally evaporated.

Earlier in this thesis, see section V.2.2.2., gravimetric measurements of uptake of vapours of water and nonane were obtained on a square sections of AC cloth. It has thereby been established that the FA of water and nonane matches well the respective mass of uptaken molecule.

Both for water and nonane, a strong linear correlation between NMR amplitude and relaxation time (T_2) can also be seen over a similar range of values, but with differing gradients ($(16.6 \pm 0.4) \times 10^8$ for nonane and $(5.6 \pm 0.6) \times 10^8$ for water), see Fig.V.17. This strongly suggests that AC saturation can also be monitored with T_2, without the

need for NMR signal calibration, provided that the molecule under investigation is known.
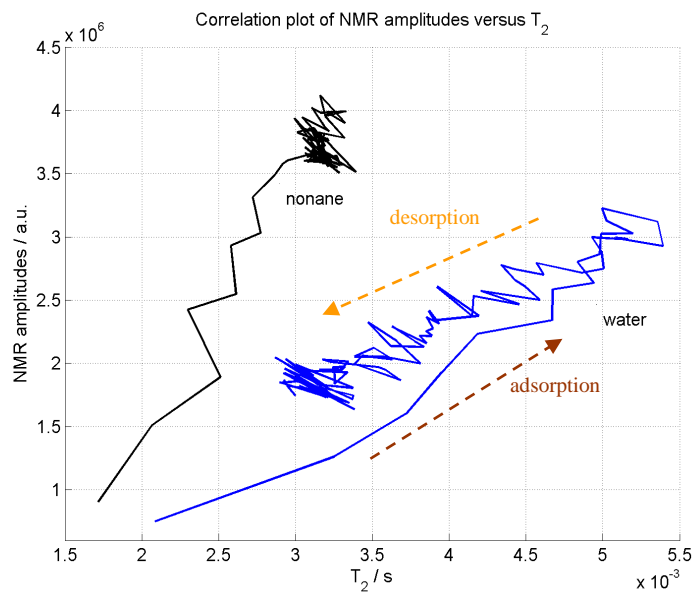
Fig.V.17: Correlation plot of the NMR amplitude versus T_2 for water and nonane. During adsorption, the FA seems to increase linearly with T_2 for the two different molecules. During desorption the NMR amplitude seems to remain linearly correlated with T_2 for water but for nonane such a conclusion is not possible because the extent of the observed desorption is negligible, resulting in a formation of a cloud of segments onto the curve.

The initial part of these curves corresponding to surface layer covering during adsorption does, again, match the shape of Conard's rearranged curves seen on Fig.V.12 where T_2 increases with the FA during absorption. This suggests once more that the saturation level can be monitored.

A clear hysteresis may be seen on the water data, ending up in two separate curves for adsorption and desorption. This might be caused by the T_1 effect (see next section V.2.3.2.2.). As has been seen in the monolith measurements, the measurement of the NMR relaxation time, T_2, offers in AC cloths the possibility of monitoring the saturation levels of two (or more) different molecular species, provided that the particular adsorptive molecule under investigation is known. It is worth noting that although the FA seems strongly linearly correlated to R_2, these two NMR parameters do not yield the same information. The hysteresis and the non linearities sometimes seen, are both evidences for that. As mentioned earlier in section V.2.3.1., T_2 also reveals the

strength (for a given molecular species) of fixation on the walls of the adsorbent, whilst FA reveals the saturation level.

Experimental repeats were obtained for water (2 repeats) and nonane (3 repeats) uptake, see Fig.V.18 and Fig.V.19. The original experiments are added for comparison purposes.

$$y_C = 5.64 \text{ x } 10^8.T_2 + 6.57 \text{ x } 10^4$$

$$y_D = 4.47 \text{ x } 10^8.T_2 + 21.5 \text{ x } 10^4$$

$$y_E = 4.77 \text{ x } 10^8.T_2 + 5.50 \text{ x } 10^4$$
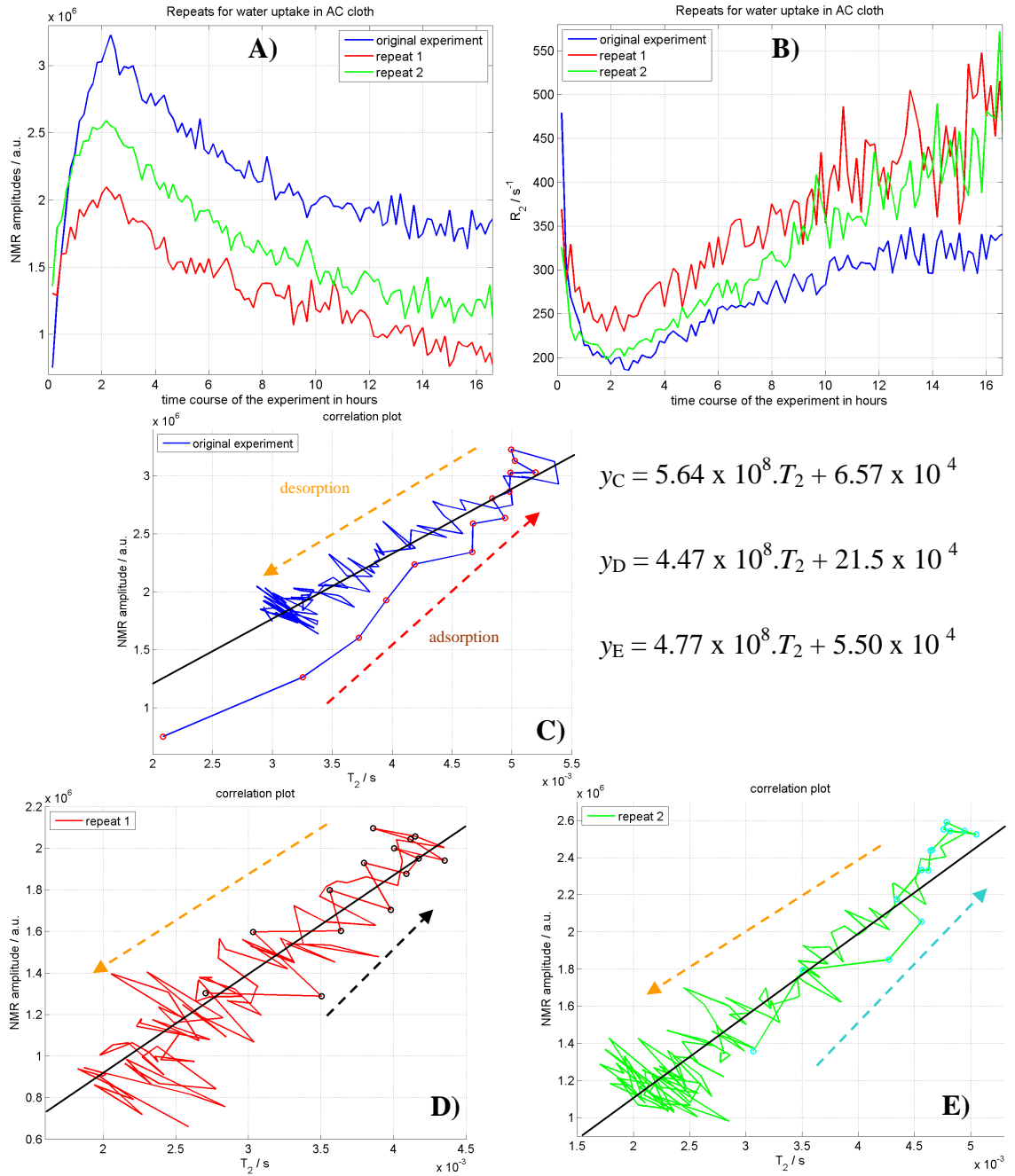
Fig.V.18: Repeats for water uptake in AC cloth. Plots **A**, and **B** represent respectively the time course of the NMR amplitudes and the time course of R_2. **C**, **D** and **E** represent the correlation plot of the NMR amplitudes versus T_2. The dots on graphs **C**, **D** and **E**, correspond to the first 135 minutes of adsorption, after which the droplet has totally evaporated. Some variations are seen on **A** and **B** and these are most likely to be due to genuine experimental set up variations rather than from the NMR monitoring technique, whereas **C**, **D** and **E** had to be shown separately as they match remarkably well. For each of these graphs, their respective y_C, y_D and y_E gradients and y intercept values are calculated (by fitting the black curve on each graph) and displayed.

Prior to each NMR experiment the same sample cloth was reactivated in a vacuum oven at 160 °C during four hours. For each separate experiment, the NMR parameters

were strictly kept identical. The droplet size was not varied. It is also seen that the gradients and the *y* intercepts are moderately varying from one another. This leads to remarkably similar repeats for the correlation plots.
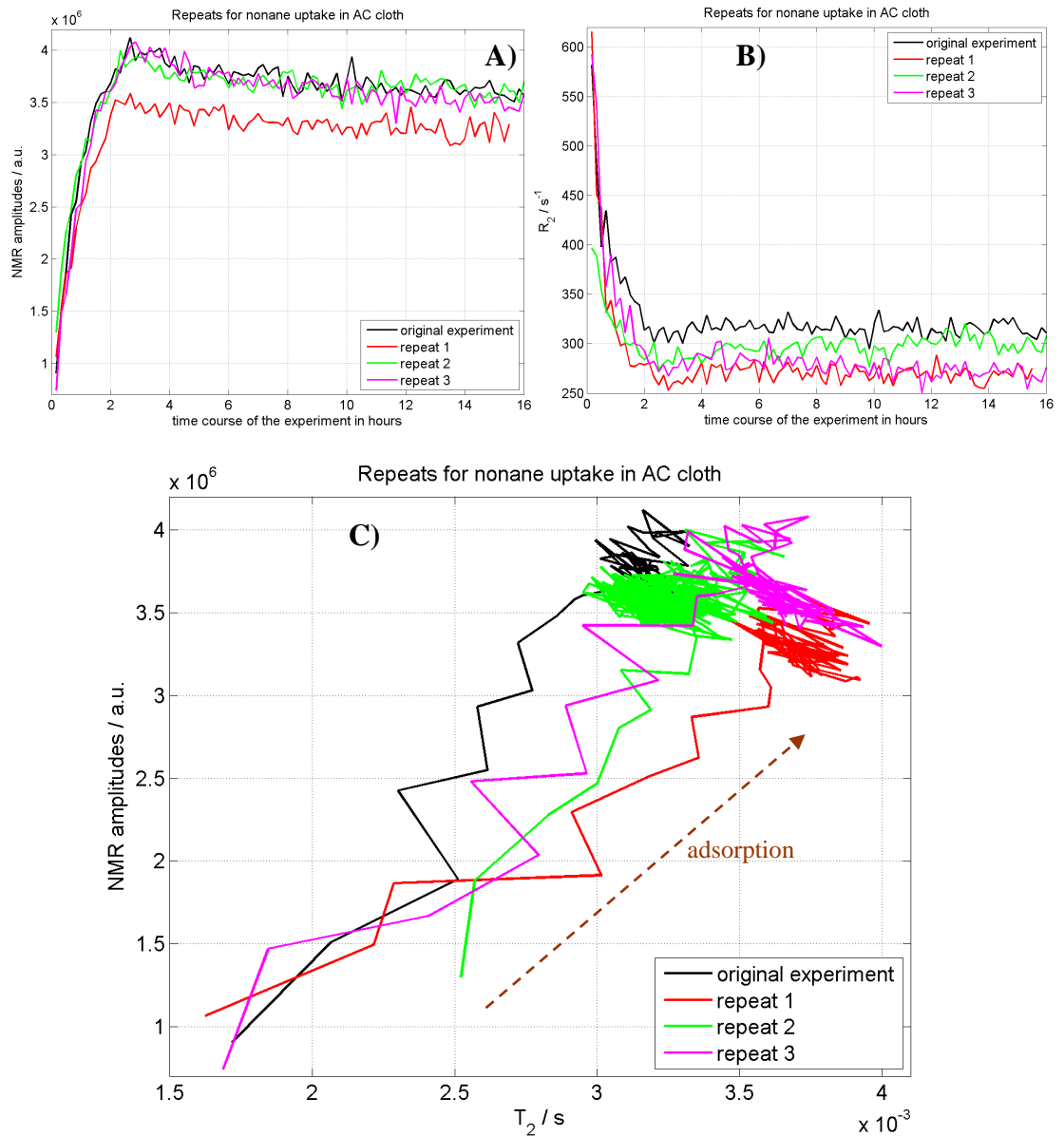
Fig.V.19: Repeats for nonane uptake in AC cloth. Plots **A, B** and **C** represent respectively the time course of the NMR amplitudes, the time course of R_2 and the correlation plot of the NMR amplitudes versus T_2. Some variations are seen from one experiment to another and these are most likely to be due to genuine experimental set up variations rather than from the NMR monitoring technique.

Although the same comments as for the water uptake can be said for the preparation of the experimental set up, the correlation plots in Fig.V.19 exhibit a few variations.

V.2.3.2.2. T_1 Measurement for water vapour uptake in activated carbon cloth

By fitting the Fourier transformed spin echoes to an exponential decay, see Eq [II.13], the T_1 value was measured every 10 minutes over a period of 34 hours. The NMR amplitude (Fig.V.20) exhibits the usual exponential increase (fast adsorption) followed by a slower increase and finally followed by a slow desorption. This particular "NMR amplitude" seems to differ slightly from all the previous plots of "NMR amplitude" shown so far. First of all the SNR is better which is seen by less deviation of thermal noise occurring on the graph. Secondly, the shape exhibits a fast increase during the first two and a half hours, followed by a slow increase during another two hours after which a plateau is reached during 30 minutes. This might be due to (i) the vapour density which is slowly decreasing as the droplet evaporates and (ii) the monitoring of the saturation level. Once the droplet has totally evaporated (after 5 hours), a rather pronounced initial decrease of the NMR amplitude by 8% occurs over one hour. This could be explained by the challenge being exhausted resulting in this quick but moderate initial desorption. After that the NMR amplitude reduces slowly as can be seen on the NMR amplitude of the previous plots. This NMR amplitude is probably probing dynamic effects occurring at the molecular level during adsorption and desorption which are very similar than those seen with the NMR amplitude of the previous plots.

The T_1 curve can be divided into three parts. To start with, the first half an hour demonstrates a dramatic decrease of T_1 from 80 until 29 ms. This process, to the best of my knowledge, has not been shown in the existing literature, and its interpretation requires theoretical modelling of longitudinal relaxation [100] which is not considered within the frame work of this thesis. The second part lasts for approximately four and a half hours and shows a moderate increase from 29 until 32 ms followed by a plateau. The last part of the curve (occurring during water desorption, as has been seen in all other experiments, and as is further demonstrated by the time course of the signal amplitude) exhibits a slow and constant decrease of the T_1 value from 32 to 23 ms. The time course of T_1 is close to that of the NMR amplitude, but for the slow desorption process only.
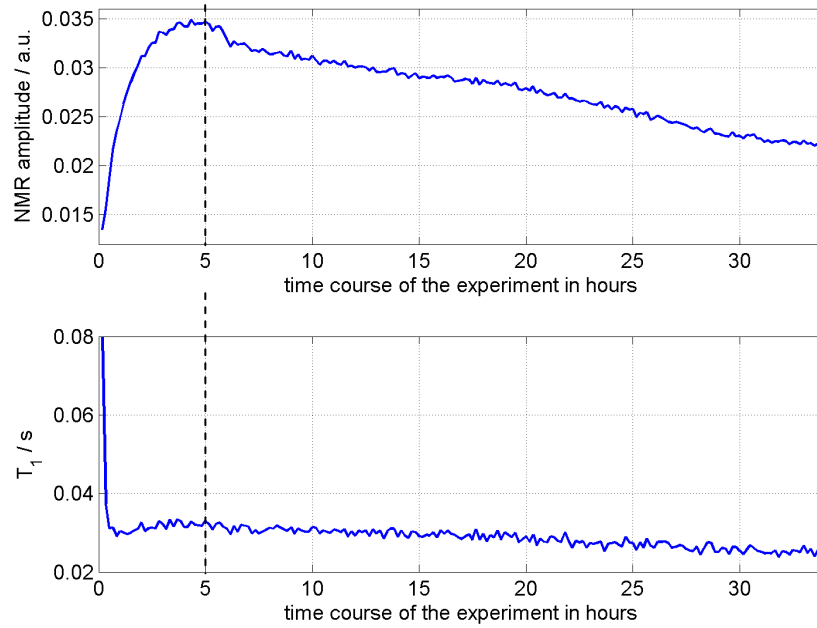
Fig.V.20: Time course of the amplitude (M_0) and T_1 for water adsorption followed by desorption in AC cloth. The vertical dotted line highlights the time at which the droplet totally evaporated.

The correlation plot of NMR amplitude versus T_1 is also plotted, see Fig.V.21. This type of plot exhibits a typical shape which is very reliable as is demonstrated by three other repeats shown in Fig.V.22.
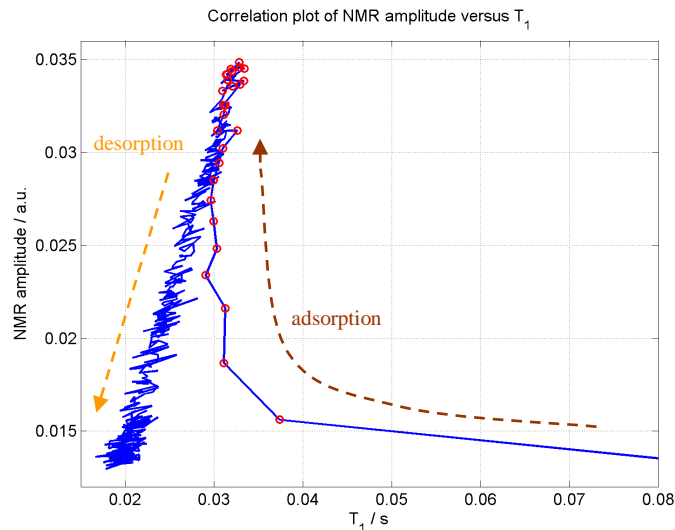
Fig.V.21: Correlation plot of the NMR amplitude versus T_1 for water. The two processes of adsorption and desorption are clustered in extremely well separated areas of the plot. Note that the red dots on the blue curve correspond to the first five hours of adsorption, after which the droplet has totally evaporated.

148

The data clearly demonstrates that T_1 measurements yield different information from T_2. The effect of T_1 is consistent with the hysteresis seen on the amplitude-T_2 plot: at the beginning of the uptake experiment, T_1 is the longest and approximately ten times shorter than the repetition time used in the T_2 measurement (the ratio of $T_1/T_R = 0.12 \pm 0.03$), so that when T_1 shortens, the signal is enhanced which is indeed the correct "direction" of the hysteresis seen on the amplitude-T_2 correlation plots, since the desorption is seen to be "higher" than the adsorption curve for any given value of T_2. By shortening T_R the hysteresis should be larger.
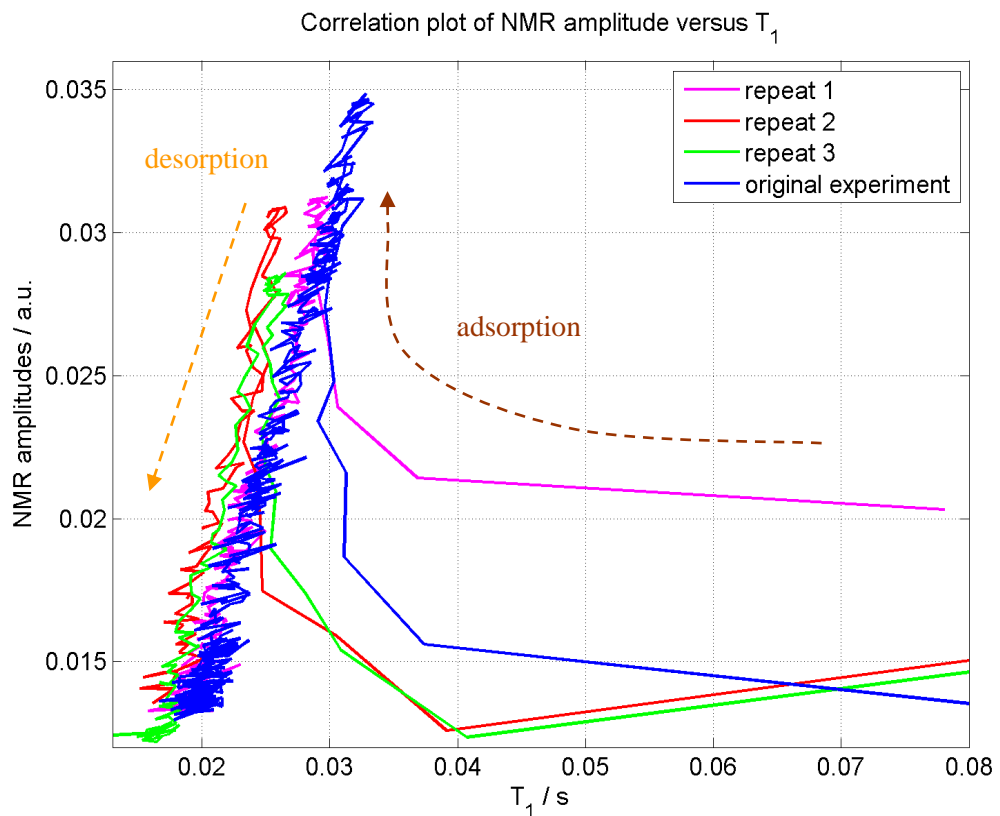
Fig.V.22: Repeats of T_1 measurement for water uptake in AC cloth. These correlation plots of NMR amplitude versus T_1 show a few discrepancies which can be explained by small experimental protocol variations, such as how long the freshly degassed AC cloth is exposed to the laboratory atmosphere. When the AC cloth is reactivated, it adsorbs the humidity of the air quite well resulting in a value of the first measurement of the NMR amplitude that may vary substantially. Therefore the time required to launch the experiment should be reduced as much as possible. However, for each repeat, the two processes of adsorption and desorption are clustered in extremely well separated areas of the plot. The original experiment is added for comparison purposes.

V.2.3.3. Spontaneous uptake of dodecane

It has been shown in chapter IV that the NMR Mouse® can be used to quantitatively monitor the complex ingress of an oil into a thin fabric either made of three stacked individual layers, each 70 µm thick, or made of an AC cloth (200 µm thick) sandwiched between two repellent layers. The ability to determine the location of a liquid (or an adsorbate) within a textile laminate is extremely useful in developing an understanding of how, or whether, a material is able to offer protection towards a liquid (or an adsorptive) contaminant. In the design of protective clothing, air permeable textiles exploits activated carbon as means of removing volatile chemicals. In this section it is shown that the NMR Mouse® can also be used to monitor the uptake of a vapour into a laminate fabric comprising an AC cloth. The entire textile is imaged (with NMR) in this experiment which is conducted with an evaporating drop of dodecane (rather than a liquid drop that is forced into the textile), see Fig.V.23.
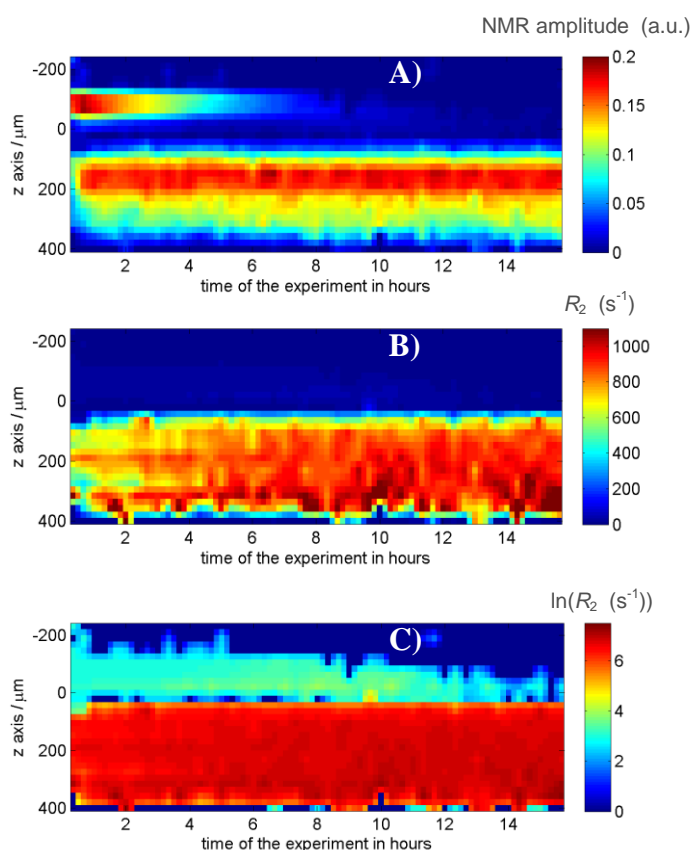
Fig.V.23: Dodecane vapour uptake in an AC cloth sandwiched between two repellent layers. **A, B** and **C** represent respectively the colour coded vertical profiles of the NMR amplitude, the colour coded transverse relaxation rate and the colour coded natural logarithm of R_2.

As dodecane evaporates a vapour propagates in all directions. From the NMR amplitude, the signal build up of adsorbed dodecane in the central sandwiched AC cloth is clearly seen together with the reduction in the height of the droplet sitting on the top of the system. There is a lack of signal in the 70 μm between the bulk dodecane and the AC cloth, due to the repellent layer that is not adsorbent. This top repellent layer is therefore only used as a separate porous sheet to allow the pool of liquid dodecane to be in very close proximity of the cloth. Significant signal intensity is observed to rapidly accumulate in the activated carbon cloth.

On the plot of the time course of the vertical profile of the relaxation rate, a clear increase of R_2 from 500 s^{-1} until 900 s^{-1} is seen in the cloth, whilst that of the dodecane sitting on the top of the system is so low that it is just about visible in the deep blue range of the colour coding. In contrast to R_2 of the molecules adsorbed onto the activated carbon, that of the dodecane droplet does not change with time (as expected). The increase in dodecane's R_2 in the AC cloth (from 570 until 950 s^{-1}) is different from that previously seen for uptake in AC monolith (140 until 40 s^{-1} for water and 1000 until 200 s^{-1} for heptane, see V.2.3.1.) and in AC cloth (480 until 190 s^{-1} for water and 570 until 325 s^{-1} for nonane, see V.2.3.2.1.). Finally, the profiles of the natural logarithm of dodecane's R_2 enable both states of dodecane and their respective time courses (free and adsorbed) to be identified.

V.3. Conclusion

Unilateral NMR provides very useful insight in the uptake of molecules in a porous material under standard protocols. Using a non invasive method, the uptake of several VOCs and water in a sample important to the industry can be can monitored and distinguished, even though it is challenging from its electrical conductivity point of view. It was also demonstrated that the nature of the NMR measurements are quantitative with regards to the linear density of a liquid found at a given z coordinate.

The uptakes of water and heptane vapours were successfully monitored in AC monolith samples. The time course of the NMR amplitude illustrates the saturated level of the

vapours. The time course of their NMR transverse relaxation rates exhibits similar trends but shows evidence of different specific path for a given molecule.

It is important to undertake experiments of adsorption of gases and vapours onto different types of porous media in order to bring information on the dynamic effects occurring at the molecular level during the uptake process. These effects can be different for an AC monolith than for an AC cloth subjected to the uptake of the same vapour. Adsorption for both nonane and water vapours were quantitatively monitored non-invasively without the need of delaminating the samples comprising the AC cloth. When the challenge becomes negligible, the monitoring technique also reveals two separate observable facts: (i) spontaneous desorption occurs immediately following the removal of the challenge; (ii) water desorbs substantially (45% signal change in 13 hours) whilst this process is hardly measurable (9% signal change in 13 hours) for the case of nonane. In spite of being independent parameters, the measured NMR amplitude often follows the trend of the measured NMR transverse relaxation time and both provide mostly information regarding the saturation level. The latter however gives additional information such as different changes in molecular rearrangements for different molecular species. It has been shown that T_2 is a good indicator of adsorption and is also a promising parameter to measure in order to get the saturation level of the AC with good accuracy without the need for calibration provided the molecule under investigation is known.

In contrast to T_2 measurements, T_1 shows another type of monitoring of adsorption/desorption in AC cloth for water vapour. It remains to be seen whether the T_1 measurements promise additional useful information about desorption phenomena in AC.

Furthermore, it has been shown that unilateral NMR is capable of imaging vapour adsorption in a multi-layered fabric by depth profiling into the vertical-direction without the need to physically move the sample relative to the instrument. Once the dodecane vapour has passed through the top repellent layer of the textile laminate containing AC cloth, adsorption was monitored and the instrument provided information on the quantity of adsorbate present at different depths of the x-y plane.

CHAPTER VI: SUMMARY AND FUTURE WORK

VI.1. Summary

This thesis demonstrates that the aims described in the beginning (in section I.1.1.) have been accomplished. The fate of a liquid *mimicking a toxic liquid* ingressing into a layered fabric has been non-invasively monitored, and the amount found at different depths of the protective textile was also revealed by means of inexpensive NMR. An extension of this method has been applied to a self-made *intelligent* fabric comprising activated carbon material which has a great performance to adsorb a large amount of vapours (simulant for toxic vapours).

This work thereby presents a new way of monitoring the dynamic liquid ingress and adsorptive uptake of vapours into different porous materials. The work comprises of two main sections:

The first one demonstrates a promising method to quantitatively and non-invasively monitor the dynamics of liquid ingressing into a layered fabric made of a combination of repellent and non-repellent layers and/or into an activated carbon cloth layer, with the use of a low field-unilateral NMR instrument. The second one is concerned with monitoring the uptake of a vapour in activated carbons with the same NMR device. In both cases, the AC materials present challenging issues, which are extensively explored, arising from their electrical conductivity.

In these studies, the geometry of the samples is found to match well that of the sensitive volume of the *profile* NMR Mouse$^{®}$ and therefore allows the efficient exploitation of Fourier transformed NMR, rather than physically moving the instrument relative to the sample. The CPMG sequence is used in conjunction with the built-in field gradient. Mono- and biexponential decays are fitted to the Fourier transformed spin echoes in order to extract 1D profiles of the NMR amplitude and the relaxation rate.

The technique has been shown to be powerful in that (i) the dynamics of liquids can be explored without the need to delaminate the porous textile samples; (ii) the

adsorption/desorption and the saturation level of ACs can be measured by means of NMR transverse relaxation and/or amplitude and measurements of the saturation level are shown to be possible without any further calibration provided that the molecule under investigation is known. NMR transverse relaxation measurements bring at least two additional benefits. They are extremely robust in spite of the artefacts due to the AC electrical conductivity and they are able to probe molecular rearrangements for a given molecular species.

Finally, measurements of the longitudinal relaxation time, T_1, have been reported and show another type of monitoring adsorption/desorption of water in AC cloth.

Different parts of this work have been presented at five conferences, four international and one national.

A peer reviewed publication of spatially resolving the dynamics of liquid ingress in textile layers has been achieved [101]; in addition another publication is being written up where spatially resolved images of (i) ingress of liquid in AC cloth is revealed, and (ii) dynamics of vapour uptake in textile layers comprising AC cloth is examined. Although dodecane uptake has been successfully monitored, the results of the water front propagation still need further investigation and could then be added to this second publication.

VI.2. Future work

VI.2.1. Using short values of T_R for monitoring activated carbon samples with NMR

In chapter III it was shown that for short T_R values, the RF electromagnetic waves can deposit heat into AC samples. If T_R values shorter than 800 ms are needed, the heat deposition induced by NMR experiments in AC samples could be somewhat compensated for by delivering a continuous air flow at a well-characterised temperature.

VI.2.2. Restricting the lateral spread

In general, whilst collecting NMR data during these types of experiment where pressure is applied on top of the system, the lateral spread of oil in the fabric is sometimes too important and it therefore moves out of the sensitive volume. This results in the integral of the signal not being a constant. A preliminary experiment was set-up to examine whether this could be corrected. In this experiment the lateral spread of the liquid was restricted by placing it in a hollow cylinder in Perspex at the end of which was glued (with araldite) a fabric where a non-repellent layer was sandwiched between two repellent layers. The layers were also glued together (with araldite) just under the hollow cylinder, see Fig.VI.1.
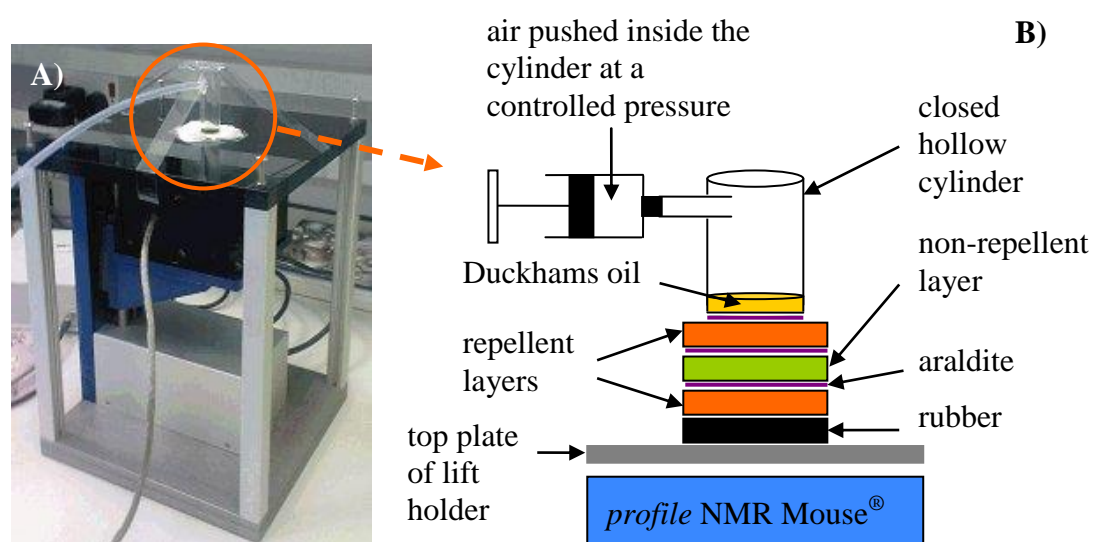
Fig.VI.1: Photograph **(A)** of experimental set up where the lateral spread of oil is prevented by araldite which keeps the layers together. The hollow cylinder was placed above the NMR Mouse® and secured with sellotape to the top plate of the lift so as to prevent the tilting from the Perspex tube. The corresponding schematic representation of the system under investigation is shown in **(B)**. A thin rubber layer was added to the system in order to facilitate post processing compensation of shifts due to fluctuations in temperature. The magenta horizontal strips represent the araldite.

In this experiment pressure was applied to a film of oil (placed on top of the fabric inside the hollow cylinder) using an air-filled syringe. The force of the air applied on the oil was measured with a pressure sensor. In order to digitally align the profiles (*i.e.* compensate for fluctuations due to temperature) a thin rubber layer was included at the bottom of the system.

A thicker spacer was placed under the plate hosting the RF coil of the NMR Mouse® so that the B_1 field is in closer proximity to the sensitive volume. The RF pulse needed to be made shorter allowing a broader frequency bandwidth to be created. Regarding the experimental set up, an extra thickness between the layers was added due to the glue holding the separate layers all together. This resulted in (i) both a film of air and a lack of parallelism residing between the layers; and (ii) a damage of the layers due to the application of the glue. Therefore the oil placed on the top repellent layer made its way *immediately* to the bottom repellent layer and eventually escaped the system under investigation (without any pressure applied on the top of the system). Consequently to develop this further in future work the gluing method would need to be improved substantially.

VI.2.3. Working at the resonance of fluorine

In all of this thesis, the focus has been on proton NMR. Challenges *simulating toxic liquids/vapours* containing as well fluorine (such as fluorobenzene, C_6H_5F, that Conard investigated [33]) or only fluorine are also of an interest. Future work could consist in trying to look at the problem of detecting fluorine signal coming from a fluorinated liquid ingressing the system. From the gyromagnetic ratio, γ, of ^{19}F, its resonance signal at 0.25 T should be around 10.01 MHz. The RF amplifier can work at this frequency, but the RF coil does not resonate at such a lower frequency. Fluorine measurements would need a separate tuned and matched RF coil, as well as a separate duplexer.

VI.2.4. T_1 measurement for a hydrocarbon

So far in this work, T_1 measurements on molecules other than water have not been investigated. So the separate measurements of T_1 values of different VOCs, such as nonane and heptane, should complete the data. This should be straightforward to do since the SNR obtained for water was quite high and the experimental set up does not meet any major difficulties other than being very quick in the preparation of the

experiment so that minimal atmospheric air contaminates the freshly reactivated AC cloth. The work could then be expanded to the AC monolith.

VI.2.5. T_1 effect during adsorption leading to the reduction of the hysteresis on T_2

For some molecules, a hysteresis on T_2 can be seen which is probably related to the T_1 effect. In measurements in this thesis, the effect on T_1 may somewhat be due to heat deposited in the system. T_1 is a parameter known to be able to reveal temperature changes [102, 103]. Future experiments to investigate this could include a warming up or cooling down of the AC cloth during monitoring of desorption. This should result both in allowing T_1 changes to be calibrated with temperature changes, and in minimizing the hysteresis on T_2. In separate experiments the rate at which the vapour is provided could be reduced to see whether this reduces the long T_1 values of the first two measurements.

VI.2.6. Potential use of a vapour generator constructed in situ

In many cases of adsorption that have been explored in this thesis, the very initial (and highest) values of R_2 were difficult to measure, because the signal was low in the very beginning of the uptake process and because short echo times can require rapid RF switching beyond the values allowed by the hardware. By using a vapour generator, uptake can be stopped and started on demand, and it should therefore be possible to monitor these initial values of R_2 with higher accuracy, by averaging the NMR signal for a longer time duration whilst the AC system's saturation level is kept in a steady state. Some initial experiments to test this approach were completed. A vapour generator was made of a flask with an integrated sintered glass on which a liquid droplet can be transformed into a gas. A flow of a compressed gas produced before the sintered gas should carry away the vapour to the outlet of the flask, see Fig.VI.2.
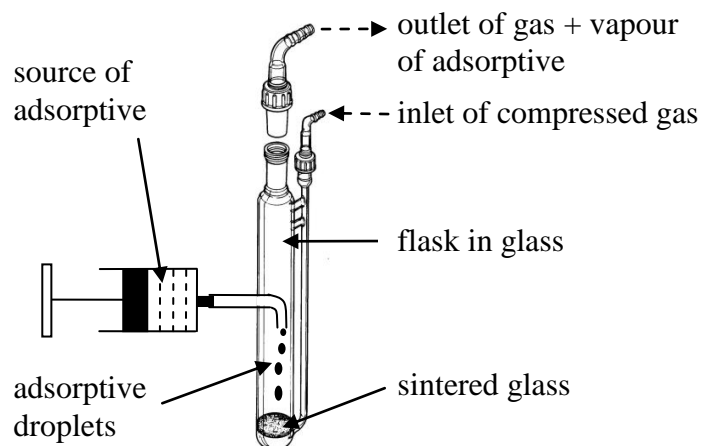
Fig.VI.2: Vapour generator. A source of liquid adsorptive can be delivered into the flask by means of a controlled syringe pump. Those drops fall onto the sintered glass where they become a vapour. The flow rate of compressed gas can also be controlled independently.

The flow rate of the gas passing through the vapour generator and the amount of liquid delivery can be controlled, allowing both the vapour flow rate and the vapour density to be adjusted.

It is seen that leakages of the syringe occur between the head of the mobile part and the static part. Indeed, the adsorptive liquid can transform into a vapour which is thin enough to escape. Therefore another type of syringe is needed. In order to produce gas, atmospheric air can be used and purified by a compressor (BAMBI VT75D available at the university). The "L" shape glass tube between the syringe and the main body of the flask was built and incorporated to it (at the chemistry glassware unit) in the University of Nottingham. In principle this approach seems feasible, but improvements would need to be done on how the source of adsorptive could be introduced to the flask for this to be a viable method. Moreover, by using a vapour generator, T_2 measurements could be obtained with better SNR (already mentioned earlier) and could be expanded to other adsorptives or even to a mixture of two adsorptives as is shown in a preliminary experiment, later on in section VI.2.8.

VI.2.7. Dynamic monitoring of water vapour propagation into 400 µm thick activated carbon cloth

In chapter IV and V it was found respectively that the ingress of oil, and the uptake of dodecane can be monitored into AC cloth. An interesting question is whether it may be possible to follow the propagation of a water vapour front. To investigate this, a pilot study experiment was set up to see whether such a front propagating into a 400 µm thick AC cloth during adsorption could be monitored.

For this type of experiment it is necessary to ensure that the vapour reaches the cloth from one side only. The design used consisted of placing four strips of JP2 AC cloth (each 2 cm wide) in the shape of a rectangle around the central cloth under investigation, see Fig.VI.3. The AC cloth JP2 was chosen for two reasons: 1. there was not enough of the *usually* used cloth in order to constitute such a large barrier; 2. its thickness (500 µm) is needed in order to have approximately the same thickness than two stacked cloths plus one repellent layer (470 µm). These JP2 AC cloth strips around the sample under investigation were at a distance of 6 cm from the centre of the sensitive volume in order to minimise interference with the B_1 field. These strips should be effective enough to prevent molecules reaching from the sides the cloth under investigation. The AC cloth (under investigation) was sandwiched between two repellent layers. The adsorptive should first reach the top of the cloth after having crossed the top repellent layer.

Perspex load vessel

"O" ring

AC cloth JP2 strips
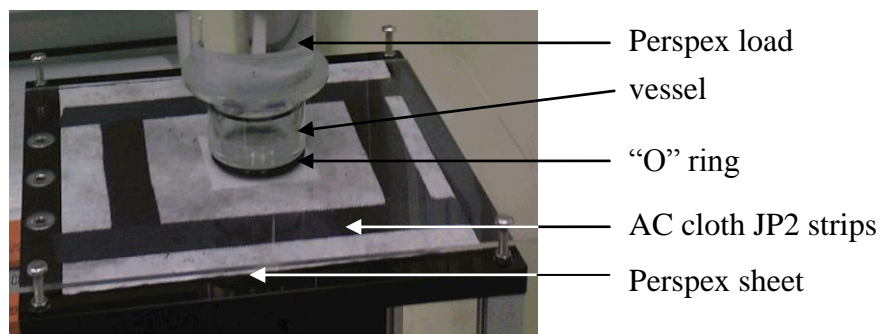
Perspex sheet

Fig.VI.3: Photograph of the experimental set up pointing to the arrangement of four strips of JP2 AC cloth in the shape of a rectangle around the cloth under investigation. The largest and smallest squares of white material represent respectively the bottom and the top repellent layers.

A sketch of the experimental set up (see Fig.VI.4) is supplied in addition to Fig.VI.3.
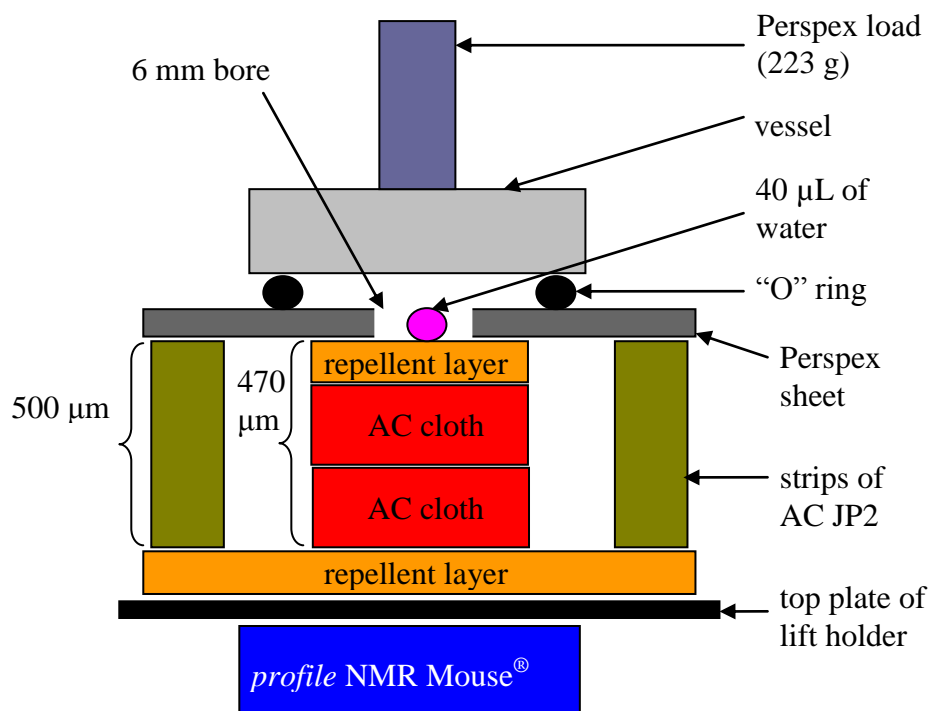
Fig.VI.4: Sketch of experimental set up for the monitoring of a water vapour front propagating into AC cloth during adsorption. Two AC cloths were stacked together producing a 400 μm thick layer. Additional JP2 AC cloth strips are used to prevent molecules to invade the cloth sideways. The thickness of the JP2 is similar to that of the two stacked cloths with the top repellent. The action of the Perspex load should eliminate this 6% relative difference due to the fact that (i) the Perspex sheet can sag easily and that (ii) the JP2 material can be squeezed a little bit.

The top and bottom repellent layers were respectively of the two following sizes (6 cm x 6 cm) and (21 cm x 21 cm). A large Perspex sheet (21 cm x 21 cm x 3 mm thick) with a 6 mm bore in its middle was placed on top of the system in order to flatten it. A toroidal "O" ring (i.d.: 4.4 cm, o.d.: 5.4 cm) was placed onto the Perspex sheet centred with the bore. 40 μL of water was deposited inside the bore of the flat Perspex sheet directly onto the top repellent layer, thereby forming a steady droplet. A vessel exhibiting a flat bottom was placed onto the "O" ring preventing water vapour to escape from the system. The NMR data was acquired with the CPMG sequence associated with the following settings: T_E = 120 μs, 128 echoes were collected, T_R = 600 ms, acquisition time = 50 μs and each experiment was averaged over for 10 minutes. The post processing was conducted by reconstructing a one dimensional profile from the averaged NMR signal. Each profile representing the 400 μm thickness of the cloth was stacked vertically so as to obtain an image of the propagating water front, see Fig.VI.5.
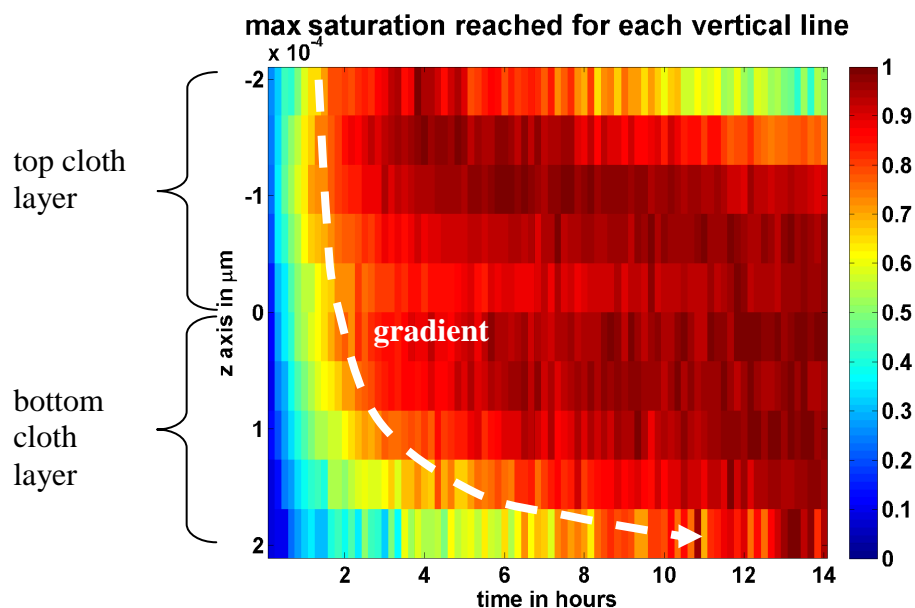
Fig.VI.5: Time course of the spatially resolved averaged NMR signal in two cloths stacked vertically. In this plot, each horizontal line, representing 40 μm, was scaled to its maximum in order to show the clear propagation of the solvent front during the uptake process irrespective of the absolute saturation level achieved at each *z* value.

This preliminary result clearly shows the water front moving downwards inside the stacked cloths. The top 40 μm of the cloth is saturated after 4 hours and the bottom cloth is saturated after 13 hours. A slow gradient (described on Fig.VI.5) can also be seen as the water propagates into the cloth.

The design was not optimal because as can be seen on Fig.VI.4, atmospheric water molecules can contaminate the cloth sideways and from the bottom side by crossing the bottom layer. Further investigation is needed to determine whether this repellent layer is needed or if it plane section is large enough to block molecules. In addition, it might be beneficial to insert a sintered glass in the bore of the Perspex sheet, so that the vapour homogeneously reaches the cloth. In order to have an optimised set up, this sintered glass should be of at least the size of the plane of the cloth.

VI.2.8. Uptake of a mixed vapour composed of water and heptane on activated carbon monolith, monitored with NMR

In chapter V, it was shown that it was possible to monitor the uptake of a single molecule. However, the relaxation rates for adsorbed water (approximately between 145 and 40 s^{-1}) and adsorbed heptane (approximately between 1000 and 200 s^{-1}) in the AC monolith seem to be sufficiently separated so as to suggest that it may be possible to individually monitor the simultaneous uptake of both these molecules. One experiment was attempted to gauge the feasibility of this using a thin monolith section. The experimental set up was similar to that described in section V.1.3.1.; the adsorptives were placed in two separate microcentrifuge tubes, one filled up with 1.5 mL of water and the other one filled with the same volume of heptane. The vapours were mixed in the receptacle once they escaped the microcentrifuge tubes. The NMR data were processed with a bi-exponential fit in order to extract two separate values of T_2 and the corresponding NMR amplitudes of both water and heptane, see Fig.VI.6, ending up in a four parameter fit.
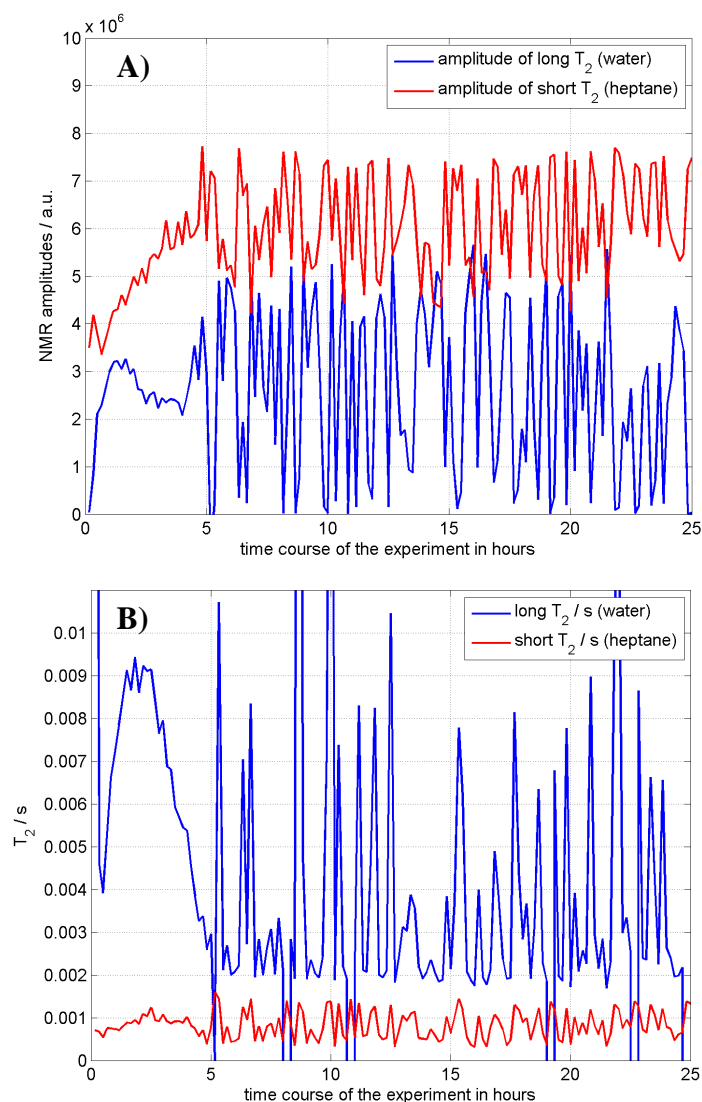
Fig.VI.6: Uptake of mixed vapours (water + heptane) on an AC monolith. Plots **A** and **B** represent respectively the time course of the NMR amplitudes and of R_2. During the first five hours of uptake, the two values of T_2 are far enough apart that they can be fitted individually. After five hours, they become so similar (around 1.5 ms) and so short that monoexponential fits can be used.

After almost five hours of uptake, it can be seen that T_2 for heptane falls under 400 µs. In the CPMG sequence, the echo time is 100 µs. In order to fit the bi-exponential decay, the third echo onwards, which is already at time 300 µs, is used. Therefore, the resulting signal is extremely low. By doing a bi-exponential fit, four values are generated with a poorer estimation than from a monoexponential fit (with only two parameters fit). In addition, the amplitude of the short T_2 (representing the adsorption of heptane) does not follow the usual trend; it increases during four and a half hours, after which the SNR is too low in order to extract useful information. The amplitude for

water increases until the 2 hours point and then reduces unlike heptane. It is unclear whether these results are genuine and clearly further work to optimize the design is needed before it is possible to have confidence in the data. Such an optimization could include using the vapour generator so that averaging the NMR signal for a much longer time duration would become possible.

REFERENCES

[1] M.A. Connell, P.J. Bowyer, P.A. Bone, A.L. Davis, A.G. Swanson, M. Nilsson, G.A. Morris, Improving the accuracy of pulsed field gradient NMR diffusion experiments: correction for gradient non-uniformity, Journal of Magnetic Resonance, **198**, (2009), 121-131.

[2] P. Schanda, Fast-pulsing longitudinal relaxation optimized techniques: enriching the toolbox of fast biomolecular NMR spectroscopy, Progress in Nuclear Magnetic Resonance Spectroscopy, **55**, (2009), 238-265.

[3] G.P. Schmidt, M.F. Reiser, A. Baur-Melnyk, Whole-body MRI for the staging and follow-up of patients with metastasis. European Journal of Radiology, **70**, (2009), 393-400.

[4] F. Kruggel, J. Turner, L.T. Muftuler and The Alzheimer's Disease Neuroimaging Initiative, Impact of scanner hardware and imaging protocol on image quality and compartment volume precision in the ADNI cohort, NeuroImage, **49**, (2010), 2123-2133.

[5] B.A. Moffat, C.J. Galbán, A. Rehemtulla, Advanced MRI: translation from animal to human in brain tumor research neuroimaging clinics of North America, **19**, (2009), 517-526.

[6] A.P.S. Kirkham, M. Emberton, C. Allen, How good is MRI at detecting and characterising cancer within the prostate? European Urology, **50**, (2006), 1163-1175.

[7] C. Kuhl, W. Kuhn, M. Braun, H. Schild, Pre-operative staging of breast cancer with breast MRI: one step forward, two steps back? The Breast, **16**, (2007), 34-44.

[8] H. Wen, S.S. Yoo, J. Kang, H.G. Kim, J.S. Park, S. Jeong, J.I. Lee, H.N. Kwon, S. Kang, D.H. Lee, S. Park, A new NMR-based metabolomics approach for the diagnosis of biliary tract cancer, J. Hepatol., **52**, (2010), 228-233.

[9] S.Y. Chung, P. Ehrenfreund, J.D. Rummel, N. Peter, Synergies of Earth science and space exploration, Advances in Space Research, **45**, (2010), 155-168.

[10] P. Ehrenfreund, N. Peter, K.U. Schrogl, J.M. Logsdon, Cross-cultural management supporting global space exploration, Acta Astronautica, **66**, (2010), 245-256.

[11] H. Le Treut, Modeling future climate changes: certainties and uncertainties, Houille blanche-revue internationale de l'eau, **8**, (2002), 69-72.

[12] M. Blazewicz, S. Blazewicz, C. Wajler, C Mechanical and implant behavior of chemically-modified carbon braids, Ceramics international, **20**, (1994), 99-103.

[13] J. Li, C. Papadopoulos, J.M. Xu, Highly-ordered carbon nanotube arrays for electronics applications, Appl. Phys. Lett., **75**, (1999), 367-369.

[14] T.A. Centeno, F. Stoeckli, Recent advances in adsorption processes for environmental protection and security, (poster at conference, September 09-12 2006), Kiev Ukraine, 9-18.

[15] E. Kissa, book: Handbook of Fibre Science and Technology, M. Lewin, S.B. Sello Eds., Marcel and Dekker Inc., New York, (1984).

[16] S.R. Coulson, I. Woodward, J.P.S. Badyal, S.A. Brewer, C. Willis, Super-repellent composite fluoropolymer surfaces, J. Phys. Chem. B, **104**, (2000), 8836-8840.

[17] S.R. Coulson, I. Woodward, J.P.S. Badyal, S.A. Brewer, C. Willis, Plasmachemical functionalization of solid surfaces with low surface energy perfluorocarbon chains, Langmuir, **16**, (2000), 6287-6293.

[18] S.R. Coulson, I. Woodward, J.P.S. Badyal, S.A. Brewer, C. Willis, Ultralow surface energy plasma polymer films, Chem. Maters., **12**, (2000), 2031-2038.

[19] X.J. Feng, L. Jiang, Design and creation of superwetting/antiwetting surfaces, Adv. Mater., **18**, (2006), 3063-3078.

[20] T. Young, An essay on the cohesion of fluids, Philos. Trans. R. Soc. London, **95**, (1805), 65-87.

[21] L. Léger and J.F. Joanny, Liquid spreading, Reports on Progress in Phys., **55**, (1992), 431-486.

[22] G.T. Barnes, I.R. Gentle, book: Interfacial Science, Oxford University Press, (2005).

[23] F.E. Taber, book: Fluid Dynamics for Physicists, Cambridge University Press, (1995).

[24] M. Weder, P.A. Bruhwiler, A. Laib, X-ray tomography measurements of the moisture distribution in multilayered clothing systems, Text. Res. J., **76**, (2006), 18-26.

[25]   M. Weder, P.A. Bruhwiler, U. Herzig, R. Huber, G. Frei, E. Lehmann, Neutron radiography measurements of moisture distribution in multilayer clothing systems, Text. Res. J., **74**, (2004), 685-700.

[26]   H.S. Lee, W.W. Carr, J. Leisen, H.W. Beckham, Through-air drying of unbacked tufted carpets, Text. Res. J., **71**, (2001), 613-620.

[27]   J. Leisen, H.W. Beckham, Quantitative magnetic resonance imaging of fluid distribution and movement in textiles, Text. Res. J., **71**, (2001), 1033-1045.

[28]   W.W. Carr, H.W. Beckham, H.W. Spiess, C. Fülber, B. Blümich, Nuclear-magnetic-resonance imaging of water distributions in loop-pile nylon carpet tiles, J. Text. Inst., **89**, (1998), 436-440.

[29]   S. Harding, H. Baumann, T. Gren, A. Seo, NMR microscopy of the uptake, distribution and mobility of dissolution media in small, sub-millimetre drug delivery systems, Journal of Controlled Release, **66**, (2000), 81-99.

[30]   H. Marsh, F. Rodriguez-Reinoso, book: Activated Carbon, Elsevier Ltd, (2006).

[31]   A.C. Lua, T. Yang, J. Guo, Effects of pyrolysis conditions on the properties of activated carbons prepared from pistachio-nut shells, J. Anal. Appl. Pyrolysis, **72**, (2004), 279-287.

[32]   L.J. Kennedy, J.J. Vijaya, G. Sekaran, Effect of two stage process on the preparation and characterization of porous carbon composite from rice husk by phosphoric acid activation, Ind. Eng. Chem. Res., **43**, (2004), 1832-1838.

[33]   S. Gradsztajn, J. Conard and H. Benoit, Etude de la surface de solides par RMN de liquides adsorbes-I. Origine du déplacement et de la largeur des raies dans le cas des carbones. J. Phys. Chem. Solids., **31**, (1970), 1121-1135.

[34]   S. Gradsztajn, D. Vivien and J. Conard, Etude de la surface de solides par RMN haute résolution de liquides adsorbes-II. Molécules à protons mobiles, J. Phys. Chem. Solids., **32**, (1971), 1507-1520.

[35]   S. Brunauer, P.H. Emmett, E. Teller, Adsorption of gases in multimolecular layers, J. Am. Chem. Soc., **60**, (1938), 309-319.

[36]   L.D. Gelb, K.E. Gubbins, Characterization of porous glasses: simulation models, adsorption isotherms, and the Brunauer-Emmett-Teller analysis method, Langmuir, **18**, (1998), 2097-2111.

[37]   P. Le Cloirec, G. Martin, J. Gallier, ^{1}H NMR investigation on phenol saturated and unsaturated activated carbon: quantification and exchange behavior of protons, Carbon, **26**, (1988) 275-282.

[38] Magic-Angle Spinning NMR study of the competitive adsorption of an organophosphate and an organophosphonate on activated carbon, J.A. Shaw, R.K. Harris, P.R. Norman, Langmuir, **14**, (1998), 6716-6721.

[39] Phosphorus-31 NMR studies of adsorption onto activated carbon, R.K. Harris, T.V. Thompson, P.R. Norman, C. Pottage, Carbon, **37**, (1998), 1425-1430.

[40] J.C.C. Freitas, F.G. Emmerich, G.R.C. Cernicchiaro, L.C. Sampaio, T.J. Bonagamba, Magnetic susceptibility effects on C-13 MAS NMR spectra of carbon materials and graphite, Solid State Nucl. Magn. Reson., **20**, (2001), 61-73.

[41] M.S. Solum, A.F. Sarofim, R.J. Pugmire, T.H. Fletcher, H. Zhang, C-13 NMR analysis of soot produced from model compounds and a coal, Energy Fuels, **15**, (2001), 961-971.

[42] Paper currently in preparation and work was presented by M. Melguizo Guijarrro at the international conference Carbon 2009 hold in Biarritz between 14th and 19th of June 2009. The information was extracted from the extended abstract from the conference proceedings CD made available to each participant. M. Melguizo-Guijarro, M.D. López de la Torre, O. del Pico-Hualde, A. Peñas-Sanjuan, C. García Gallarín, R. López-Garzón, M. Pérez-Mendoza, Influence of electromagnetic shielding effect of carbons on their 13C-NMR solid spectra.

[43] W. Zhang, A.A. Dehghani-Sanij, R.S. Blackburn, Carbon based conductive polymer composites, J. Maters. Sci., **42**, (2007), 3408-3418.

[44] L.D. Gelb, K.E. Gubbins, Pore size distributions in porous glasses: a computer simulation study, Langmuir, **15**, (1999), 305-308.

[45] C.I. Nicholls, A. De Los Santos, Hydrogen transient nuclear magnetic resonance for industrial moisture sensing, Drying Technol., **9**, (1991), 849-873.

[46] Development of prototype soil moisture sensors, NCHRP Research Results Digest 75, Transportation Research Board, Washington, 1975.

[47] G.A. Matzkanin, R.F. Paetzold, Measuring soil water content using pulsed nuclear magnetic resonance, ASAE Winter Mtg., **Paper No. 82-2619**, Chicago, Il, (1982).

[48] G.A. Matzkanin, W.L. Rollwitz, J.D. King, R.F. Paetzold, Principles of nuclear magnetic resonance for agricultural operations, proceedings of the national conference on agricultural electronics applications, ASAE, (1984), 309-318.

[49] R.F. Paetzold, G.A. Matzkanin, A. De Los Santos, Surface soil water content measurement using pulsed nuclear magnetic resonance techniques, Soil Sci. Soc. Am. J., **49**, (1985), 537-540.

[50] R.F. Paetzold, A. De Los Santos, G.A. Matzkanin, Pulsed nuclear magnetic resonance instruments for soil–water content measurement: sensor configurations, Soil Sci. Soc. Am. J., **51**, (1987), 287-298.

[51] G.A. Matzkanin, J.D. King, W.L. Rollwitz, Non-destructive measurement of moisture in concrete using pulsed NMR, proceedings of the 13th Symposium on Non-destructive evaluation, San Antonio, TX, April 21-23, (1981).

[52] A. Marko, B. Wolter, W. Arnold, Application of portable nuclear magnetic resonance surface probe porous media, J. Mag. Res., **185**, (2007), 19-25.

[53] R.M. Pearson, L.R. Ream, C. Job, J. Adams, Use of NMR spectrometers for process control, Cereal Foods World, **32**, (1987), 822-826.

[54] R.M. Pearson, Using industrial magnetic resonance for moisture monitoring, Cereal Foods World, **32**, (1987), 658.

[55] R.M. Pearson, D.I. Wetzel, Rapid on-line moisture determination of whole kernel wheat by pulsed nuclear magnetic resonance, Cereal Foods World, **30**, (1985), 563-564.

[56] G.A. Persyn, W.L. Rollwitz, Transient NMR quantitative measurements, JAOCS, **48**, (1971), 67-69.

[57] W.L. Rollwitz, G.A. Persyn, On-stream NMR measurements and control, JAOCS, **48**, (1971), 59-66.

[58] W.L. Rollwitz, J.D. King, G.A. Matzkanin, R.F. Paetzhold, Magnetic resonance: a versatile sensor for agricultural applications, Proceedings of the national conference on agricultural electronics applications, ASAE, Chicago, Il, (1983), 766-772.

[59] W.L. Rollwitz, Using radiofrequency spectroscopy in agricultural applications, Agric. Eng., **66**, (1985), 12-14.

[60] J. Perlo, Profiles with microscopic resolution by single-sided NMR, J. Mag. Res., **176**, (2005), 64-70.

[61] E.M. Purcell, H.C. Torrey and R.V. Pound, Resonance absorption by nuclear magnetic moments in a solid, Phys. Rev., **69**, (1946), 37-38.

[62] F. Bloch, W.W. Hansen, and M. Packard, "Nuclear induction," Phys. Rev., **69**, (1946), 127.

[63] P. Mansfield and P.K. Grannell, NMR 'diffraction' in solids?, J. Phys. C: Solid State Phys., **6**, (1973), L422-L426.

[64] P. Lauterbur, Image formation by induced local interactions: examples employing nuclear magnetic resonance, Nature, **242**, (1973), 190-191.

[65] R. Damadian, Apparatus and method for detecting cancer in tissue, US Patent 3789832, (1974).

[66] B. Blümich, book: Essential NMR, Springer, (2005).

[67] A. Abragam, book: The principles of nuclear magnetism, Oxford University Press, (1961).

[68] G.G. McDonald, J.S. Leigh, A new method for measuring longitudinal relaxation times, J. Mag. Res., **9**, (1973), 358-362.

[69] E.L. Hahn, Spin Echoes, Physical review, **80**, (1950).

[70] H.Y. Carr, E.M. Purcell, Effects of diffusion on free precession in nuclear magnetic resonance experiments, Phys Rev, **94**, (1954), 630-638.

[71] S. Meiboom, D. Gill, Modified spin-echo method for measuring nuclear relaxation times, Rev. Sci. Instrum., **29**, (1958), 688-691.

[72] R.L. Kleinberg, Well Logging, in "Encyclopedia of NMR", John Wiley and Sons, Chichester UK, (1996), 4960-4968.

[73] M.H. Cohen and K.S. Mendelson, Nuclear magnetic resonance and the internal geometry of sedimentary rocks, J. Appl. Phys., **53**, (1982), 1127-1135.

[74] K.R. Brownstein and C.E. Tarr, Importance of classical diffusion in NMR studies of water in biological cells, Phys. Rev. A, **19**, (1979), 2446-2453.

[75] D.G. Rata, F. Casanova, J. Perlo, D.E. Demco, B. Blümich, Self-diffusion measurements by a mobile single-sided NMR sensor with improved magnetic field gradient, J. Mag. Res., **180**, (2006), 229-235.

[76]: J.D. Jackson, book: Classical Electrodynamics, John Wiley & Sons, Inc., (1999).

[77] J. Perlo, F. Casanova, B. Blümich, 3D imaging with a single-sided sensor: an open tomography, J. Mag. Res., **166**, (2004), 228-235.

[78] G. Goelman, M.G. Prammer, The CPMG pulse sequence in strong magnetic field gradients with applications to oil-well logging, J. Mag. Res., **Ser. A 113**, (1995), 11-18.

[79] M.C.A. Brown, D.A. Verganelakis, M.J.D. Mallett, J. Mitchell, P. Blumler, Surface normal imaging with a hand-held NMR device, J. Mag. Res., **169**, (2004), 308-312.

[80] L.J. Kennedy, J.J. Vijaya, G. Sekaran, Electrical conductivity study of porous carbon composite derived from rice husk, Maters. Chem. Phys., **91**, (2005), 471-476.

[81] M.E. Ramos, P.R. Bonelli, A.L. Cukierman, Physico-chemical and electrical properties of activated carbon cloths effect of inherent nature of the fabric precursor, Colloids and Surfaces A: Physicochem. Eng. Aspects, **324**, (2008), 86-92.

[82] A. Subrenat, J.N. Baleo, P. Le Cloirec, P.E. Blanc, Electrical behaviour of activated carbon cloth heated by the joule effect: desorption application, Carbon, **39**, (2001), 707-716.

[83] V. Ruiz, C. Blanco, R. Santamaria, J.M. Ramos-Fernandez, M. Martinez-Escandell, A. Sepulveda-Escribano, F. Rodriguez-Reinoso, An activated carbon monolith as an electrode material for supercapacitors, Carbon, **47**, (2009), 195-200.

[84] S.R. Coulson, I. Woodward, J.P.S. Badyal, S.A. Brewer, C. Willis, Super-repellent composite fluoropolymer surfaces, J. Phys. Chem. B, **104**, (2000), 8836-8840.

[85] R.N. Wenzel, Surface roughness and contact angle, J. Phys. Chem., **53**, (1949), 1466-1467.

[86] A.B.D. Cassie, S. Baxter, Wettability of porous surfaces, Trans. Faraday Soc., **40**, (1944), 546-551.

[87] J.L. Moilliet, book: Waterproofing and water repellency, Elsevier Publishing, (1963).

[88] C.W. Extrand, Criteria for ultralyophobic surfaces, Langmuir, **20**, (2004), 5013-5018.

[89] G. Wolansky, A. Marmur, The actual contact angle on a heterogeneous rough surface in three dimensions, Langmuir, **14**, (1998), 5292-5297.

[90] A. Marmur, Contact angles in constrained wetting, Langmuir, **12**, (1996), 5704-5708.

[91] S.S. Chhatre, A. Tuteja, W. Choi, A. Revaux, D. Smith, J.M. Mabry, G.H. McKinley, R.E. Cohen, Thermal annealing treatment to achieve switchable and reversible oleophobicity on fabrics, Langmuir, **25(23)**, (2009), 13625-13632.

[92] B. Blümich, J. Perlo, F. Casanova, Mobile single-sided NMR, Progress in nuclear magnetic resonance spectroscopy, **52**, (2008), 197-269.

[93] J.M. Ramos-Fernandez, M. Martinez-Escandell, F. Rodriguez-Reinoso, Production of binderless activated carbon monoliths by KOH activation of carbon mesophase materials, Carbon, **46**, (2008), 365-389.

[94] S. Kumar, T. Rath, R.N. Mahaling, C.S. Reddy, C.K. Das, K.N. Pandey, R.B. Srivastava, S.B. Yadaw, Study on mechanical, morphological and electrical properties of carbon nanofiber/polyetherimide composites, Maters. Sci. Eng. B, **141**, (2007), 61-70.

[95] R. Thiruvenkatachari, S. Su, X.X. Yu, Carbon fibre composite for ventilation air methane (VAM) capture, Journal of Hazardous Materials, **172**, (2009), 1505-1511.

[96] D.R. Lide, book: CRC Handbook of Chemistry and Physics, **85th edition**, (2005).

[97] McLaughlin, Hugh Stanley, Method for destruction of organic compounds by co-oxidation with activated carbon, US Patent 6982068, (2006).

[98] I. Langmuir, The constitution and fundamental properties of solids and liquids, part I. solids., J. Am. Chem. Soc., **38**, (1916), 2221-2295.

[99] J.R. Rahn, R.B. Hallock, Antibody binding to antigen-coated substrates studied with surface plasmon oscillations, Langmuir, **11**, (1995), 650-654.

[100] N. Bloembergen, E.M. Purcell, R.V. Pound, Relaxation effects in nuclear magnetic resonance absorption, Phys. Rev., **73**, (1948), 679-712.

[101] M. Bencsik, H. Adriaensen, S.A. Brewer, G. McHale, Quantitative NMR monitoring of liquid ingress into repellent heterogeneous layered fabrics, J. Mag. Res., **193**, (2008), 32-36.

[102] F.G. Ridell, Intramolecular motions in solid organic compounds, "Encyclopedia of NMR", D.M. Grant, R.K. Harris, (2002), 570-578.

[103] X. Tang, Y. Wu, Quasicrystalline compounds: metallic glasses, "Encyclopedia of NMR", D.M. Grant, R.K. Harris, (2002), 729-737.

[104] J. Dunning-Davies, book: Mathematical method for Mathematicians, Physical Scientists and Engineers, Horwood Publishing Ltd, (2003).

APPENDIX

A. Isotherm equations

The isotherm equations are given here for information.

Kelvin equation:

$$\ln\left(\frac{p}{p^0}\right) = -\frac{2\gamma v_m}{r_K RT},$$ Eq [A.1]

where:

- p is the equilibrium vapour pressure in Pascal;
- p^0 is the saturation pressure in Pascal;
- v_m is the molar volume of the liquid;
- γ is the surface tension of the liquid;
- r_K is the effective radius of curvature of the liquid;
- R is the universal gas constant;
- T is the temperature.

Langmuir equation:

$$\frac{p/p^0}{n^a} = \frac{1}{bn_m^a} + \frac{p/p^0}{n_m^a},$$ Eq [A.2]

where:

- n^a is the weight of adsorbate at some p/p^0 in $mmol.g^{-1}$ or in $cm^3.g^{-1}$;
- n_m^a is the monolayer capacity (= weight of adsorbate in a monolayer) in $mmol.g^{-1}$ or in $cm^3.g^{-1}$;
- b is a constant associated with the energy of adsorption.

BET equation:

$$\frac{p}{V(p^0 - p)} = \frac{1}{V_m c} + \frac{(c-1)p}{V_m c p^0} ,$$ Eq [A.3]

where:

- V is the amount of gas adsorbed at a relative pressure p/p^0 in cm^3.g^{-1};
- V_m is the volume of adsorbate constituting a monolayer coverage in cm^3.g^{-1};
- the term c, the BET c constant, is related to the energy of adsorption in the first adsorbed layer and consequently its value is an indication of the magnitude of the adsorbent/adsorbate interactions.

DR equation:

$$V = V_0 \exp\left(\frac{-BT}{\beta \log^2(p^0/p)}\right),$$ Eq [A.4]

where:

- V is the volume of adsorbate filling micropores in cm^3.g^{-1};
- V_0 is the total volume of the micropore system in cm^3.g^{-1} and is often assumed to equate to values of V_m and hence of n_m^a
- B is the point B of the isotherm being the position of n_m^a;
- T is the adsorption temperature in K;
- β is an affinity coefficient.

B. Diffusion resulting from Fick's equation

The discussion treats first the case of a 1D problem before tackling the 3D problem.

Fick's equation describes the motion of "something" when "something" is allowed to diffuse and has a spatial gradient in concentration, *i.e.* the flux goes from regions of high concentration to regions of low concentration. Fick's equation is as follows:

$$J = -D\frac{\partial \Phi}{\partial x},$$

with:

J: diffusion flux in 1D in mol.m^{-2}.s^{-1},

D: diffusion coefficient in m^2.s^{-1},

Φ: concentration in mol.m^{-3},

x: position in m.

Here, one Cartesian component of the nuclear magnetisation *e.g.* M_x is considered as if it were a fluid and is assigned to Φ. J is assimilated to the diffusion flux of that component of the nuclear magnetisation.
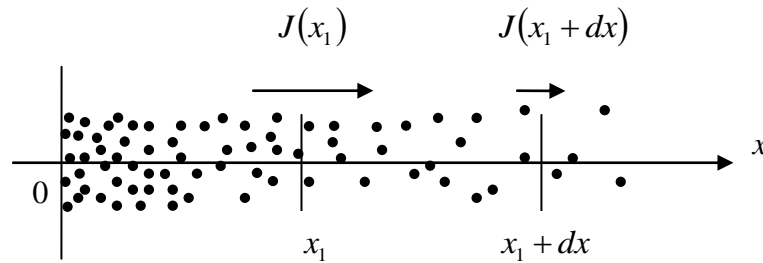
Fig.B.1: Representation of the diffusion of the nuclear magnetisation (magnetic flux) treated in the case of a 1D problem. The dots represent the concentration of the nuclear magnetisation.

Locally, if the concentration gradient, $\dfrac{\partial M_x}{\partial x}$, of the nuclear magnetisation is constant, there is as much flux at x_1 as at $x_1 + dx$, and the local magnetisation is therefore constant, *i.e.* $\dfrac{\partial M_x}{\partial t} = 0$. However, if the concentration gradient is higher at x_1 than at $x_1 + dx$, it results in a change in the local magnetisation (resulting from the conservation of mass) so that:

175

$$\frac{\partial M_x}{\partial t} = -\frac{J(x_1 + dx) - J(x_1)}{dx},$$

yielding:

$$\frac{\partial M_x}{\partial t} = -\frac{\partial J}{\partial x}.$$

By substituting Fick's equation into this mass equation, the following result is obtained:

$$\frac{\partial M_x}{\partial t} = --D\frac{\partial}{\partial x}\left(\frac{\partial M_x}{\partial x}\right)$$

$$\Leftrightarrow$$

$$\frac{\partial M_x}{\partial t} = D\frac{\partial^2 M_x}{\partial x^2}.$$

For the 3D case, all the components of $\underline{J}$ must be accounted for as it is now considered as a vector quantity. A local rate of change in the concentration of x component of the nuclear magnetisation, M_x, is due to the sum of three differential magnetic fluxes:

$$\frac{\partial M_x}{\partial t} = -\left\{\frac{\partial J_x}{\partial x} + \frac{\partial J_y}{\partial y} + \frac{\partial J_z}{\partial z}\right\}$$

$$\Leftrightarrow$$

$$\frac{\partial M_x}{\partial t} = -\left\{-D\frac{\partial}{\partial x}\left(\frac{\partial M_x}{\partial x}\right) - D\frac{\partial}{\partial y}\left(\frac{\partial M_x}{\partial y}\right) - D\frac{\partial}{\partial z}\left(\frac{\partial M_x}{\partial z}\right)\right\}$$

$$\Leftrightarrow$$

$$\frac{\partial M_x}{\partial t} = D\left\{\frac{\partial^2 M_x}{\partial x^2} + \frac{\partial^2 M_x}{\partial y^2} + \frac{\partial^2 M_x}{\partial z^2}\right\},$$

Furthermore, $\left\{\frac{\partial^2 M_x}{\partial x^2} + \frac{\partial^2 M_x}{\partial y^2} + \frac{\partial^2 M_x}{\partial z^2}\right\}$ is the Laplacian of M_x, also written: $\nabla^2 M_x$, therefore the rate of change of the x component of the nuclear magnetisation is:

$$\frac{\partial M_x}{\partial t} = D\nabla^2 M_x,$$

and by treating each component of $\underline{M}$ similarly, the rate of change of the vectorial nuclear magnetisation is given by

$$\frac{\partial \underline{M}}{\partial t} = D\nabla^2 \underline{M}.$$

C. How to find T_1

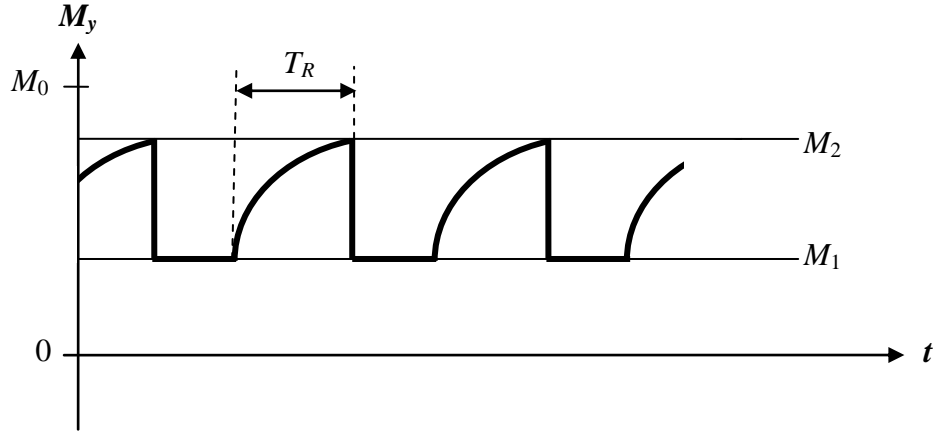*What is the optimum T_R to use for the highest SNR?*

Fig.C.1: Schematic of the time course of the longitudinal magnetisation, when the magnetisation is repeatedly tilted by a moderate flip angle, α, and then left to recover for a time duration, T_R.

M_1 and M_2 are defined on Fig.C.1:

M_1 is the value that the longitudinal component of the magnetisation takes just after a RF pulse.

M_2 is the value that the longitudinal component of the magnetisation takes after a recovery time, T_R.

The differential equation for M_y is:

$$\dot{M}_y(t) = -\frac{\left(M_y(t) - M_0\right)}{T_1}$$

M_y: longitudinal component of the magnetisation at time, t.

M_0: magnitude of the fully polarised nuclear magnetisation (before any excitation pulse is applied).

This is a non-homogeneous first order differential equation.

C.1. First the homogeneous equation needs to be solved

$$\dot{M}_y(t) = -\frac{M_y(t)}{T_1}.$$

Its integration yields:

$$\ln\left(M_y(t)\right) = \frac{-t}{T_1} + A,$$

where A is a constant of integration. By using the exponential function it is obtained that:

$$M_y(t) = \exp\left(\frac{-t}{T_1} + A\right) \text{ which may be rearranged into:}$$

$$M_y(t) = B\exp\left(\frac{-t}{T_1}\right).$$

C.2. Account for the full equation

$$\dot{M}_y(t) = -\frac{\left(M_y(t) - M_0\right)}{T_1}$$

By assuming that $|B|$ is a function of time, the previous solution is forced to be a solution of the new equation in order to determine $B(t)$.

$$\dot{M}_y(t) = \dot{B}(t)\exp\left(\frac{-t}{T_1}\right) - \frac{B(t)}{T_1}\exp\left(\frac{-t}{T_1}\right)$$

Rearranging this gives:

$$\dot{B}(t) = \frac{M_0}{T_1}\exp\left(\frac{t}{T_1}\right)$$

Both sides are integrated so as to yield:

$$B(t) = M_0\exp\left(\frac{t}{T_1}\right) + C, \quad \text{with } C \text{ a constant of integration.}$$

Therefore, $M_y(t)$ becomes:

$$M_y(t) = M_0 + C\exp\left(\frac{-t}{T_1}\right)$$
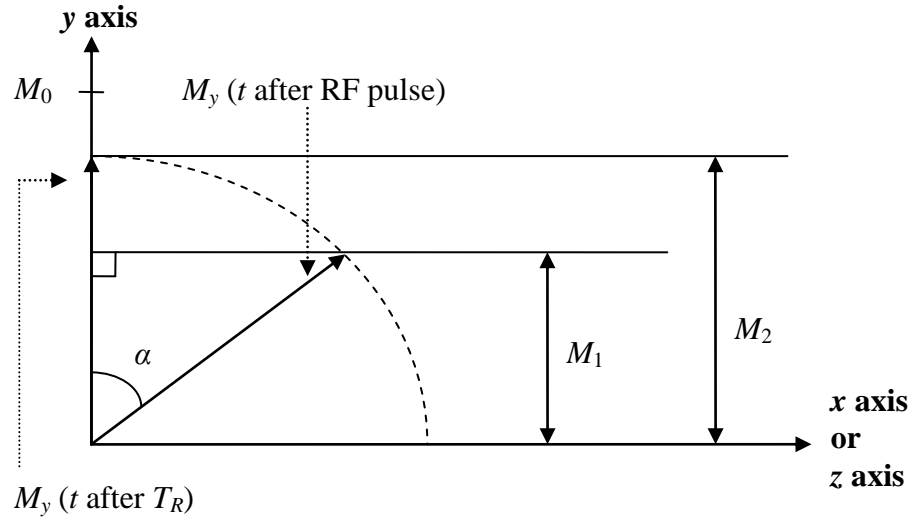
C.3. Determination of C

Fig.C.2: Schematic showing M_1 and M_2 as projections of $M(t)$. α is graphically determined and is the angle between the M_y (t after RF pulse) and M_y (t after T_R).

Further:

$$M_y(T_R) = M_2 = M_0 + C\exp\left(\frac{-T_R}{T_1}\right)$$

and

$$M_y(0) = M_1 = M_0 + C\exp(0) = M_0 + C$$
$$\Leftrightarrow C = M_1 - M_0$$
$$\Leftrightarrow C = M_2\cos(\alpha) - M_0.$$

Thus

$$M_2 = M_0\left(\frac{1 - \exp\left(\dfrac{-T_R}{T_1}\right)}{1 - \cos(\alpha)\exp\left(\dfrac{-T_R}{T_1}\right)}\right).$$

C.4. Furthermore, on the NMR Mouse®, the RF pulse $\alpha = 90°$, hence:

$$M_2 = M_y(T_R) = M_0\left(1 - \exp\left(-\frac{T_R}{T_1}\right)\right).$$

C.5. Assuming that N averages are acquired, so the experimental time is: $T = N \times T_R$ (neglecting the time duration of the CPMG):

- noise grows like $\sqrt{N}$.

This is because in "counting statistics" or in "Poisson statistics" the standard deviation is equal to the square-root of the number of individual experiments.

- signal grows like $N \times Signal$,

- SNR grows like $\dfrac{N \times Signal}{\sqrt{N}}$,

obtaining:

$$\sqrt{N} = \sqrt{\frac{T}{T_R}} \,.$$

Thus

$$SNR \propto \frac{\dfrac{T}{T_R} \times M_y(T_R)}{\sqrt{\dfrac{T}{T_R}}}\,.$$

Therefore

$$\boxed{SNR \propto \sqrt{\frac{T}{T_R}} \times M_0 \times \left(1 - \exp\left(-\frac{T_R}{T_1}\right)\right)}\,.$$

D. Equation dictating the saturation recovery sequence

Eq [II.8] reads as:

$$\frac{dM_y(t)}{dt} = -\frac{M_y(t) - M_0}{T_1}$$

by rearranging, it becomes:

$$\frac{dM_y(t)}{dt} \times \frac{1}{M_y(t) - M_0} = -\frac{1}{T_1}$$

integrating it gives:

$$\ln\left(M_y(t) - M_0\right) = -\frac{t}{T_1} + A \qquad \text{Eq [D.1]}$$

where A is a constant of integration. By using the exponential function:

$$M_y(t) - M_0 = \exp\left(-\frac{t}{T_1}\right)\exp(A)$$

$$\Leftrightarrow$$

$$\exp(A) = \frac{M_y(t) - M_0}{\exp\left(-\dfrac{t}{T_1}\right)} \qquad \text{Eq [D.2]}$$

At $t = 0$, Eq [D.1] becomes:

$$\ln\left(M_y(t_0) - M_0\right) = A$$

$$\Leftrightarrow$$

$$\exp(A) = M_y(t_0) - M_0 \qquad \text{Eq [D.3]}$$

combining Eq [D.2] and Eq [D.3] gives:

$$\frac{M_y(t) - M_0}{\exp\left(-\dfrac{t}{T_1}\right)} = M_y(t_0) - M_0$$

$$\Leftrightarrow$$

$$M_y(t) = M_0 + \left(M_y(t_0) - M_0\right)\exp\left(-\frac{t}{T_1}\right) \qquad \text{Eq [D.4]}$$

by assuming that $M_y(t_0) = 0$ since $\alpha = 90°$ on the Mouse$^{®}$ and t is the repetition time T_R, Eq [D.4] becomes:

$$M_y(t) = M_0 - M_0 \exp\left(-\frac{T_R}{T_1}\right)$$

$$\Leftrightarrow$$

$$M_y(t) = M_0\left(1 - \exp\left(-\frac{T_R}{T_1}\right)\right)$$

E. Relationship between FWHM and R_2

E.1. Real and imaginary part of the Fourier Transform (FT) of f(t)

From the definition of the FT given later on in appendix F:

$$FT(f(t)) = \int_{-\infty}^{+\infty} f(t) \exp(-2i\pi\nu t) dt$$

$$\Leftrightarrow$$

$$FT(f(t)) = \int_{-\infty}^{+\infty} f(t)[\cos(2\pi\nu t) - i\sin(2\pi\nu t)] dt$$

$$\Leftrightarrow$$

$$FT(f(t)) = \underbrace{\int_{-\infty}^{+\infty} f(t)\cos(2\pi\nu t) dt}_{\mathfrak{Re}} - i\underbrace{\int_{-\infty}^{+\infty} f(t)\sin(2\pi\nu t) dt}_{\mathfrak{Im}}$$

thus

$$FT(f(t)) = FT_C(f(t)) - iFT_S(f(t)),$$

with:

$FT_C(f(t))$ the "cos FT" being the real part of the Fourier transform of *f(t)*, and

$FT_S(f(t))$ the "sin FT" being the imaginary part of the Fourier transform of *f(t)*.

E.2. Definition of the FT of an NMR signal

For the following NMR signal $f(t) = \cos(\omega_0 t)\exp\left(-\dfrac{t}{T_2}\right)$ for $t \geq 0$,

with ω_0 the Larmor frequency of the spin in the rotating frame and T_2 being the transverse relaxation time (as obtained above):

$$FT(f(t)) = FT_C(f(t)) - iFT_S(f(t)),$$

with

$$FT_C(f(t)) = C(\omega) = \int_{-\infty}^{+\infty} f(t)\cos(\omega t) dt ,$$

and

$$FT_S(f(t)) = S(\omega) = \int_{-\infty}^{+\infty} f(t)\sin(\omega t)dt \; ;$$

therefore,

$$FT(f(t)) = \int_{-\infty}^{+\infty} f(t)\cos(\omega t)dt - i\int_{-\infty}^{+\infty} f(t)\sin(\omega t)dt \, .$$

But for this case, the function $f(t)$ is defined for $t \geq 0$, thus

$$FT(f(t)) = \int_{0}^{+\infty} \cos(\omega t)\cos(\omega_0 t)\exp\left(-\frac{t}{T_2}\right)dt - i\int_{0}^{+\infty} \sin(\omega t)\cos(\omega_0 t)\exp\left(-\frac{t}{T_2}\right)dt \, . \quad \text{Eq [E.1]}$$

E.3. Simplification with the addition formulae of trigonometry

On one hand there is:

$$\cos a\cos b = \cos(a+b)+\sin a\sin b$$

$$\Leftrightarrow$$

$$\cos a\cos b = \cos(a+b)+\cos(a-b)-\cos a\cos b$$

$$\Leftrightarrow$$

$$\cos a\cos b = \frac{\cos(a+b)+\cos(a-b)}{2} \, . \quad\quad\quad\quad\quad\quad \text{Eq [E.2]}$$

On the other hand there is:

$$\cos a\sin b = -\sin a\sin b + \sin(a+b)$$

$$\Leftrightarrow$$

$$\cos a\sin b = -\sin(a-b)-\cos a\sin b + \sin(a+b)$$

$$\Leftrightarrow$$

$$\cos a\sin b = -\sin(a-b)-\cos a\sin b + \sin(a+b)$$

$$\Leftrightarrow$$

$$2\cos a\sin b = -\sin(a-b)+\sin(a+b)$$

$$\Leftrightarrow$$

$$\cos a\sin b = \frac{\sin(b+a)+\sin(b-a)}{2} \, . \quad\quad\quad\quad\quad\quad \text{Eq [E.3]}$$

E.4. Combination of Eq [E.1], Eq [E.2] and Eq [E.3]

By including Eq [E.2] and Eq [E.3] in Eq [E.1], it is found that:

$$FT(f(t)) = \frac{1}{2} \int_0^{+\infty} (\cos(\omega_0 t + \omega t) + \cos(\omega_0 t - \omega t)) \exp\left(-\frac{t}{T_2}\right) dt$$

$$- \frac{i}{2} \int_0^{+\infty} (\sin(\omega t + \omega_0 t) + \sin(\omega t - \omega t_0)) \exp\left(-\frac{t}{T_2}\right) dt \,. \qquad \text{Eq [E.4]}$$

E.5. Other definitions about integrals

From a book of standard integrals [104]:

$$\int_0^{+\infty} \cos ax \exp(-bx) dx = \frac{b}{a^2 + b^2}$$

and

$$\int_0^{+\infty} \sin ax \exp(-bx) dx = \frac{a}{a^2 + b^2}$$

applied to the cases of interest:

$$\int_0^{+\infty} \cos((\omega_0 + \omega)t) \exp\left(-\frac{t}{T_2}\right) dt = \frac{\dfrac{1}{T_2}}{(\omega_0 + \omega)^2 + \left(\dfrac{1}{T_2}\right)^2} \,, \qquad \text{Eq [E.5]}$$

$$\int_0^{+\infty} \cos((\omega_0 - \omega)t) \exp\left(-\frac{t}{T_2}\right) dt = \frac{\dfrac{1}{T_2}}{(\omega_0 - \omega)^2 + \left(\dfrac{1}{T_2}\right)^2} \,, \qquad \text{Eq [E.6]}$$

$$\int_0^{+\infty} \sin((\omega + \omega_0)t) \exp\left(-\frac{t}{T_2}\right) dt = \frac{\omega + \omega_0}{(\omega + \omega_0)^2 + \left(\dfrac{1}{T_2}\right)^2} \text{ and} \qquad \text{Eq [E.7]}$$

$$\int_0^{+\infty} \sin((\omega - \omega_0)t) \exp\left(-\frac{t}{T_2}\right) dt = \frac{\omega - \omega_0}{(\omega - \omega_0)^2 + \left(\dfrac{1}{T_2}\right)^2} \,. \qquad \text{Eq [E.8]}$$

Introducing Eq [E.5], Eq [E.6], Eq [E.7] and Eq [E.8] in Eq [E.4] gives:

$$FT(f(t)) = \frac{1}{2}\left(\frac{\frac{1}{T_2}}{(\omega_0 + \omega)^2 + \left(\frac{1}{T_2}\right)^2} + \frac{\frac{1}{T_2}}{(\omega_0 - \omega)^2 + \left(\frac{1}{T_2}\right)^2}\right) - \frac{i}{2}\left(\frac{\omega + \omega_0}{(\omega + \omega_0)^2 + \left(\frac{1}{T_2}\right)^2} + \frac{\omega - \omega_0}{(\omega - \omega_0)^2 + \left(\frac{1}{T_2}\right)^2}\right)$$

$$\Leftrightarrow$$

$$FT(f(t)) = \frac{1}{2}\left(\frac{T_2}{1 + (\omega_0 + \omega)^2 T_2^2} + \frac{T_2}{1 + (\omega_0 - \omega)^2 T_2^2}\right) - \frac{i}{2}\left(\frac{(\omega + \omega_0)T_2^2}{1 + (\omega_0 + \omega)^2 T_2^2} + \frac{(\omega - \omega_0)T_2^2}{1 + (\omega_0 - \omega)^2 T_2^2}\right).$$

Eq [E.9]

E.6. Normal spectrum

In Eq [E.9], the real part is made of two absorption lines $A(\omega)$ centred on the frequencies $\pm\omega_0$, the imaginary part is made of two dispersion lines $D(\omega)$ centred on the same frequencies $\pm\omega_0$.

The normalised absorption is:

$$A_{\omega_0}(\omega) = \frac{T_2}{1 + (\omega_0 - \omega)^2 T_2^2}.$$

The normalised dispersion is:

$$D_{\omega_0}(\omega) = \frac{(\omega - \omega_0)T_2^2}{1 + (\omega_0 - \omega)^2 T_2^2}.$$

The normalised spectrum is:

$$FT(f(t)) = f(\omega) = \sqrt{A_{\omega_0}^2(\omega) + D_{\omega_0}^2(\omega)}$$

$$\Leftrightarrow$$

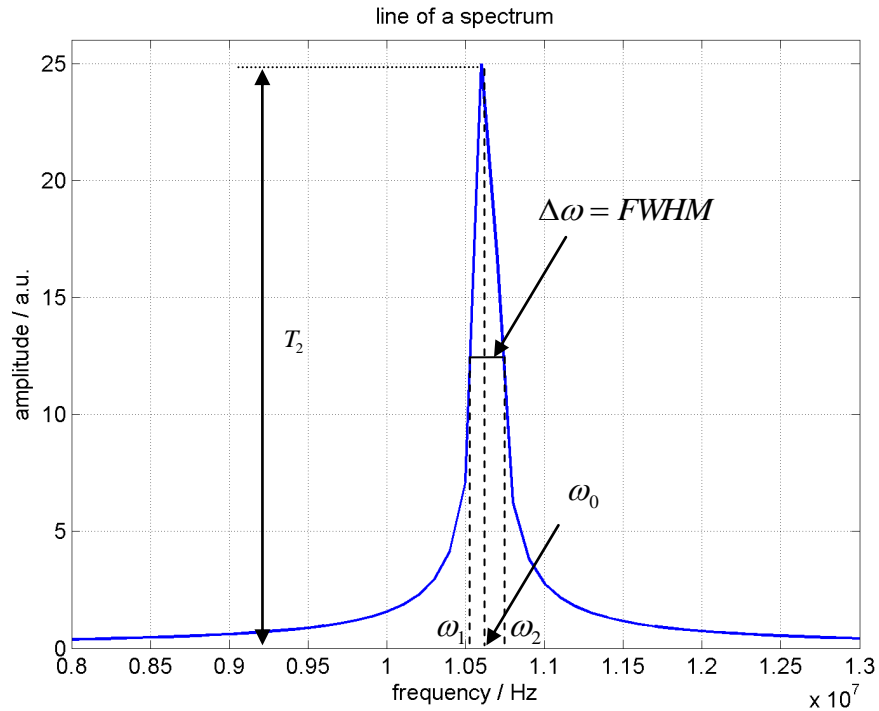$$f(\omega) = \sqrt{\frac{T_2^2}{1 + (\omega_0 - \omega)^2 T_2^2}}.$$

Fig.E.1: Representation of a line width within an NMR spectrum. T_2 is the amplitude of the line. ω_0, ω_1 and ω_2 are defined graphically and correspond to the frequencies of $\Delta\omega$. The non-zero width of the peak is due to the T_2 relaxation.

E.7. Determination of the value of the FWHM

From Fig.E.1:

$$FWHM = \Delta\omega = |\omega_2 - \omega_1| = 2 \times |(\omega_0 - \omega_1)| .$$

The amplitude of the peak is found at ω_0:

$$\therefore f(\omega_0) = \sqrt{\frac{T_2^{\,2}}{1 + (\omega_0 - \omega_0)^2 T_2^{\,2}}} = T_2 .$$

For which value of ω_1 does $f(\omega)$ reach half of the height of the peak?

$$f(\omega_1) = \frac{f(\omega_0)}{2} = \frac{T_2}{2} = \sqrt{\frac{T_2^{\,2}}{1 + (\omega_0 - \omega_1)^2 T_2^{\,2}}}$$

$$\Leftrightarrow$$

$$\frac{T_2}{2} = \sqrt{\frac{T_2^{\,2}}{1 + (\omega_0 - \omega_1)^2 T_2^{\,2}}}$$

$$\Leftrightarrow$$

187

$$\frac{T_2{}^2}{4} = \frac{T_2{}^2}{1 + (\omega_0 - \omega_1)^2 T_2{}^2}$$

$$\Leftrightarrow$$

$$4 = 1 + (\omega_0 - \omega_1)^2 T_2{}^2$$

$$\Leftrightarrow$$

$$\frac{\sqrt{3}}{T_2} = \omega_0 - \omega_1$$

$$\therefore \Delta\omega = 2 \times |(\omega_0 - \omega_1)| = 2 \times \left|\frac{\sqrt{3}}{T_2}\right| = \frac{2\sqrt{3}}{T_2},$$

giving: $FWHM = \dfrac{2\sqrt{3}}{T_2} = 2\sqrt{3}R_2.$

F. Fourier transform

The Fourier transformation is defined as:

$$FT(f(t)) = F_\upsilon(f(t)) = \int_{-\infty}^{+\infty} f(t)\exp(-2i\pi\nu t)dt$$

ν : frequency.

$f(t)$: function of time, t.

$FT(f(t))$ or $F_\upsilon(f(t))$: Fourier transform of $f(t)$, also called frequency spectrum.

G. Shift theorem

From the definition of the Fourier transform it is found that:

$$F_\upsilon[f(t+shift)] = \int_{-\infty}^{+\infty} f(t+shift)\exp(-2i\pi\upsilon t)dt .$$

Let ξ be the value of the *shift*; by applying the following change of variable:

$$T = t + \xi ,$$

$$dT = dt ,$$

$$t = T - \xi ,$$

$$F_\upsilon[f(t+\xi)] = \int_{-\infty}^{+\infty} f(T)\exp(-2i\pi\upsilon(T-\xi))dT$$

with $\exp(-2i\pi\upsilon(T-\xi)) = \exp(-2i\pi\upsilon T)\underbrace{\exp(2i\pi\upsilon(\xi))}$ ⟵ constant with respect to time.

$$\therefore F_\upsilon[f(t+\xi)] = \exp(2i\pi\upsilon\xi)\int_{-\infty}^{+\infty} f(T)\exp(-2i\pi\upsilon T)dT$$

thus

$$F_\upsilon[f(t+\xi)] = \exp(2i\pi\upsilon\xi)F_\upsilon[f(t)].$$

H. Publication

H.1. Journal of Magnetic Resonance